ABSTRACT

Title of Dissertation: A SONG OF FIRE & ICE: EVOLUTIONARY PROPERTIES OF HOT & COLD SMALL BODIES

Carrie E. Holt
Doctor of Philosophy, 2023

Dissertation Directed by: Professor Matthew Knight
Department of Physics
US Naval Academy

Small bodies (i.e., asteroids and comets) play an important role in our understanding of the Solar System. They are composed of the same planetesimal material that was incorporated into the planets, but their smaller size kept them from experiencing extensive processing (such as differentiation or atmosphere-related surface erosion). Therefore, their primitive nature allows us to probe the composition of the early Solar System and its subsequent evolution. Even though comets and asteroids are expected to contain material characteristic of their formation region, they have undoubtedly undergone some degree of processing since they were formed. The overarching motivation for small-body science is to disentangle primordial characteristics from evolutionary characteristics developed since formation with the goal of better understanding how our Solar System came to be. This work seeks to tackle a small piece of this goal by studying the objects of two extreme populations: the most and least thermally processed bodies.

This thesis uses ground-based broadband optical photometry to investigate the differences between different small body populations and how thermal processing alters the

characteristics of objects over time. First, we investigate the optical colors of near-Sun asteroids that experience extreme temperatures of > 1000 K to better understand the dominant processes that affect their surface properties and could potentially lead to their disruption. Next, we characterize the long-term brightness evolution of long-period comets using two distinct datasets: 1) an observing campaign that conducts long-term monitoring of long-period comets that are active beyond the region where water-ice sublimation is efficient, and 2) photometric magnitudes of long-period comets with well-characterized orbits that were collected and reported by amateur observers. We assess our ability to improve brightness predictions for comets discovered at large heliocentric distances and establish if brightness behavior can be used as a diagnostic of dynamical age.

A SONG OF FIRE & ICE:
EVOLUTIONARY PROPERTIES OF
HOT & COLD SMALL BODIES

by

Carrie E. Holt

Dissertation submitted to the Faculty of the Graduate School of the
University of Maryland, College Park in partial fulfillment
of the requirements for the degree of
Doctor of Philosophy
2023

Advisory Committee:
Professor Matthew M. Knight, Co-Chair/Advisor
Professor Derek C. Richardson, Co-Chair
Dr. Michael S. P. Kelley
Professor Stuart Vogel
Dr. Stefanie Milam, External Examiner
Professor Christine Hartzell, Dean's Representative

Preface

Some sections of the research presented in this dissertation have been previously published. Chapter 2 is presented with minimal modification since appearing in the Planetary Science Journal (PSJ) as "Surface Properties of Near-Sun Asteroids" (Holt et al., 2022a). Preliminary findings of the work described in Chapter 3 were published in PSJ as "The LCO Outbursting Objects Key Project: Overview and Year 1 Status" (Lister et al., 2022). The project described in Lister et al. (2022) encompasses two main observing objectives: follow-up of outbursts and long-term monitoring of distant long-period comets (LPCs). I am leading the analysis of LPCs, and reported the observations and findings from Year 1 in Lister et al. (2022) and synthesized results from all three years of the initial observation phase in Chapter 3. However, no text in this thesis is taken directly from Lister et al. (2022).

Acknowledgments

This thesis represents the collective influence of remarkable individuals who have contributed to my growth and played an instrumental role in shaping both my character and the content of this work.

I'd like to first give my endless thanks to my advisor, Matthew Knight. Your encouragement and dedication to my success is the reason I made it this far. Thank you for encouraging me to travel and introducing me to ground-based observing* and the widespread comet community. So many of my favorite science moments have occurred while observing or at meetings. Thank you for believing in me when I didn't believe in myself. You've trusted me to work through my science questions (and mistakes) and are always willing to talk things out when I get stuck. You helped me realize my love for science again after nearly quitting, and for that, I will be forever grateful.

I'd like to thank my academic advisor, Derek Richardson. Even as an observer, you immediately welcomed me into your group with open arms. Thank you to Mike Kelley for challenging me to be a better scientist and taking the time to introduce me to new ideas. Many thanks to Stuart Vogel for setting the wheels in motion to get me here today by passing around my resume and introducing me to Mike and Lori, who then introduced me to comets. And thank you to my newest committee member, Stefanie Milam. We haven't known each other long, but I am so thankful for your encouragement.

*(thanks for covering my observing run the week this dissertation is due)

I am indebted to so many incredible scientists: Tim Lister, Colin Snodgrass, Cyrielle Opitom, Rosita Kokotanekova, Henry Hsieh, Meg Schwamb. Thank you for uplifting me as a researcher and for providing me with opportunities and invaluable feedback that have allowed me to continue my scientific pursuits beyond graduate school. I want to thank my groupmates: Harrison, Julian, and Joe, for welcoming an observer into theory-land. I am a better scientist because of our great discussions.

I'd like to give special thanks to the most supportive group of fellow graduate students, especially the queerstros and the DND crew. I've enjoyed all of the time we've spent together and will always remember it fondly. I've been incredibly fortunate to have the greatest officemates: Becca, Ginny, Tomás, and Joe. Thank you for all of your support and for answering my endless science questions with enthusiasm every time. Each one of you has become a true friend. To my grad school partner in crime, Liz, I'm thankful to have shared my graduate experience with you. Your friendship has meant so much more to me than I can express. I want to give an extra thanks to Liz, Teal, Rick, and Drew for reading drafts and sending reassurances.

I'd like to send a huge thank you to my friends, near and far, who provided frequent escapes from graduate school and never stopped sending me encouragement: Justin, Angela, Dylan, Amelia, Kelsey, Jes, Erika, and so many others.

I want to give special thanks to my parents: Connie and Andy. Mom - thank you for your unconditional love and support. Words cannot adequately convey how much I appreciate everything you've done for me over the last seven years. Dad - thank you for your genuine interest in my work. Your enthusiasm for space is a big part of how I ended up here. I'd like to give a big appreciation to my step-parents: Kim and Steve, and my

siblings: Charlie, Emily, and Abby for all of your love and support. And thank you to my extended family members. I'd also like to thank my future brother and sister-in-law, Jonathan and Ellie, for providing always-needed couch hangs and glasses of whiskey, but also for having the cutest baby and making me an aunt. Pictures of Nina's smiling face have made these last stressful months much more bearable.

I have to acknowledge my dog, Orion, who has been with me since the beginning of my second year and can always turn my worst days around with his unconditional love and cozy snugs.

I want to end by thanking my future-wife, Victoria. Your love and support means more to me than I can possibly put into words. Thank you for your constant reassurance and for always believing in me. Thank you for listening to me ramble about comets and rant about my broken code. Thank you for keeping me fed and single-handedly running our household for the past several months. There's no way I would have made it to the finish line without you. Sharing a life with you has been the greatest gift – I love you, V.

Table of Contents

List of Tables

List of Figures

List of Abbreviations

COBS	Comet OBServation Database
CODE	Catalog of Cometary Orbits and their Dynamical Evolution
DCT	Discovery Channel Telescope
DIA	Difference Image Analysis
DNC	dynamically new comet
ER	escape region
FOV	field-of-view
FWHM	Full Width at Half Maximum
INT	Isaac Newton Telescope
JFC	Jupiter-family comet
JPL	Jet Propulsion Laboratory
KDE	kernel density estimation
LCO	Las Cumbres Observatory
LDT	Lowell Discovery Telescope
LMI	Large Monolithic Imager
LOOK	LCO Outbursting Objects Key Project
LPC	Long-period comet
LSST	Legacy Survey of Space & Time
MOC	Moving Object Catalog
NEA	Near-Earth Asteroid
NEAR	Near-Earth Asteroid Rendezvous
NEATM	Near-Earth Asteroid Thermal Model
NEO	Near-Earth Object
NEOSM	Near-Earth Object Surveyor Mission
NEOWISE	Near-Earth Object Wide-Field Infrared Survey Explorer

OCC	Oort cloud comet
OSIRIS–REx	Origins, Spectral Interpretation, Resource Identification, Security, Regolith Explorer
PS1	Pan-STARRS Data-Release 1
SDSS	Sloan Digital Sky Survey
SNR	signal-to-noise ratio SOAR
Southern Astrophysical Research	
SOHO	Solar and Heliospheric Observatory
SOI	SOAR Optical Imager
STEREO	Solar Terrestrial Relations
WCS	World Coordinate System
WISE	Wide-field Infrared Survey Explorer
WFC	Wide-Field Camera
YORP	Yarkovsky–O'Keefe–Radzievskii–Paddack

Chapter 1: Introduction

1.1 Small Bodies as a Window into the Early Solar System

Small bodies (i.e., asteroids and comets) play a unique role in our understanding of the Solar System. As the pre-solar nebula collapsed into the protoplanetary disk, particles began to collide and stick to other grains, eventually accreting into larger bodies called planetesimals, ranging in size from meters to kilometers (Lunine & Gautier, 2004). In the inner regions, where temperatures were high, rocky planetesimals formed through the accumulation of primarily silicate-rich material (Öberg & Bergin, 2021, Figure 1.1). In the outer regions, volatile gases condensed onto dust grains depending on their location in the disk and the condensation temperature of the gas. These planetesimals served as the building blocks for the planets and the leftovers formed asteroids, comets, and other small bodies. Because these smaller bodies did not undergo as much processing (such as differentiation and atmospheric weathering), their primitive nature provides unique insight into the formation and evolution of the Solar System.

Small bodies today do not originate in the same regions where they formed. Studies have suggested that the giant planets underwent significant radial movements during their early formation, which affected the current distribution of objects (e.g., Tsiganis et al., 2005; Gomes et al., 2005; Levison et al., 2011; Walsh et al., 2011). The gravitational interactions

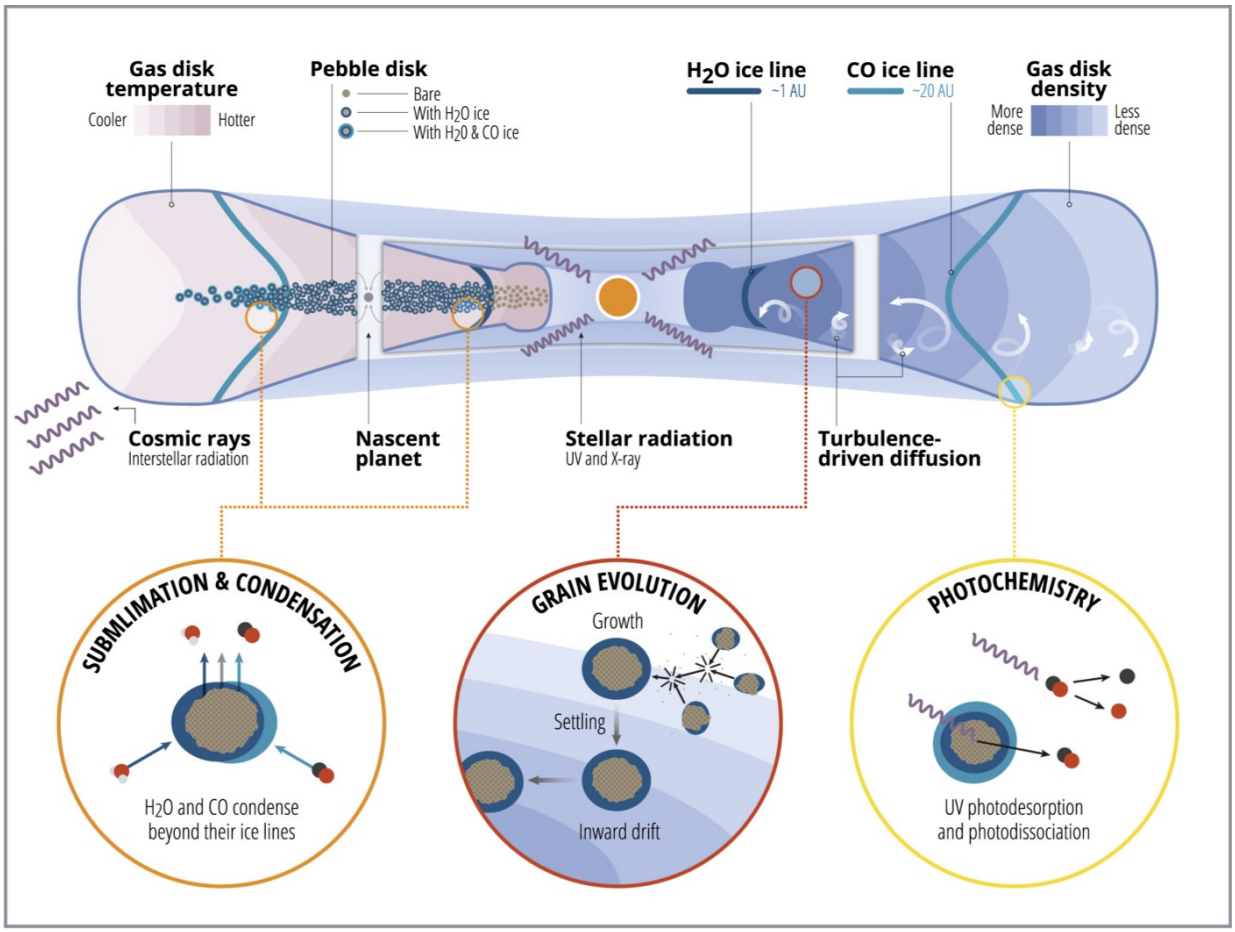

Figure 1.1: **From Öberg & Bergin (2021):** Cartoon of protoplanetary disk chemistry and its coupling to different gas and grain dynamical processes.

among the planets caused small bodies to scatter inward or outward from their original formation locations, disrupting the initial configuration of the disk.

1.1.1 The Thesis in Context

Comets and asteroids contain material characteristic of their formation region. However, they have undoubtedly undergone some degree of processing since then. The overarching motivation for small body science is to disentangle primordial characteristics from evolutionary ones with the goal of better understanding how our Solar System came to be.

This work seeks to tackle a piece of this goal by studying end member populations: the most and least thermally processed objects.

Chapter 2 characterizes the surface alteration of near-Sun asteroids and constrains the dominant mechanisms responsible. Chapters 3 and 4 investigate the brightness evolution of dynamically new comets and how it relates to processes on the surface. Finally, Chapter 5 summarizes our findings and describes upcoming work.

In this introduction, we describe our main observational method of broadband optical photometry in Section 1.2. We then introduce the subjects of the subsequent chapters: near-Sun asteroids in Section 1.3 and dynamically new comets in Section 1.4. The background and motivations for Chapters 3 and 4 are largely the same, so to avoid redundancy, we introduce those concepts in the introduction and spend less time introducing near-Sun asteroids. Detailed context for our near-Sun asteroids work is covered within Chapter 2.

1.2 Broadband Optical Photometry

This work employs one of the most basic astronomical methods of photometry, which measures the amount of light emitted or reflected from an object at a specific time and over a specific wavelength range. We use broadband optical filters which only transmit light within broad spectral bands in the visible region of the spectrum (roughly $\sim$ 0.4–0.8 μm). Commonly used filters include SDSS-*ugriz* (Fukugita et al., 1996) and Johnson-Cousins *UBVRI* (Bessell, 2005). Optical photometry can be conducted using relatively small and portable telescopes, making it accessible to a wide range of astronomers and researchers.

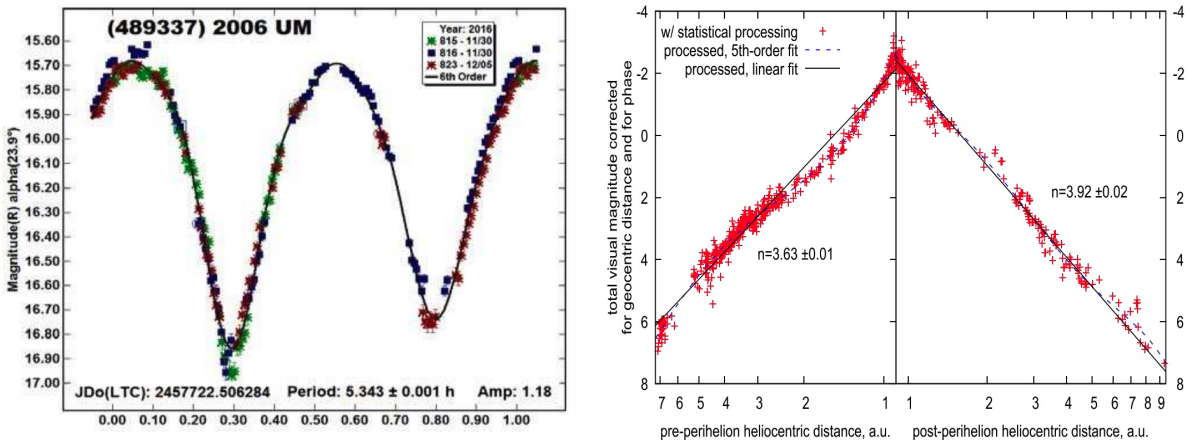

Figure 1.2: **Left:** from Carbognani (2017), the rotational light curve of asteroid (489337) 2006 UM, where each point is an observation phased to a rotational period and the colors represent different observatories. The red points were collected on a separate date from the others. **Right:** from Womack et al. (2021), the heliocentric light curve of comet C/1995 O1 (Hale-Bopp) in log-scale, where the left side shows the brightness variation as the comet approaches the Sun and the right side as the comet travels away from the Sun.

1.2.1 Time-Series Photometry

One of the primary applications of photometry of small bodies is the determination of temporal variations in brightness (Figure 1.2). By monitoring the changes in brightness over time, we can constrain the rotational period of inactive objects. The rotational period provides valuable insights into the internal structure and dynamics of inactive objects, helping to discern their shape and composition. For comets, we can use time-series photometry to monitor how brightness changes across a wide range of heliocentric distance to assess the drivers of activity, which contributes to our understanding of the processes occurring on the comet surface.

1.2.2 Broadband Color Analysis

By subtracting the magnitude in one filter from another, we can evaluate the spectral color, which represents the brightness ratio between different regions of an object's spectrum. For example, $g - r$ is the magnitude in the g filter minus the magnitude in r. This approach provides a more accessible characterization of the spectrum, albeit with less detailed information, compared to spectroscopy. In doing so, we gain insights into the color variations of objects over time and between populations. This enables a broader understanding of the spectral properties of small bodies.

The colors provide valuable information about the reflective properties and composition of asteroid surfaces. Different materials have distinct spectral signatures, causing variations in the colors observed. Spectral colors can contribute to the determination of an asteroid's type, which is related to its composition (Figure 1.3). Colors can also be used to assess spectral slope variations caused by surface processing, which is what we focus on in Chapter 2.

For active comets, we can use spectral colors to separate the contributions of gas versus dust in the coma. As shown in Figure 1.4, the SDSS-g filter contains several of the strong cometary gas emission lines, while the SDSS-r filter is mostly free of such lines. This technique can be used to assess how the gas production changes as the comet passes closer to the Sun, allowing us to better understand the mechanisms behind cometary activity.

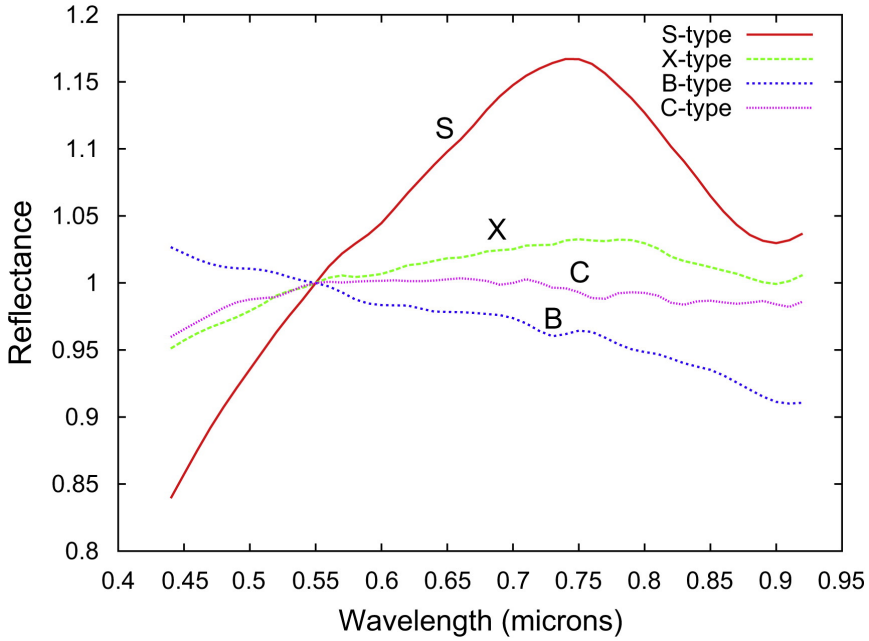

Figure 1.3: **From Delbó et al. (2012):** Example of the visible reflectances of asteroids obtained from the Small Main Belt Asteroid Spectroscopic Survey (SMASS). Each spectrum is accompanied by a letter denoting the respective asteroid's spectral type.

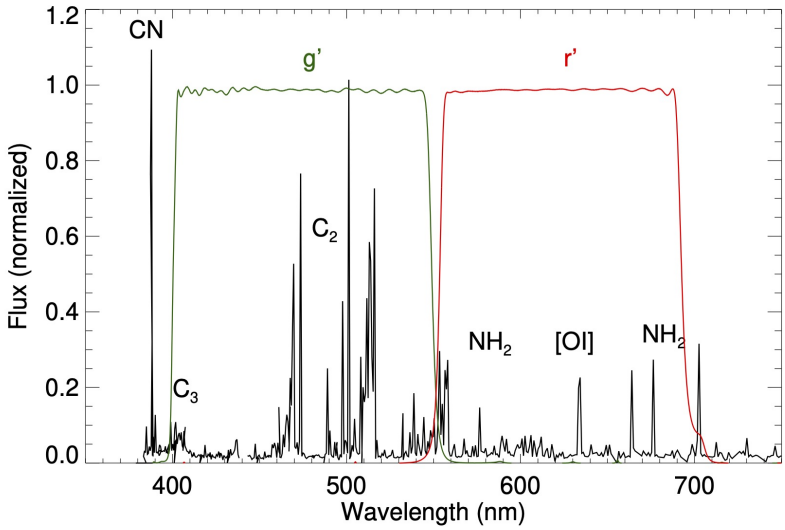

Figure 1.4: **From Lister et al. (2022):** Cometary gas emission lines shown in the spectrum of 122P/de Vico (Cochran & Cochran, 2002) overlapped by the transmission spectra of the SDSS g and r filters. The continuum was not removed by Cochran & Cochran (2002), as 122P had a very high gas-to-dust ratio and the continuum was negligible compared to the emission lines. The r filter (red) is minimally affected by the strongest cometary gas emission lines, while the g (green) filter captures a substantial number of them. This enables reliable measurements of the separate distributions of gas and dust.

1.3 Near-Sun Asteroids

Many comets and asteroids spend part of their dynamical lifetimes as near-Sun objects with small perihelion distances (< 0.3 au) as a result of dynamical interactions with Jupiter (e.g., Bailey et al., 1992; Farinella et al., 1994; Gladman et al., 1997; Bottke et al., 2002; Marchi et al., 2009; Greenstreet et al., 2012). Near-Sun objects are a unique population that has arguably experienced the most extreme conditions of any small body, sometimes reaching temperatures of 1000–1500 K, where silicates (i.e., the minerals that make up rocks) begin to sublimate (see review by Jones et al., 2017). The extreme environment makes them prone to fragmentation or disruption, although the exact mechanism remains unknown (e.g., Bortle, 1991; Granvik et al., 2016). Our motivation is to comprehend the effects of intense thermal processing and uncover the cause of these disruptions.

Apart from scientific curiosity, studying Near-Sun asteroids is crucial because they are a subset of Near-Earth Asteroids (NEAs) and have the potential to impact our planet (although there are currently no detected objects with a significant risk of impact in the next 100 years*). Understanding the composition, size, and other characteristics of potential impactors is vital for accurate hazard assessment and mitigation planning. By unraveling the dominant near-Sun processes responsible for disruptions and surface alterations, we can improve our characterization of these objects and enhance preparedness for potential impacts.

Several processes likely contribute to surface processing and potential disruption: 1) Increasing temperatures facilitate the sublimation of additional materials, such as those

*https://cneos.jpl.nasa.gov/sentry/

from deeper surface layers, as well as less volatile substances. The sublimation causes outgassing, ejecting material from the nucleus. 2) Near-Sun asteroids are expected to experience more planetary encounters, and therefore tidal forces that disturb the surface (e.g., Nesvorný et al., 2005; Marchi et al., 2006b; Binzel et al., 2010; Nesvorný et al., 2010; DeMeo et al., 2014; Carry et al., 2016; Devogèle et al., 2019). 3) The Yarkovsky-O'Keefe-Radzievskii-Paddack (YORP) effect, characterized by asymmetrical radiative torques, can increase the spin rate of irregular-shaped asteroids (Bottke et al., 2006), potentially leading to the centrifugal loss of material (Rubincam, 2000; Vokrouhlický et al., 2015). 4) Diurnal temperature variations can induce thermal fatigue, causing boulders and grains to fracture and break down into smaller regolith (Jewitt, 2012; Delbo et al., 2014). The OSIRIS-REx mission observed such thermal cracking on asteroid Bennu (Molaro et al., 2020). 5) Impacts by high-speed near-Sun meteoroids have been suggested to cause surface alteration (Wiegert et al., 2020).

1.4 Dynamically New Comets

Observed comets are separated into two main types: Jupiter family comets (JFCs), which evolve from the trans-Neptunian region, and long-period comets (LPCs), which are perturbed inward from the Oort cloud by passing stars and galactic tides. When a comet enters the inner Solar System ($r_h \lesssim 40$ au), solar irradiation will induce the outgassing of volatiles, which can cause cometary nuclei to undergo physical changes (e.g., Vincent et al., 2016), as well as chemical changes (e.g., A'Hearn et al., 2011). JFCs have undergone numerous orbits within the inner solar system, resulting in observable evolutionary properties

that are consistent with prolonged exposure to temperatures well above the sublimation point of water. Some LPCs with highly elongated orbits spanning hundreds to thousands of years have had previous passages through the inner Solar System and are therefore similarly processed to JFCs. LPCs entering the inner Solar System for the first time are considered to be "dynamically new" comets (DNCs). DNCs are valuable probes for connecting observed cometary properties to conditions in the pre-solar nebula and subsequent evolution, as they are considered to be mostly primordial with limited solar heating prior to discovery.

1.4.1 Dynamical Definition

DNCs are a statistical subset of long-period comets (LPCs) distinguished by their orbital properties. Historically, the original orbital energy has been used as the main diagnostic. The original orbital energy of an LPC is proportional to the inverse of the original semi-major axis, $1/a_0$, calculated by integrating the orbit backward in time until it reaches a distance from the Sun where planetary perturbations are negligible ($\sim$ 250 au). The distribution of $1/a_0$ shows an excess of comets with $a_0 > 10^4$ au. This "spike" led to the postulation of the Oort Cloud (Oort, 1950).

However, not all comets in the Oort spike are truly pristine. $1/a_0$ does not directly correlate with previous perihelion distance q_{prev}, though comets with $1/a_0 < 3 \times 10^{-5}$ au^{-1} are more likely to have $q_{prev} > 20$ au (Figure 1.5). M. Królikowska and P. A. Dybczyński have dedicated decades of research to the dynamical modeling of long-period comets (e.g., Królikowska & Dybczyński, 2010, 2013; Dybczyński & Królikowska, 2015; Królikowska & Dybczyński, 2017). Their models, reported in the CODE Catalog[†], which we discuss in-

[†]`https://pad2.astro.amu.edu.pl/comets/`

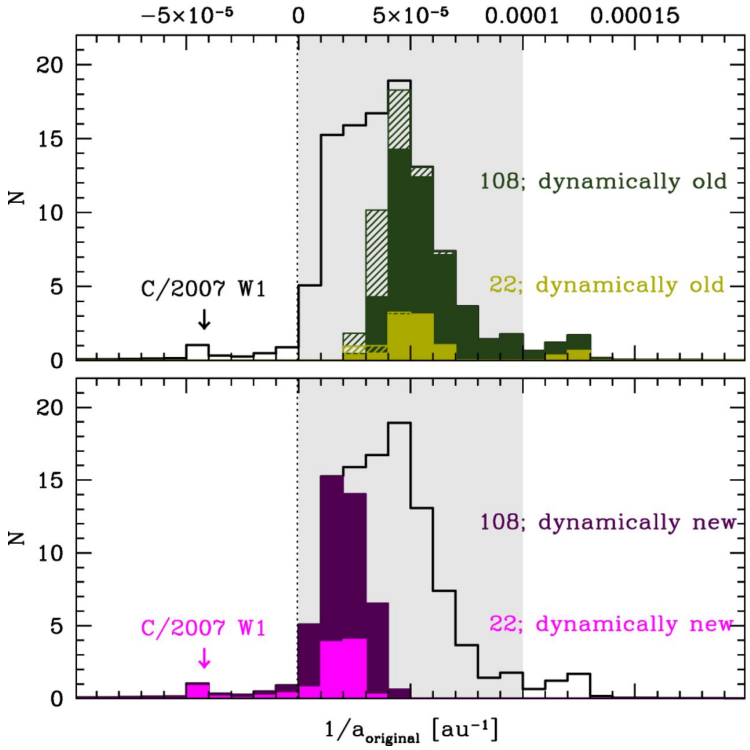

Figure 1.5: **From Dybczyński & Królikowska (2015):** The distribution of "new" verses "old" comets in the "Oort spike", where "old" is defined as having $q_{prev} < 20$ au. A previous misconception is that all comets in the Oort spike are dynamically new. However, it is most likely that only a small subset are.

depth in Chapter 4, cover the orbital evolution of Oort spike comets during three consecutive perihelion passages: previous, observed, and next, typically over 1–10 million years, calculating parameters such as $1/a_0$ and the previous perihelion distance (q_{prev}). This type of extensive modeling is not trivial. An accurate $1/a_0$ value requires a long data arc and the determination and implementation of nongravitational accelerations (Królikowska & Dybczyński, 2013). Conducting further reverse orbit integrations to determine the previous perihelion distance q_{prev} can give a more precise look at the prior heating experienced by these objects (Dybczyński & Breiter, 2022). However, such integrations require the implementation of galactic tides and stellar perturbers (Dybczyński & Królikowska, 2022).

1.4.2 Previous Studies

Differences in the rate of brightening between new and returning comets were initially observed shortly after the establishment of the Oort cloud. After analyzing the brightness behavior of approximately 50 LPCs, Oort & Schmidt (1951) reported that comets originating from the Oort spike exhibited a slower increase in brightness compared to returning comets. Subsequently, Whipple (1978) conducted a study of over 100 comets based on observations spanning over a century and discovered a correlation between the rate of brightening and dynamical age, whereby older comets experienced a more rapid increase in brightness. A'Hearn et al. (1995), in an extensive study of comets, albeit with a smaller sample size, observed a similar trend in the brightening of gas production rates (OH, CN, C_2, C_3, and NH) as well as dust. These studies primarily focused on observations made when the comets were within 3 au of the Sun, a region where activity is driven by the sublimation of water ice. The work discussed in Chapters 3 and 4 extends to larger heliocentric distances than previous work.

Chapter 2: Surface Properties of Near-Sun Asteroids

2.1 Introduction

2.1.1 Background

Many comets and asteroids spend part of their dynamical lifetimes with small perihelion distances (or "low-q") as a result of dynamical interactions with Jupiter (e.g., Bailey et al., 1992; Farinella et al., 1994; Gladman et al., 1997; Bottke et al., 2002; Marchi et al., 2009; Greenstreet et al., 2012). However, even while assuming a loss due to collisions with the Sun or planets, or an escape from the inner solar system, Granvik et al. (2016) reported a deficit of asteroids with small perihelion distances ($q \lesssim 0.5$ au), which they attributed to "super-catastrophic disruption" on timescales of less than 250 years when an asteroid reaches a perihelion distance less than $q \sim 0.076$ au, with some dependence on asteroid size. Based on the evolution of debris streams, Ye & Granvik (2019) suggest that disruption is a more gradual process with timescales of $1 - 20$ kyr. Granvik et al. (2016) determined that the disruption of near-Sun asteroids cannot be explained by tidal effects or thermal vaporization. Potential near-Sun processes that might lead to disruption over time (e.g., thermal cracking, spin-up, subsurface volatile release) likely cause surface alteration, which might be observable from the ground using optical telescopes.

2.1.2 Observed Trends

Low-q comets 322P/SOHO 1, 96P/Machholz 1 and 323P/SOHO have been observed to have atypical blue colors (Knight et al., 2016; Eisner et al., 2019; Hui et al., 2022). 322P/SOHO 1 has a cometary orbit and shows evidence of being active at perihelion (Lamy et al., 2013), but it has an asteroid-like albedo, density, and fast rotation. 96P/Machholz 1 had the smallest perihelion distance of any unambiguously active short-period comet until recent observations of 323P/SOHO, which was observed post-perihelion with a long-narrow tail, likely caused by immense thermal stress or rotational instability; 323P has the shortest rotational period of known comets in our Solar System at 0.522 hrs. 323P/SOHO 1 was recently observed to have bluer colors than most Solar System small bodies, which changed unprecedentedly over a few weeks to a color unlike any other small bodies in our Solar System (Hui et al., 2022). Further characterization of objects with small perihelion distances is necessary to assess whether these comets are unique or if their bluer colors are typical of objects that closely approach the Sun. Very few periodic comets are observed from the ground with a perihelion distance less than 0.15 au, so additional observations must focus on asteroids.

Spectral trends with perihelion distance have been observed for S- and Q-type near-Earth asteroids (NEAs) with $q \gtrsim 0.2$ au. Marchi et al. (2006a) observed that S- and Q-types become spectrally bluer with decreasing perihelion distance using data from Binzel et al. (2004) and Lazzarin et al. (2004, 2005), which they attribute to resurfacing caused by close encounters with planets. Because of their closely related spectra, only different in features impacted by space weathering (spectral slope and 1-μm band depth), Q-types are best

explained as resurfaced S-types that have not yet had enough time for space weathering to alter their surface (e.g., Chapman, 2004; Brunetto et al., 2015). In agreement with Marchi et al. (2006a), DeMeo et al. (2014) and Devogèle et al. (2019) found a higher percentage of Q-type asteroids (which are spectrally bluer than S-types) with smaller perihelion distances. Graves et al. (2019) argue that resurfacing due to thermal degradation explains the trend better than planetary encounters after modeling NEA orbits and tracking spectral slope with planetary encounters or physical distance from the Sun for each object. More observations of near-Sun asteroids are needed to determine if this trend holds at smaller perihelion distances.

2.1.3 Overview of Known Properties

This work presents an observational study of known near-Sun asteroids and searches for any common properties that might be related to near-Sun processes experienced by these objects. We focus our efforts on objects with perihelion distance $q \leq 0.15$ au. We chose this limit because 0.15 au is the outer limit of the Solar and Heliospheric Observatory (SOHO)'s outermost coronagraph (C3)'s field-of-view, meaning we can potentially view activity or disruption of these objects using SOHO. There are 53 known asteroids that reach perihelion at $q \leq 0.15$ au (sub-solar temperatures $\gtrsim 1000$ K) as of November 1, 2021, including the ones with poorly constrained orbits. All of the objects reach perihelion within the SOHO field of view each orbit, yet none have been observed to date, meaning that mass loss near perihelion has been very low over the last quarter century (to be explored further in Section 2.4.3).

Campins et al. (2009) and Jewitt et al. (2013) investigated a similar set of asteroids, but their perihelion distance limits were significantly larger ($q \leq 0.35$ au and ≤ 0.25 au, respectively). Only seven of their objects are in our sample. Most low-q asteroids are small and therefore faint and difficult to study. In-depth studies have not been possible for low-q objects other than 3200 Phaethon. While there have been a few serendipitous observations as part of general NEO studies, the available data are still limited, as detailed below and summarized in Table 2.1.

2.1.3.1 3200 Phaethon

Phaethon is the most studied low-q asteroid because it is the largest among the sample (diameter ∼5 km) and has a short orbital period (1.43 yr), allowing for observations nearly every apparition, including a historically close approach to Earth in 2017. The parent body of the Geminid meteor shower (Whipple, 1983), Phaethon is the only known unambiguously active low-q asteroid (Jewitt & Li, 2010; Jewitt, 2013; Li & Jewitt, 2013; Hui & Li, 2017) and the only named asteroid that approaches within 0.15 au of the Sun. Phaethon is a B-type asteroid (Binzel et al., 2001) with an albedo of ∼0.16 (Masiero et al., 2019) and a rotational period of ∼3.6 hours (Warner, 2015a). Spectroscopy and colors have been measured extensively (most recently by Lin et al. 2020). The Japanese space agency JAXA's forthcoming DESTINY$^+$ mission is expected to fly by Phaethon in 2024 (Ozaki et al., 2022).

Table 2.1: Published Measurements of Near-Sun Asteroids*

Object	$B-V$	$V-R$	$B-R$	Ref.	Rotation Rate [hrs]	Ref.	Albedo	Size [km]	Ref.
1995 CR	-	-	-	-	2.66 ± 0.04	1	$0.167\pm^{0.101}_{0.079}$	$0.129\pm^{0.045}_{0.024}$	2
2000 BD19	-	-	-	-	10.570 ± 0.005	3	0.247 ± 0.046	0.97 ± 0.04	4
							$0.123\pm^{0.082}_{0.066}$	$1.149\pm^{0.513}_{0.241}$	5
2000 LK	-	-	-	-	-	-	$0.137\pm^{0.092}_{0.074}$	$0.610\pm^{0.278}_{0.132}$	5
2002 AJ129	0.687 ± 0.050	0.405 ± 0.027	1.092 ± 0.057	6	3.9222 ± 0.0008	6	$0.226\pm^{0.141}_{0.116}$	$0.438\pm^{0.181}_{0.091}$	5
	-	-	1.23 ± 0.10	7	-	-	-	-	-
2002 PD43	0.66 ± 0.05	0.42 ± 0.05	1.08 ± 0.03	7	-	-	-	-	-
2004 UL	0.82 ± 0.10	0.54 ± 0.10	1.37 ± 0.10	7	38 ± 2	8	$0.604\pm^{0.258}_{0.264}$	$0.268\pm^{0.083}_{0.042}$	5
2004 XY60	-	-	-	-	-	-	$0.217\pm^{0.137}_{0.110}$	$0.389\pm^{0.161}_{0.080}$	5
2006 HY51	-	-	-	-	3.350 ± 0.008	9	0.157 ± 0.071	1.218 ± 0.23	4
2006 TC	0.60 ± 0.08	0.33 ± 0.03	0.93 ± 0.08	7	-	-	-	-	-
2007 EP88	-	-	-	-	-	-	0.174 ± 0.038	0.636 ± 0.04	4
							$0.531\pm^{0.236}_{0.230}$	$0.312\pm^{0.098}_{0.051}$	5
2008 HE	-	-	-	-	-	-	$0.120\pm^{0.091}_{0.066}$	$0.779\pm^{0.375}_{0.184}$	10
2008 MG1	-	-	-	-	-	-	$0.431\pm^{0.252}_{0.223}$	$0.194\pm^{0.084}_{0.038}$	10
2008 XM	-	-	-	-	-	-	0.128 ± 0.032	0.367 ± 0.01	4
2010 JG87	-	-	-	-	-	-	0.202 ± 0.040	0.408 ± 0.02	4
2011 KE	-	-	-	-	8.0 ± 0.1	11	-	-	-
2011 XA3	-	0.473 ± 0.051**	-	12	0.730 ± 0.007	12	$0.347\pm^{0.196}_{0.163}$	$0.163\pm^{0.056}_{0.029}$	10
2017 AF5	-	-	-	-	49.68 ± 0.06	13	-	-	-
3200 Phaethon	0.67 ± 0.02	0.32 ± 0.02	0.99 ± 0.02	7	3.6039 ± 0.0002	14	0.16 ± 0.02	4.6 ± 0.3	15

References –(1) Warner (2014) ; (2) Trilling et al. (2016b) (3) Warner (2015b); (4) Mainzer et al. (2011, 2016); (5) Trilling et al. (2010); (6) Devyatkin et al. (2022); (7) Jewitt (2013); (8) Warner (2015a); (9) This work; (10) Trilling et al. (2016a); (11) Skiff, B.A. (2011)[a](12) Urakawa et al. (2014); (13) Warner (2017); (14) Warner (2015a);(15) Masiero et al. (2019)

* All uncertainty values are presumed 1-σ errors
** Converted from $g' - r'$ according to Jordi et al. (2006)
[a] Posting on CALL web site. `http://www.minorplanet.info/call.html`

2.1.3.2 Albedos

Near-Earth Object Wide-Field Infrared Survey Explorer (NEOWISE), an infrared characterization survey, has measured diameters and determined albedos for 2000 BD19, 2006 HY51, 2007 EP88, 2008 XM, and 2010 JG87 (Mainzer et al., 2011, 2016). Albedos were derived by combining infrared measurements with previously reported or follow-up optical magnitudes using the Near-Earth Asteroid Thermal Model (NEATM; Harris, 1998). Additional albedo measurements were made using the Spitzer Space Telescope via the ExploreNEOs (Trilling et al., 2010) and NEOSurvey (Trilling et al., 2016b) infrared char-

acterization surveys. We include both NEOWISE and Spitzer albedos in Table 2.1 for completeness, but we caution the use of Spitzer measurements with reported albedos that are larger than the assumed NEO upper limit of ~ 0.5 (Gustafsson et al., 2019).

2.1.3.3 Rotation Periods

Rotation rates have been measured for eight low-q asteroids, including Phaethon. All objects except 2011 XA3 have rotation rates ranging from ∼2.5 hours (1995 CR; Warner, 2014) to ∼2 days (2017 AF5; Warner, 2017). 2011 XA3 is the exception with a fast rotation rate of ∼45 minutes (Urakawa et al., 2014). We discuss this object further in Section 2.4.4.

2.1.3.4 Spectral Properties

Spectral observations are limited for the low-q population. Three objects in addition to Phaethon have measured IR spectra and classification: 137924 (2000 BD19) is V type, 394130 (2006 HY51) is R-type, and 465402 (2008 HW1) is S-type (Thomas et al., 2014; Binzel et al., 2019). The variety of taxonomies is interesting to note considering the majority of NEAs are S-type, while V- and R- types only make up $\sim 5\%$ of the NEA population (Binzel et al., 2019).

Campins et al. (2009) measured the 7-14 μm thermal emission spectra of 19 asteroids with $q \leq 0.35$ au, including two objects with $q \leq 0.15$ au: 2000 BD19 and 2004 XY60. They fit the spectra with thermal continuum models to derive effective diameter, geometric albedo, and beaming parameter of these objects and suggest that thermal behavior is different for near-Sun asteroids compared with other NEAs (stronger thermal emission

"beaming" at low phase angles). Jewitt et al. (2013) measured the colors of nine asteroids with $q \leq 0.25$ au to search for evidence of thermal modification. Five of the objects have $q \leq 0.15$ au and are therefore a part of our sample. They found that near-Sun objects have a wide range of colors, but there was no statistical distinction between such objects and other near-Earth objects. Both Campins et al. (2009) and Jewitt et al. (2013) consider objects beyond our perihelion cutoff of 0.15 au and suggest further characterization is needed.

2.1.4 This Work

Near-Sun asteroids have not been thoroughly examined as a population. Color observations can provide us with a better understanding of the processes occurring and the effects they have on near-Sun asteroids. Broadband optical colors (e.g., $g' - r'$, $r' - i'$) can be obtained quickly and for fainter objects, which makes such observations optimal for a population study. Over more than three years of observations from January 2017 to March 2020, we attempted to observe as many near-Sun asteroids as possible. Of the 53 known asteroids with $q \leq 0.15$ au (summary of orbital elements in Table 2.2), we attempted to observe 35, and successfully observed 22. Nine of the objects we attempted to observe were predicted to be within our fields of view and above our detection limit but were not recovered, most likely due to the very large uncertainty in their orbits. We also observed near-Earth asteroid 2004 LG, which previously spent 2500 years with a perihelion distance less than 0.076 au, the disruption limit of Granvik et al. (2016), experiencing extreme temperatures of ~ 2500 K at the surface (Vokrouhlický & Nesvorný, 2012; Wiegert et al., 2020).

Table 2.2: Near-Sun Asteroid Properties[a]

			Orbital Elements[b]								Source Region Probabilities[c]								
	Object	H_V[d]	q	a	e	i	T_J	U[e]	$T_{BB}(q)$[f]	$T_{SS}(q)$[g]	ν_6	5:2	2:1	Hun	3:1	Pho	JFC	T_{q*}[h]	Status[i]
	(2005 HC4)	20.7	0.070	1.824	0.961	8.4	3.17	9	1048	1482	**0.76**	0.04	0.00	0.01	0.18	0.00	0.00	-[j]	A
	(2020 BU13)	21.2	0.073	2.471	0.970	9.2	2.44	6	1028	1454	0.18	0.11	0.00	0.00	**0.69**	0.00	0.01	-	X
	(2017 TC1)	20.9	0.076	2.491	0.970	9.3	2.42	8	1010	1428	0.19	0.13	0.00	0.00	**0.66**	0.00	0.01	-	O[k]
	(2008 FF5)	23.1	0.080	2.272	0.965	2.6	2.64	9	986	1395	**0.62**	0.01	0.00	0.02	0.34	0.00	0.02	-	X
	(2017 MM7)	21.1	0.080	2.064	0.961	23.2	2.84	7	983	1391	**0.63**	0.06	0.00	0.02	0.27	0.02	0.00	-	A
	(2015 EV)	22.5	0.081	2.036	0.960	11.4	2.90	9	980	1386	**0.70**	0.02	0.00	0.02	0.26	0.00	0.00	-	X
394130	(2006 HY51)	17.1	0.081	2.588	0.969	33.6	2.30	0	975	1379	0.08	0.26	0.01	0.01	**0.55**	0.06	0.03	6.1	O
	(2021 AF3)	22.9	0.086	1.301	0.934	7.2	4.35	9	946	1338	**0.89**	0.01	0.00	0.05	0.05	0.00	0.00	-	X
	(2016 GU2)	24.0	0.087	2.052	0.957	10.3	2.89	8	941	1331	**0.68**	0.00	0.00	0.04	0.28	0.00	0.00	-	A
	(2019 AM13)	22.0	0.091	1.296	0.930	16.7	4.37	2	922	1304	**0.78**	0.02	0.00	0.06	0.14	0.00	0.00	-	O
	(2019 JZ6)	21.0	0.091	2.461	0.963	24.1	2.45	9	921	1303	0.12	0.15	0.01	0.00	**0.70**	0.01	0.01	-	X
137924	(2000 BD19)	17.4	0.092	0.876	0.895	25.7	6.27	0	917	1297	**0.52**	0.00	0.00	0.33	0.13	0.01	0.00	7351.8	O
374158	(2004 UL)	18.7	0.093	1.266	0.927	23.8	4.45	0	913	1291	**0.80**	0.03	0.00	0.06	0.09	0.02	0.00	157.0	O
394392	(2007 EP88)	18.5	0.096	0.837	0.886	20.7	6.56	1	900	1273	**0.74**	0.00	0.00	0.14	0.11	0.01	0.00	13687.6	O
	(2011 KE)	19.8	0.100	2.207	0.955	5.9	2.74	1	879	1243	**0.75**	0.05	0.00	0.01	0.19	0.00	0.00	4.0	O
465402	(2008 HW1)	17.4	0.103	2.587	0.960	10.5	2.40	0	865	1224	0.14	0.24	0.01	0.00	**0.55**	0.02	0.04	6.7	O
	(2015 HG)	21.0	0.105	2.102	0.950	17.7	2.85	9	859	1215	**0.62**	0.05	0.00	0.01	0.30	0.02	0.00	4.9	A
	(2012 US68)	18.3	0.106	2.503	0.958	25.8	2.44	2	856	1210	0.11	0.29	0.03	0.00	**0.51**	0.04	0.01	3.7	A[l]
	(2011 XA3)	20.4	0.109	1.467	0.926	28.0	3.90	0	844	1193	**0.76**	0.03	0.00	0.05	0.15	0.02	0.00	1319.4	X
399457	(2002 PD43)	19.1	0.109	2.507	0.956	26.0	2.44	0	841	1189	0.11	0.28	0.03	0.00	**0.53**	0.03	0.01	2.9	O
	(2018 GG5)	19.8	0.110	1.986	0.945	16.8	3.01	7	840	1187	**0.71**	0.03	0.00	0.01	0.23	0.02	0.00	36.4	O
386454	(2008 XM)	20.0	0.111	1.222	0.909	5.4	4.66	0	834	1180	**0.84**	0.03	0.00	0.02	0.11	0.00	0.00	96.9	O
431760	(2008 HE)	18.1	0.112	2.262	0.950	9.8	2.70	0	831	1175	**0.68**	0.08	0.00	0.01	0.21	0.00	0.01	8.4	O
	(2020 DD)	23.5	0.116	2.483	0.953	2.3	2.51	8	818	1156	0.22	0.01	0.00	0.01	**0.68**	0.00	0.08	-	X
276033	(2002 AJ129)	18.7	0.116	1.371	0.915	15.5	4.20	0	815	1153	**0.84**	0.03	0.01	0.05	0.06	0.01	0.00	88.3	O
	(2020 GB2)	21.1	0.117	2.338	0.950	15.2	2.63	7	814	1152	0.42	0.09	0.00	0.01	**0.48**	0.00	0.00	1.1	X
	(2019 VE3)	23.3	0.117	1.174	0.901	2.5	4.85	9	814	1151	**0.70**	0.00	0.00	0.04	0.26	0.00	0.00	-	X
425755	(2011 CP4)	21.2	0.118	0.912	0.870	9.5	6.11	0	809	1144	**0.95**	0.00	0.00	0.02	0.02	0.01	0.00	2111.9	O
	(1995 CR)	21.8	0.119	0.907	0.868	4.1	6.15	0	805	1139	**0.98**	0.00	0.00	0.02	0.00	0.00	0.00	190.2	O
	(2000 LK)	18.3	0.121	2.184	0.945	16.6	2.79	0	801	1132	**0.66**	0.07	0.00	0.02	0.21	0.04	0.00	19.9	O
	(2007 GT3)	19.7	0.122	2.006	0.939	25.6	2.98	2	796	1126	**0.66**	0.09	0.00	0.02	0.19	0.04	0.00	5.8	A[m]
	(2020 HY2)	24.9	0.124	2.314	0.946	11.4	2.67	9	788	1115	0.43	0.00	0.00	0.03	**0.50**	0.00	0.05	-	X
	(2017 AF5)	17.8	0.124	2.480	0.950	20.9	2.50	0	788	1115	0.13	0.27	0.02	0.00	**0.53**	0.04	0.01	4.5	O
	(2004 QX2)	21.7	0.125	1.286	0.903	19.1	4.45	8	786	1112	**0.82**	0.03	0.00	0.05	0.09	0.00	0.00	16.9	X
	(2019 YV2)	21.9	0.126	1.227	0.897	6.5	4.67	9	783	1107	**0.76**	0.02	0.00	0.03	0.19	0.00	0.00	11.0	X
	(2020 TS2)	18.9	0.126	2.509	0.950	20.1	2.48	8	783	1107	0.12	0.28	0.03	0.00	**0.49**	0.03	0.05	2.9	X
	(2021 LM1)	20.4	0.127	2.312	0.945	29.5	2.63	6	780	1103	0.27	0.13	0.00	0.01	**0.56**	0.03	0.00	2.4	X
	(2011 BT59)	20.9	0.130	2.471	0.947	3.6	2.55	9	771	1091	0.33	0.07	0.00	0.00	**0.54**	0.00	0.04	1.5	A
289227	(2004 XY60)	18.9	0.130	0.640	0.797	23.8	8.52	1	771	1090	**0.88**	0.00	0.00	0.03	0.06	0.03	0.00	622.2	X
	(2015 KO120)	22.0	0.130	1.779	0.927	2.1	3.37	9	770	1089	**0.77**	0.00	0.00	0.02	0.21	0.00	0.00	5.0	A
	(2007 PR10)	20.9	0.132	1.232	0.893	20.9	4.63	1	765	1082	**0.84**	0.04	0.00	0.04	0.07	0.01	0.00	45.2	A[l]
	(2021 PH27)	17.7	0.133	0.462	0.712	31.9	11.62	3	762	1078	**0.76**	0.00	0.00	0.04	0.19	0.01	0.00	2236.6	X
504181	(2006 TC)	18.7	0.136	1.538	0.912	19.6	3.80	1	755	1068	**0.77**	0.00	0.00	0.06	0.14	0.03	0.00	50.6	O
	(2019 UJ12)	22.4	0.137	2.423	0.943	27.5	2.55	8	751	1063	0.08	0.06	0.00	0.00	**0.85**	0.00	0.01	0.2	O
	(2013 JA36)	21.0	0.138	2.665	0.948	42.5	2.29	8	750	1061	0.04	0.36	0.05	0.00	**0.50**	0.02	0.02	1.7	A
	(2008 MG1)	19.9	0.139	0.783	0.823	5.7	7.08	1	746	1056	**0.93**	0.00	0.00	0.06	0.00	0.01	0.00	1685.4	O
	(2013 HK11)	20.7	0.139	2.182	0.936	17.7	2.82	9	745	1053	**0.64**	0.05	0.00	0.01	0.28	0.02	0.00	6.0	A
	(2017 SK10)	21.4	0.140	2.051	0.932	24.5	2.95	9	743	1051	**0.60**	0.06	0.00	0.02	0.30	0.02	0.00	1.2	X
3200 Phaethon	(1983 TB)	14.3	0.140	1.271	0.890	22.3	4.51	0	743	1051	**0.67**	0.06	0.00	0.18	0.06	0.03	0.00	1106.0	O
	(2020 VL4)	18.5	0.142	2.125	0.933	55.8	2.71	8	737	1043	0.18	0.08	0.20	0.03	**0.38**	0.14	0.00	363.6	X
	(2013 YC)	21.4	0.142	2.495	0.943	2.8	2.55	2	737	1043	0.30	0.06	0.00	0.00	**0.59**	0.00	0.04	1.0	O
	(2020 HE)	23.6	0.146	2.515	0.942	20.5	2.51	9	727	1028	0.06	0.01	0.00	0.00	**0.84**	0.00	0.08	-	X
	(2010 JG87)	19.2	0.148	2.768	0.947	16.8	2.33	0	723	1023	0.01	**0.56**	0.08	0.00	0.17	0.01	0.17	2.1	O

[a] As of November 1, 2021
[b] According to JPL Horizons
[c] Probability that the object escaped from each of the six source regions, totaling one, using the model detailed in Granvik & Brown (2018). The source regions consist of the ν_6 inner main-belt region, Jupiter resonance complexes: 3:1, 5:2 and 2:1, the Hungarias, the Phocaeas, and the Jupiter-family comets.
[d] Absolute V magnitude as reported by JPL Horizons
[e] MPC orbit uncertainty estimate. The range is 0-9, with 0 being good and 9 being highly uncertain
[f] Equilibrium isothermal, spherical blackbody temperature at the perihelion distance, K
[g] Equilibrium sub-solar blackbody temperature at the perihelion distance, K
[h] Dwell time with $q \leq 0.15$ au in kyrs according to Toliou et al. (2021)
[i] O: Observed; A: Attempted but not observed; X: Not attempted
[j] Some cells result in a $T_{q*} = 0$ in the Toliou et al. (2021) model after renormalizing each cell of the model according to the relative fraction of NEOs from each ER, as explained in Toliou et al. (2021) Sec. 2.4. We use '-' in those instances.
[k] 2017 TC1 was detected, but was observed in the Milky Way. Colors could not be determined because too few images were obtained for effective DIA (see text).
[l] 2007 PR10 and 2012 US68 were attempted under poor weather conditions
[m] 2007 GT3 had an orbit code of 8 at the time of observations, and was outside the telescope's field-of-view.

2.2 Observations & Data Analysis

2.2.1 Data Collection

Data were collected primarily using Lowell Observatory's 4.3-m Lowell Discovery Telescope (LDT; formerly known as the Discovery Channel Telescope, DCT) and the 4.1-m Southern Astrophysical Research (SOAR) telescope, supplemented by data from the Isaac Newton Telescope (INT) and Lowell Observatory's 42-in and 31-in telescopes. Broadband SDSS g', r', i', z' filters were used at all telescopes except for Lowell Observatory's 31-inch and 42-inch, where Johnson-Cousins *B,V,R,I* filters were used. A summary of the instruments used can be found in Table 2.3. All images were acquired at the asteroid's ephemeris rate, which frequently resulted in trailed stars. Whenever possible, we kept the star trails to less than two times the seeing in order to accurately register the image (see Sec 2.2.4), but for some objects long trails were unavoidable. As will be discussed later, this occasionally hampered absolute calibrations. Exposure times varied with the asteroid's brightness and telescope size, but were typically 180–300 seconds. The number of images acquired for each target varied with time available, though at least two cycles of filters were achieved for all observations, ordered in a way so that the mid-time of the observations for each filter is approximately the same to mitigate rotational variability.

Table 2.3: Instruments

Telescope	Instrument	Aper Size	FOV	Pix Sc[a]	Binning	Filters
Lowell Discovery Telescope (LDT)	Large Monolithic Imager (LMI)	4.3m	$12.3' \times 12.3'$	$0.36''$	3×3	g', r', i', z'
Southern Astrophysical Research (SOAR)	Goodman Spectrograph	4.1m	$7.2'$ diameter	$0.30''$	2×2	g', r', i', z'
Southern Astrophysical Research (SOAR)	SOAR Optical Imager (SOI)	4.1m	$5.26' \times 5.26'$	$0.154''$	2×2	g', r', i', z'
Isaac Newton Telescope (INT)	Wide Field Camera (WFC)	2.5m	$11.5' \times 23.0'$	$0.33''$	None	g', r', i', z'
Lowell Observatory 31-inch	NASAcam	0.8m	$15.7' \times 15.7'$	$0.46''$	None	B, V, R, I
Lowell Observatory 42-inch	NASA42 Camera	1.1m	$25.3' \times 25.3'$	$1.48''$	3×3	B, V, R, I

[a] Effective pixel scale after binning

2.2.2 Instruments

Northern hemisphere targets were primarily observed with Lowell Observatory's 4.3-m LDT located near Flagstaff, AZ. All observations were made using the Large Monolithic Imager (LMI; Massey et al., 2013). LMI has a field-of-view (FOV) of $12.3' \times 12.3'$ and a pixel scale of $0.36''$ after an on-chip 3×3 binning. SDSS broadband g', r', i', and z' filters were used.

Observations of southern hemisphere targets were made using the 4.1-m SOAR Telescope on Cerro Pachón in Chile. The Goodman Spectrograph Red Camera (Clemens et al., 2004) and the SOAR Optical Imager (SOI) were used. The Goodman Spectrograph camera has a circular FOV of $7.2'$ diameter. The observations were done in 2×2 binning mode with an effective pixel scale of $0.30''$. SOI uses two adjacent CCD chips read out through two amplifiers per chip that cover a $5.26' \times 5.26'$ FOV and have a scale of $0.154''$/pixel after 2×2 binning. Broadband g', r', i', and z' SDSS filters were used on all images.

We conducted an observing run in January 2017 using the 2.5-m INT at the Rogue de Los Muchachos Observatory in La Palma, Spain. Observations were made using the Wide Field Camera (WFC), which has an effective FOV of $11.5' \times 23.0'$ and a pixel scale of $0.33''$. All observations used broadband g', r', i', and z' SDSS filters.

Supplemental observations were made using Lowell Observatory's Hall 31-inch (0.8 m) and 42-inch (1.1 m) telescopes. The 31-inch telescope has a square field of view of $15.7'$ on a side and an unbinned pixel scale of $0.46''$. The 42-inch telescope has a square field of view of $25.3'$ on a side and a 3×3 binned pixel scale of $0.98''$. Observations using the 31-inch were robotically acquired. All other telescopes used classic observing mode.

Johnson-Cousins B, V, R, and I filters were used.

2.2.3 Data Reduction

Each observation followed the same reduction routine. A master bias frame for each night was created by averaging 10–20 individual bias frames. The master bias frame was then subtracted from each frame. At least five sky or dome flats taken during the same observing period were normalized and median combined for each filter used. Images were flat-field corrected by dividing each frame by the median-combined flat-field.

2.2.4 Data Analysis

2.2.4.1 Absolute Calibration

Reduced images were registered using `PHOTOMETRYPIPELINE` (Mommert, 2017), which utilizes `SCAMP` (Bertin, 2006) to match the source catalog of an image created by Source Extractor (Bertin & Arnouts, 1996) with astrometric catalogs, such as GAIA. After registration, using `PHOTOMETRYPIPELINE`, photometry was completed on the image sources followed by the derivation of the photometric image zeropoints with the Pan-STARRS DR1 catalog (PS1; Magnier et al., 2013) using field stars. The aperture size was derived using a curve-of-growth analysis, where the optimum aperture radius is the smallest aperture radius where the target and the background fractional fluxes exceed 70% and the difference between the target and background curves is less than 5% (reducing systematic offsets in the flux measurements).

We took our calibration one step further by adding a color correction applied im-

age by image using components of `calviacat` (Kelley & Lister, 2022). The difference between instrumental magnitudes and absolute magnitudes of stars is positively correlated with star color. Using the same in-field stars from the PS1 catalog, we determined the color-correction coefficient. We used the previously determined color to calculate the new absolute magnitude. We repeated this process iteratively until the color converged, usually about three times.

The zeropoints were then converted to either the SDSS photometry system or *BVRI* system depending on the filters used (Tonry et al., 2012). A weighted average of all object magnitudes of the same filter was measured before calculating the difference to determine the object colors. Colors determined in *BVRI* filters were converted to SDSS colors according to Jordi et al. (2006).

As previously discussed, observations were not always acquired during ideal epochs. Therefore, two of the observations (2008 XM and 2018 GG5) include large star streaks ($\sim 15''$) as the telescope tracked the asteroid during long exposures required to achieve necessary signal-to-noise. For those observations, we derived the zeropoint from field stars chosen manually, but still using the PS1 catalog.

Images acquired using the 31-inch telescope did not contain a sufficient amount of stars for in-field calibration due to a brighter limiting magnitude. In these cases, we used Landolt standard star fields (Landolt, 1992, 2009) to determine the zeropoint and airmass extinction coefficient.

Because of our limited observing window, asteroid 2008 HE was observed in crowded star fields and suffered significant contamination. Difference image analysis (DIA; Bramich, 2008; Bramich et al., 2013) was used to extract useful data from such images. The technique

models the convolution kernel as a discrete pixel array, rather than a combination of linear functions. Each pixel value is solved for using a linear least squares. Using the kernel model, stars from a reference image can be blurred to match the seeing of each frame. After subtracting the blurred master from the image, the majority of the background stars are removed, allowing for more accurate photometry of the asteroid. This technique was only used for the images of 2008 HE because images of other asteroids are clean and the improvement form the usage of DIA is minimal.

2.2.5 Normalization

We estimated the absolute magnitude ($H(1,1,0)$ (or H), which is the apparent V-band magnitude at 1 au from the Sun and the Earth, observed at a phase angle of zero degrees. For observations made using SDSS filters, the g' magnitude value was converted to V magnitude (m_V) according to Jordi et al. (2006). To determine the absolute magnitude, we used the formula:

$$H(1,1,0) = m_V - 5\log_{10}(\Delta r_{\rm h}) + 2.5\log_{10}(\phi(\alpha)) \tag{2.1}$$

where Δ equals the geocentric distance in au, $r_{\rm h}$ equals the heliocentric distance in au, α is the phase angle (the Sun-Target-Observer angle) and $\phi(\alpha)$ is the phase integral, which is the ratio of the brightness at phase angle α to that at phase angle 0°. For the majority of the observed low-q asteroids, we used HG formalism (Bowell et al., 1989) with $G = 0.15$ to determine the phase integral. Asteroid 2002 AJ129 was the only object with enough phase coverage to determine the phase integral using the three-parameter magnitude phase

function (HG_1G_2; Muinonen et al., 2010), which we then used to determine a more accurate H (Section 2.3.5).

2.2.6 Reflectance Values

SDSS color filters provide sufficient wavelength coverage to study spectral slope trends (e.g., Thomas et al., 2013; Graves et al., 2018; Thomas et al., 2021). We followed techniques used by DeMeo & Carry (2013) and Thomas et al. (2013) to calculate the spectral slope over the g' , r' , and i' reflectance values (hereafter gri-slope) to represent the slope of the continuum and $z' - i'$ color representing the depth of the possible 1 μm band. First, known Sloan filter solar colors* ($g' - r' = 0.44$, $g' - i' = 0.55$, $g' - z' = 0.58$ mag) were removed from the color indices. Then, the Sun-subtracted color indices were converted into reflectance values, normalized to the g' band:

$$\frac{R_x}{R_g} = 10^{0.4[(m_g - m_x) - (m_{g,\odot} - m_{x,\odot})]} \tag{2.2}$$

The error for each reflectance point is calculated using standard error propagation. The R_g value does not have an error as the other values are always in relation to $R_g = 1$.

A linear regression was fit to the three photometric points using the central wavelength of the filters to calculate the slope. We computed the slope errors for each object via a Monte Carlo calculation, a technique used by Thomas et al. (2013, 2021). For each object, the individual reflectance values were modified by applying an offset of a random number pulled from a Gaussian distribution where the standard deviation is the 1-σ error of the

*http://classic.sdss.org/dr6/algorithms/sdssUBVRITransform.html

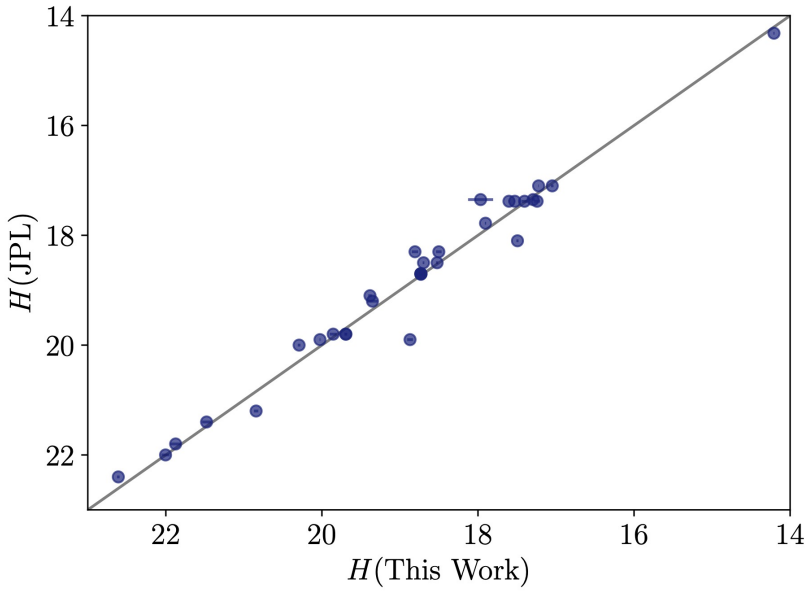

Figure 2.1: Absolute magnitude comparisons between this work and JPL. The solid line represents equality between the measurements. For all but one point, the errorbars are all within the marker. We find agreement between the values suggesting none of the objects were active during observations. All measurements including the largest difference between magnitudes of 1.02 (2008 MG1) are still within typical estimates for rotational variation.

reflectance value. This calculation was done 20,000 times for each object and a slope was determined for each altered spectrum. The uncertainty of the slope was the standard deviation of the altered slopes generated by this process.

2.3 Observational Results

2.3.1 Absolute Magnitude H

We find our derived absolute magnitude values to be mostly consistent with those reported by the Jet Propulsion Laboratory's (JPL) Small-Body Database[†] with a standard deviation of the difference equal to ∼0.3 (Figure 2.1). An offset in absolute magnitude

[†]`https://ssd.jpl.nasa.gov/`

larger than the uncertainty due to rotational variability ($A_{max} \lesssim 1$ mag for small asteroids; Statler et al., 2013) could indicate unresolved activity during one epoch. However, we do not observe any such offset and will explore upper limits of activity in Section 2.4.3.

2.3.2 Color Distribution

Our measured colors are summarized in Table 2.4 and plotted in Figure 2.2. For near-Sun asteroids, we see a wide variety of colors with large overlap between the near-Sun distribution and the colors reported by Dandy et al. (2003) and SDSS. Some objects have error bars spanning a broad spectrum, which we attribute to faint objects observed under less-than-ideal conditions after inspecting each frame individually to rule out uncertainty due to the occasional background star or poor photometric solutions. In Fig. 2.2, we also separate objects by Tisserand parameter T_J. Most main-belt asteroids have $T_J > 3$, most Jupiter-family comets (JFCs) have $2 < T_J < 3$, and long-period comets (LPCs) have $T_J < 2$. Therefore, T_J, which is related to an object's encounter velocity with Jupiter can generally be used to distinguish between types of orbits (Tisserand, 1896; Kresák, 1972; Carusi et al., 1987; Levison, 1996). The red circles have a cometary orbit ($T_J < 3$) and the blue squares have an asteroidal orbit ($T_J > 3$). We do not see a clear trend with color versus T_J. The two objects with the smallest spectral slope in the lower left of the figure are 2011 CP4 and 2019 UJ12. There are several objects with $r' - i'$ colors most similar to V-types, but some of their $g' - r'$ colors are more red.

We compared the distribution of colors of low-q objects to the range for NEAs using the Sloan Digital Sky Survey Moving Object Catalog (SDSS, MOC, Ivezić et al., 2001;

Table 2.4: Summary of Observations and Measured Magnitudes

Object	UT Date	Tel.[a]	r_h[b]	Δ[c]	α[d]	Filters	H_V[e]	g'	r'	i'	z'	$g'-r'$	$r'-i'$	$i'-z'$	gri-slope[f]
1995 CR	2017 Jan 25	INT	1.415	0.520	27.700	g', r', i'	21.87	22.826 ± 0.092	22.169 ± 0.084	21.928 ± 0.181	-	0.657 ± 0.124	0.242 ± 0.199	-	1.36 ± 1.02
2000 BD19	2017 Jan 26	INT	1.177	0.606	56.700	g', r', i', z'	17.53	19.260 ± 0.008	18.554 ± 0.003	18.551 ± 0.008	19.120 ± 0.034	0.706 ± 0.008	0.003 ± 0.008	-0.569 ± 0.035	0.59 ± 0.08
	2020 Jan 28	31in	1.103	0.272	57.788	B, V, R, I	17.60	-	17.071 ± 0.007	16.654 ± 0.007	16.494 ± 0.009	0.547 ± 0.023	-0.074 ± 0.016	-	-0.23 ± 0.11
	2020 Jan 30	31in	1.077	0.237	61.215	B, V, R, I	17.40	17.624 ± 0.057	16.621 ± 0.037	16.265 ± 0.035	16.317 ± 0.054	0.447 ± 0.092	-0.288 ± 0.070	-	-1.06 ± 0.26
	2020 Jan 31	31in	1.064	0.220	63.355	B, V, R, I	17.24	17.378 ± 0.043	16.337 ± 0.038	15.888 ± 0.033	16.119 ± 0.034	0.600 ± 0.090	-0.468 ± 0.053	-	-1.10 ± 0.23
2000 LK	2019 Jun 25	SOAR	2.421	1.839	22.766	g', r', i'	18.50	23.223 ± 0.051	22.555 ± 0.037	22.516 ± 0.065	-	0.668 ± 0.063	0.040 ± 0.075	-	0.58 ± 0.36
	2020 Mar 1	LDT	2.091	1.373	23.257	g', r', i', z'	18.81	22.548 ± 0.048	21.955 ± 0.052	22.073 ± 0.096	-	0.592 ± 0.071	-0.118 ± 0.109	-	-0.22 ± 0.40
2002 AJ129	2018 Feb 9	LDT	1.077	0.093	14.192	g', r', i', z'	18.73	14.785 ± 0.013	14.250 ± 0.009	14.203 ± 0.007	14.522 ± 0.009	0.535 ± 0.015	0.048 ± 0.011	-0.319 ± 0.012	0.12 ± 0.09
	2018 Feb 10	LDT	1.091	0.109	17.083	g', r', i', z'	18.73	15.245 ± 0.008	14.680 ± 0.007	14.658 ± 0.006	14.956 ± 0.008	0.565 ± 0.010	0.022 ± 0.009	-0.298 ± 0.010	0.14 ± 0.08
2002 PD43	2018 Jun 25	SOAR	1.239	0.836	54.575	g', r', i', z'	19.38	21.795 ± 0.029	21.211 ± 0.028	21.209 ± 0.040	-	0.583 ± 0.040	0.003 ± 0.049	-	0.14 ± 0.22
2004 UL	2019 Jun 25	SOAR	1.631	1.793	34.124	g', r', i', z'	18.73	22.727 ± 0.115	22.316 ± 0.077	22.277 ± 0.102	-	0.411 ± 0.139	0.039 ± 0.128	-	-0.31 ± 0.56
2006 HY51	2019 Mar 29	42in	2.585	2.643	22.387	B, V, R, I	17.05	19.133 ± 0.029	18.309 ± 0.016	17.871 ± 0.004	17.562 ± 0.047	0.581 ± 0.035	0.076 ± 0.052	-	0.38 ± 0.23
	2019 Mar 31	42in	1.470	0.660	34.530	g', r', i', z'	17.22	18.960 ± 0.004	18.326 ± 0.004	18.218 ± 0.005	18.578 ± 0.007	0.634 ± 0.006	0.109 ± 0.006	-0.360 ± 0.008	0.71 ± 0.08
2006 TC	2019 Oct 21	SOAR	1.446	0.878	42.540	g', r', i', z'	18.73	21.636 ± 0.143	20.902 ± 0.029	21.113 ± 0.056	-	0.523 ± 0.153	0.211 ± 0.064	-	0.66 ± 0.64
2007 EP88	2017 Apr 7	SOAR	1.571	0.664	23.890	g', r', i', z'	18.70	20.280 ± 0.017	19.654 ± 0.010	19.502 ± 0.009	20.115 ± 0.027	0.626 ± 0.019	0.152 ± 0.013	-0.613 ± 0.028	0.85 ± 0.12
	2020 Jan 2	SOAR	0.962	0.663	72.030	g', r', i', z'	18.52	20.442 ± 0.019	19.805 ± 0.016	19.643 ± 0.016	-	0.637 ± 0.025	0.162 ± 0.023	-	0.93 ± 0.16
2008 HE	2018 Mar 9	LDT	1.638	1.697	34.584	g', r', i', z'	17.49	21.465 ± 0.017	20.924 ± 0.017	20.928 ± 0.015	20.853 ± 0.026	0.541 ± 0.024	-0.004 ± 0.023	0.075 ± 0.030	-0.03 ± 0.13
2008 HW1	2017 Apr 7	SOAR	2.937	1.995	8.014	g', r', i', z'	17.97	22.705 ± 0.264	22.137 ± 0.105	21.878 ± 0.077	-	0.568 ± 0.284	0.259 ± 0.130	-	1.04 ± 1.31
	2017 Jan 24	INT	2.194	1.802	26.249	g', r', i', z'	17.29	21.845 ± 0.031	21.208 ± 0.014	21.142 ± 0.040	-	0.637 ± 0.034	0.066 ± 0.043	-	0.56 ± 0.22
2008 MG1	2017 Jul 1	SOAR	0.721	1.692	8.361	g', r', i', z'	18.87	20.218 ± 0.055	19.646 ± 0.035	19.576 ± 0.041	19.684 ± 0.094	0.572 ± 0.065	0.070 ± 0.054	-0.108 ± 0.103	0.33 ± 0.31
	2019 Jun 25	INT	1.371	0.373	15.476	g', r', i', z'	20.02	19.745 ± 0.009	19.197 ± 0.006	19.177 ± 0.014	19.260 ± 0.017	0.547 ± 0.010	0.020 ± 0.015	-0.083 ± 0.022	0.07 ± 0.09
2008 XM	2018 Jan 20	LDT	1.506	0.596	22.826	g', r', i', z'	20.29	21.476 ± 0.022	20.917 ± 0.002	20.629 ± 0.020	21.021 ± 0.065	0.558 ± 0.030	0.288 ± 0.029	-0.392 ± 0.068	1.11 ± 0.19
2010 JG87	2019 Aug 26	LDT	1.785	1.683	33.732	g', r', i', z'	19.35	23.520 ± 0.094	22.885 ± 0.062	22.890 ± 0.138	-	0.635 ± 0.113	-0.005 ± 0.152	-	0.30 ± 0.67
2011 CP4	2017 Jan 24	INT	1.701	0.727	7.423	g', r', i', z'	20.84	22.079 ± 0.042	21.684 ± 0.027	21.797 ± 0.078	-	0.395 ± 0.050	-0.113 ± 0.082	-	-0.77 ± 0.25
2011 KE	2018 Apr 14	LDT	1.755	0.800	14.953	g', r', i', z'	19.69	21.528 ± 0.020	21.085 ± 0.022	20.957 ± 0.028	21.444 ± 0.072	0.443 ± 0.029	0.128 ± 0.035	-0.487 ± 0.077	0.07 ± 0.16
	2018 Apr 15	LDT	1.768	0.820	15.624	g', r', i', z'	19.69	21.645 ± 0.021	21.157 ± 0.022	21.111 ± 0.030	21.512 ± 0.082	0.488 ± 0.031	0.046 ± 0.037	-0.400 ± 0.087	-0.04 ± 0.17
2013 YC	2017 Dec 17	LDT	1.431	0.447	0.856	g', r', i', z'	21.48	20.986 ± 0.051	20.416 ± 0.086	20.284 ± 0.072	20.544 ± 0.054	0.570 ± 0.100	0.131 ± 0.112	-0.260 ± 0.090	0.54 ± 0.56
2017 AF5	2017 Jan 24	INT	1.549	0.581	10.935	g', r', i', z'	17.90	18.685 ± 0.007	18.137 ± 0.012	18.102 ± 0.010	18.230 ± 0.029	0.547 ± 0.014	0.036 ± 0.016	-0.128 ± 0.030	0.12 ± 0.10
2018 GG5	2018 Apr 23	LDT	1.276	0.392	39.622	g', r', i', z'	19.86	20.232 ± 0.056	19.710 ± 0.055	19.578 ± 0.074	19.935 ± 0.135	0.523 ± 0.079	0.131 ± 0.092	-0.356 ± 0.154	0.36 ± 0.44
2019 AM13	2020 Mar 1	LDT	1.638	0.657	7.810	g', r', i', z'	22.00	23.037 ± 0.073	22.496 ± 0.054	22.334 ± 0.152	20.595 ± 0.079	0.540 ± 0.091	0.163 ± 0.161	-	0.54 ± 0.68
2019 UJ12	2019 Nov 4	LDT	1.145	0.192	34.023	g', r', i', z'	22.61	20.984 ± 0.012	20.572 ± 0.026	20.635 ± 0.123	-	0.412 ± 0.029	-0.063 ± 0.126	0.013 ± 0.166	-0.60 ± 0.35
Phaethon	2017 Jan 25	INT	2.154	2.307	25.206	g', r', i', z'	14.21	19.071 ± 0.011	18.703 ± 0.007	18.536 ± 0.010	18.617 ± 0.037	0.368 ± 0.013	0.167 ± 0.012	-0.081 ± 0.039	-0.06 ± 0.09
2004 LG[g]	2019 Mar 31	LDT	1.719	1.711	33.862	g', r', i'	17.67	21.754 ± 0.041	21.178 ± 0.039	21.355 ± 0.078	-	0.568 ± 0.058	-0.012 ± 0.100	-	-

[a] Telescope used: LDT = Lowell Discovery Telescope (4.3-m), 42in = Hall 42-in Telescope (1.1-m), 31in = 31-in Telescope (0.8-m), INT = Isaac Newton Telescope (2.5-m), SOAR = Southern Astrophysical Research Telescope (4.1-m)
[b] Heliocentric distance, au
[c] Geocentric distance, au
[d] Phase angle, degree
[e] Absolute V magnitude measured by this work
[f] The slope of the reflectance values over g', r', and i' bandpasses [$\%/\mu m$]
[g] 2004 LG was formerly low-q (Vokrouhlický & Nesvorný, 2012)

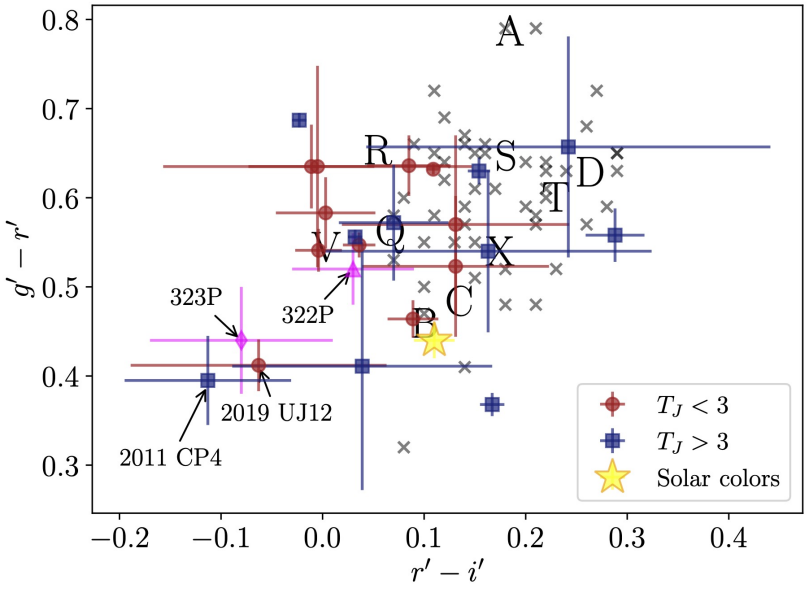

Figure 2.2: Color-color diagram of low-q asteroids. The grey 'x's are the color values of NEAs from the SDSS Moving Object Catalog (Ivezić et al., 2001; Ivezic et al., 2002). The large capital letters represent the average colors of taxonomic classes of NEAs from Dandy et al. (2003). The color of comet 322P from Knight et al. (2016) is shown as a magenta triangle. The first reported color of 323P from Hui et al. (2022) is shown as the magenta diamond. The red circles and blue squares are low-q asteroids with T_J less than and greater than 3, respectively.

Ivezic et al., 2002), which observed 471,569 moving objects through March 2007, using five filters, u', g', r', i', and z'. We restricted the sample from the SDSS MOC database according to the criteria outlined in DeMeo & Carry (2013) Section 2.1, which includes filtering faint data, data with large errors, and data with flags relevant to moving objects and good photometry. We further reduce the sample by only including objects that are categorized as NEAs ($q \leq 1.3$ au). Applying the selection criteria, we are left with a sample of 42. We plot the range of colors as a gray 'x's behind our low-q measurements and the average colors of NEA types observed by Dandy et al. (2003) to give context for our findings. We also included the colors of 322P/SOHO 1 (Knight et al., 2016), 323P/SOHO (Hui et al., 2022), and solar colors.

In the color-color plot (Figure 2.2), we observe that low-q asteroids have a bluer distribution compared to average NEA colors (more in the lower left than the upper right). To investigate this further, we used a kernel density estimation (KDE) plot of the colors (Figure 2.6). Rather than using discrete bins, a KDE plot smooths the measurements with a Gaussian kernel, producing a continuous probability density estimate. The data points are weighted by their 1-σ uncertainty and the kernel bandwidth is selected according to Scott's Rule (Scott, 1992). The result is shown in Fig. 2.6. The low-q $g' - r'$ colors appear to have the same distribution as the colors from SDSS MOC, but shifted bluer. The low-q $r' - i'$ colors show a wider distribution than the SDSS MOC, but they extend to bluer colors. The KDE plots confirm our interpretation of the color-color plot.

The reflectance values for each observation can be seen in Figure 2.3. We use the reflectance values to determine the gri-slope and $z' - i'$ color, representing the slope of the continuum and the 1-μm band depth, respectively. Both of these parameters are affected by space weathering, which causes a steeper spectral slope and a shallower 1-μm band depth. We compare our sample to NEAs from SDSS MOC values and class boundaries reported by DeMeo & Carry (2013) (Figure 2.4). We find near-Sun asteroids have a shallower spectral slope compared to the NEA population, especially those with V-type colors, which agrees with our findings of bluer colors shown in Figure 2.2. The $z' - i'$ reflectance values are smaller as well, consistent with a steeper 1-μm band depth.

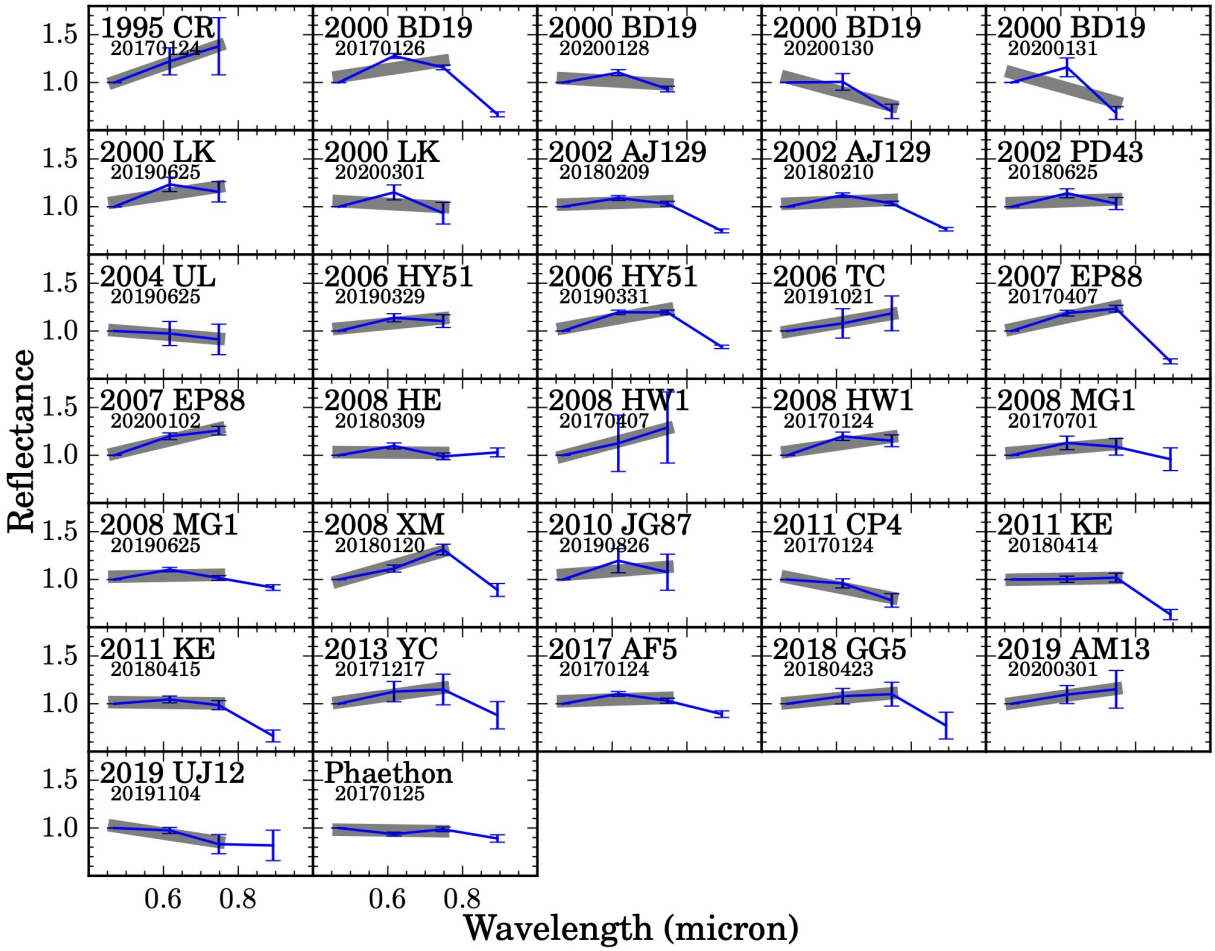

Figure 2.3: Spectrophotometry of low-q asteroid observations created by transforming colors into reflectance values. Our measurements are in blue at their central wavelength, normalized to the g' filter, with uncertainties shown. The grey bar shows the measured gri-slope. The object's name and UT date of observation (YYYYMMDD) are given on each panel.

2.3.3 Spectral Slope Trends with Decreasing Perihelion

We compare the low-q spectral slopes with the trend versus perihelion distance seen in S- and Q-type NEAs with $q \geq 0.2$ au by Marchi et al. (2006b) and Graves et al. (2019) to determine if the same trend might extend to smaller perihelion distances (Figure 2.5). We can make this comparison because we anticipate our sample to be predominately S- or Q-type because together they are the most common NEA types Binzel et al. (2019) and

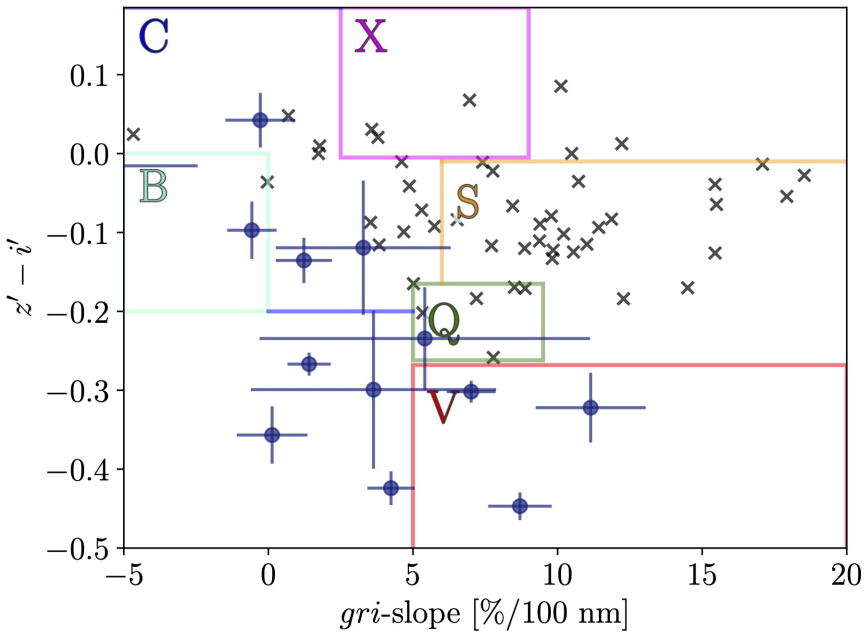

Figure 2.4: *gri*-slope and $z' - i'$ reflectance values of low-q asteroids (blue dots). For comparison we show the distribution of NEAs from the SDSS MOC4 catalog (gray 'x's) and boundaries used to classify SDSS data from DeMeo & Carry (2013). Low-q asteroids have a flatter spectral slope than the NEA population.

based on dynamical modeling of source regions, which we discuss in Section 2.3.6. For our comparison, we used the trend measured by Graves et al. (2019) who implemented a windowed moving average, instead of the similar trend determined by Marchi et al. (2006a), who implemented a point-based moving average. Our data are consistent with the extended trend at the 1-σ level. However, given the large uncertainty in some of the slopes in our dataset and the short range of q, the trend is virtually indistinguishable from a flat distribution, indicative of no spectral slope change with perihelion distance. Further investigation is warranted.

2.3.4 Lightcurves

We compiled high-cadence lightcurves of three bright objects (394130 (2006 HY51), 276033 (2002 AJ129) and 137924 (2000 BD19)) in our sample in order to measure their rotation periods and amplitudes. The methodology for determining the rotational period follows our approach in earlier papers (e.g., Knight et al., 2011, 2012; Eisner et al., 2017). Because observing geometry changed rapidly throughout the night, we corrected our photometric results for the geometric circumstances image by image. The rotation period was estimated by superimposing the lightcurves from all nights, with the data phased to a "trial" period and zero phase at perihelion. We then iterated the trial period, making direct "better or worse" comparisons between each iteration, until a rotation period estimation

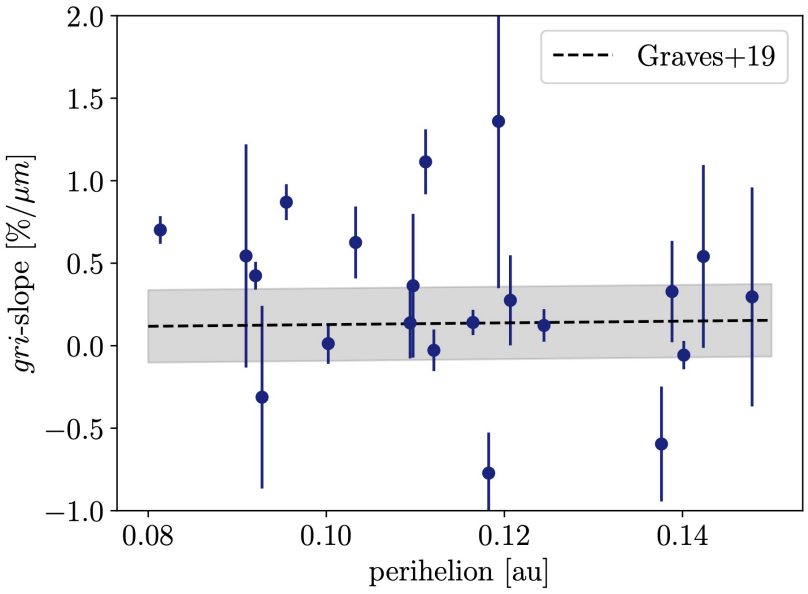

Figure 2.5: The distribution of *gri*-slope vs. perihelion distance of low-q asteroids. The dashed line and the shaded region show the trend for S- and Q-type NEAs using data in Binzel et al. (2004); Lazzarin et al. (2004, 2005) and the uncertainty at a 95% confidence level according to Graves et al. (2019). Our data are consistent with Graves et al. (2019) at the 1-σ level.

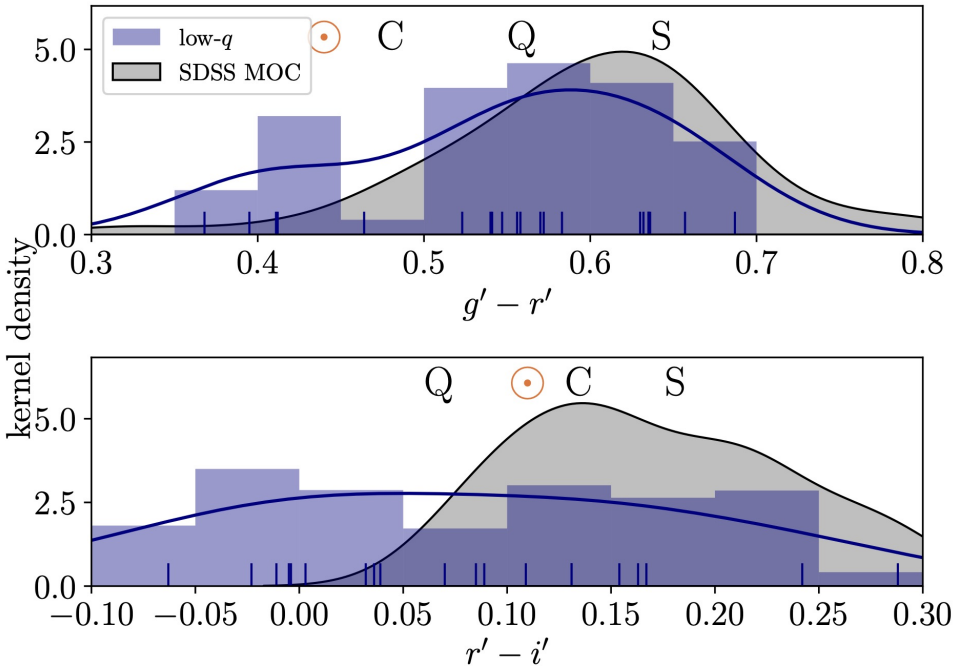

Figure 2.6: Kernel density plot of low-q asteroid colors with underlying histogram (blue), where data points are weighted by their 1-σ uncertainty and the kernel bandwidth is selected according to Scott's Rule (Scott, 1992). This allows us to assess the color distribution as a smooth probability density, instead of only discrete bins in the histogram. The black filled in curve is the color distribution of NEAs from SDSS MOC. The colors of the most common asteroid types according to Dandy et al. (2003) are shown as letters, as well as Solar colors shown as an orange "⊙". We find a preference towards bluer colors for both $g' - r'$ (top) and $r' - i'$ (bottom).

was constrained by eye. We estimate the uncertainty by determining how much the period can be adjusted before a phased light curve appears obviously incorrect.

2.3.4.1 2006 HY51

2006 HY51, whose rotation period was previously unconstrained, was observed over three nights (March 27-29, 2019) using Lowell Observatory's 42-inch telescope and the Johnson R filter. We collected $\sim$ 6 hours of data each night with frames every $\sim$ 300 seconds. We measured a rotation period of 3.350 ± 0.008 hours and a maximum peak-to-

trough amplitude of ∼0.2 mag (Fig. 2.7). The lightcurve has an interesting shape, with one peak larger than the other, suggesting the shape of the asteroid deviates substantially from a tri-axial ellipsoid (Magnusson, 1986).

2.3.4.2 2002 AJ129

2002 AJ129 was observed over two nights (February 6-7, 2018) using Lowell Observatory's 31-inch telescope in robotic mode and the Johnson R filter, collecting $\sim$ 9 hours of data each night with frames every $\sim$ 90 seconds. We found a rotational period of 3.918 ± 0.010 hours and a peak-to-trough amplitude of ∼0.15 mag (Figure 2.8). The prepublished period of 2002 AJ129 was reported by the Ondrejov Asteroid Photometry Project (Pravec et al., 2018)[‡] as 3.9226 ± 0.0007 hrs, and Devyatkin et al. (2022) reported a period of 3.9222 ± 0.0008 hrs. Both measurements are within our uncertainty.

2.3.4.3 2000 BD19

We observed 2000 BD19 over two half-nights (January 30–31, 2021) using Lowell Observatory's 31-inch in robotic mode and the Johnson R filter, collecting $\sim$ 6 hours of data each night with frames every $\sim$ 20 minutes. Warner (2015b) observed 2000 BD19 over six nights and report a rotational period of 10.570 ± 0.005 hours and a max peak-to-trough amplitude of 0.69 ± 0.04. Without full coverage, we are unable to constrain the rotational period further. However, when phased to the published period, our results are consistent with the reported period and amplitude (Figure 2.9).

[‡] `http://www.asu.cas.cz/~ppravec/newres.htm`

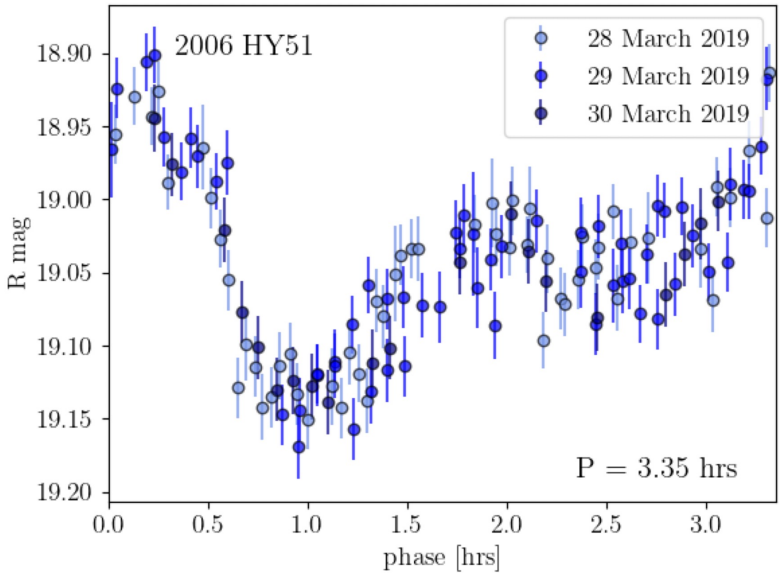

Figure 2.7: Rotational lightcurve of 2006 HY51 using data from March 2019 using Lowell Observatory's 42-inch telescope. The lightcurve is phased to the best-fit period of 3.350 ± 0.008 hours.

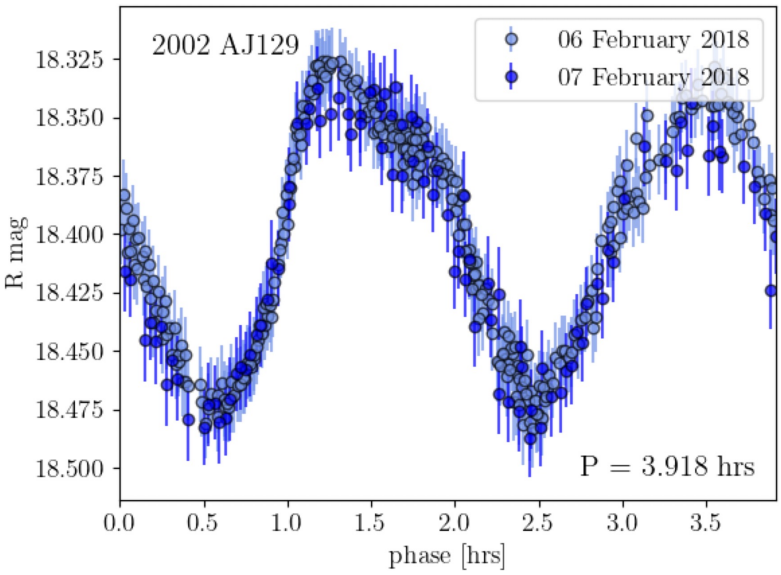

Figure 2.8: Rotational lightcurve of 2002 AJ129 using data from February 2018 using Lowell Observatory's 31-inch telescope. The lightcurve is phased to the best-fit period of 3.918 hours.

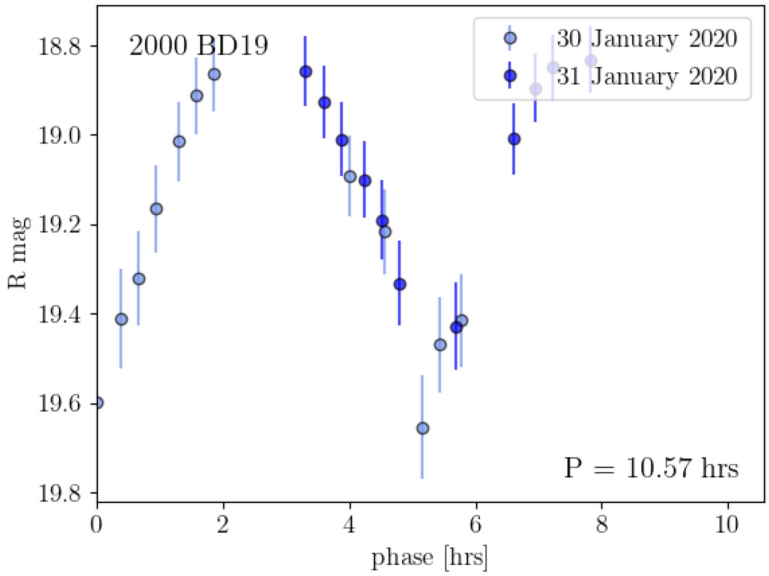

Figure 2.9: Rotational lightcurve of 2000 BD19 using data from January 2020 using Lowell Observatory's 31-inch telescope. The lightcurve is phased to the best-fit period of 10.57 hours determined by Warner (2015b). We were unable to constrain the rotational period further.

2.3.5 Phase Coefficient

For most of the objects we observed, the range of phase angles was too small to determine the asteroid's phase function. The exception is asteroid 2002 AJ129, which we observed over two nights with Lowell Observatory's 31-inch over $\sim 0.8 - 17.8$ degrees. Using the online implementation of the model selection stated in Penttilä et al. (2016), we employ the H, G_1, G_2 system described in Muinonen et al. (2010). G_1 and G_2 are determined to be 0.157 ± 0.035 and 0.486 ± 0.017, respectively, which is consistent with measurements of main-belt asteroids (Muinonen et al., 2010; Vereš et al., 2015).

2.3.6 Source Region Probabilities

We assessed the origin of low-q asteroids using the Granvik & Brown (2018) escape region model, which has been progressively developed by Granvik et al. (2016, 2017, 2018). Given the orbital elements and H magnitude of an object, this model gives the probabilities that an object "escaped" from each of the seven source regions, where the sum of the probabilities is equal to one. The source regions consist of the ν_6 inner main-belt region, Jupiter resonance complexes: 3:1, 5:2 and 2:1, the Hungarias, the Phocaeas, and the Jupiter-family comets. Source regions and orbital elements are tabulated for all 53 known low-q objects in Table 2.2 and the source region with the highest probability of being the escape region for each object is in bold. All known objects with $q \leq 0.15$ au most probably escaped from ν_6 or 3:1 regions with the exception of 2010 JG87, which most likely escaped from the 5:2 region.

This is unsurprising considering the ν_6 region and the 3:1 are the resonance escape regions for nearly 80 percent of NEAs (Bottke et al., 2002; Granvik et al., 2018; Binzel et al., 2019). NEAs from these source regions are mostly S- or Q- type, with $\sim 80-90$ percent having a geometric albedo greater than 0.1 (Binzel et al., 2019; Morbidelli et al., 2020). These resonances call for large oscillations of the eccentricity, so even if asteroids from these regions are not currently low-q, they possibly were at one point in their dynamical history. Around 80 percent of all NEAs have experienced a perihelion distance smaller than 0.15 au at some point since they escaped from the main belt (Toliou et al., 2021). For our specific sample, we use the lookup table from Toliou et al. (2021), which utilizes the NEO model from Granvik et al. (2018) to determine the probability an object with a given set

of orbital elements and H magnitude spent time with a perihelion distance smaller than a certain q_s and the estimated dwell times with $q \leq q_s$. Unlike previous models, the Granvik et al. (2018) model accounts for "supercatastrophic" disruption of NEAs within a certain q, dependent on H. We tabulate the estimated dwell times each of our objects spent with $q \leq 0.15$ au in Table 2.2. Dwell times range from one kyr (2013 YC) to 15 Myrs (2007 EP88), consistent with the findings from Marchi et al. (2009). The time spent with $q \leq 0.15$ au can vary from several hundred years to a few Myr, averaging $\sim$ 20 kyr for NEAs from ν_6 (Toliou et al., 2021). Asteroids escaped from the 3:1 resonance and outer main-belt spend an average of $\sim$ 5 kyr and $\sim$ 300 yrs with $q \leq 0.15$ au (Marchi et al., 2009).

2.4 Discussion

2.4.1 Near-Sun Processes

Space weathering is the alteration of asteroid surfaces due to the space environment, which is dominated by ion radiation from the solar wind (Marchi et al., 2006b; Vernazza et al., 2009; Brunetto et al., 2015), as opposed to micrometeorite impacts, which have longer timescales (Sasaki et al., 2001). How space weathering affects an object is dependent on the object's original composition (Lantz et al., 2017). Because characterized low-q objects typically have high albedos, where more than ten percent of incident radiation is reflected (Mainzer et al., 2012; Granvik et al., 2016), we focus on the space weathering effects on high-albedo objects. The space weathering effects on silicates are well understood, where nanophase reduced iron particles (npFe0) darken and spectrally redden the surface (e.g., Pieters et al., 2000; Taylor et al., 2001; Hapke, 2001; Clark et al., 2002; Brunetto et al.,

2015). Space weathering of silicates will also suppress the pyroxene-olivine absorption bands (e.g., Pieters et al., 2000; Hapke, 2001; Gaffey, 2010). Therefore, when a fresh unweathered surface is exposed by some resurfacing process, the spectral slope becomes bluer for asteroids with a higher albedo. This has been observed on NEA Eros by NEAR (Clark et al., 2001) and on regolith grains brought from NEA Itokawa during the Hayabusa mission (Noguchi et al., 2011), both of which are S-type asteroids.

There are several potential resurfacing mechanisms that affect asteroids when they closely approach the Sun. (a) Increasing temperatures can cause material from lower surface layers to sublimate and allow for progressively less volatile material to reach sublimation temperatures. Decomposition and sublimation of refractory organics begins around ∼450 K, metal sulfides at ∼700 K, and silicates at 1000–1500 K (see review by Jones et al., 2017). (b) Many studies have explored resurfacing caused by the tidal forces experienced during planetary encounters (e.g., Nesvorný et al., 2005; Marchi et al., 2006b; Binzel et al., 2010; Nesvorný et al., 2010; DeMeo et al., 2014; Carry et al., 2016; Devogèle et al., 2019). (c) An asteroid with an irregular surface can experience an increase in spin rate due to asymmetrical radiative torques, known as the Yarkovsky-O'Keefe-Radzievskii-Paddack (YORP) effect (Bottke et al., 2006), which may result in centrifugal loss of material (Rubincam, 2000; Vokrouhlický et al., 2015). (d) Thermal fatigue induced by the diurnal temperature variations can cause boulders and grains to fracture and break down into smaller regolith, which can then be lost due to outgassing and/or solar radiation pressure (Jewitt, 2012; Delbo et al., 2014). Such thermal cracking was observed on asteroid Bennu during the OSIRIS-REx mission (Molaro et al., 2020). (e) Resurfacing through impacts by high-speed near-Sun meteoroids that could eventually lead to disruption has also been

suggested (Wiegert et al., 2020). All of these processes can resurface weathered regolith on low-q asteroids, which would most likely cause an overall bluer spectrum.

2.4.2 Colors

We found evidence for bluer colors in the low-q population when compared to NEAs (Dandy et al., 2003), but it is not as obvious as we might expect given the bluer colors observed in comets 322P, 323P, and 96P (Knight et al., 2016; Eisner et al., 2019). Additionally, we find agreement with the extended bluening trend with decreasing perihelion seen in S- and Q-type NEAs at $q > 0.2$ au (Marchi et al., 2006a; Graves et al., 2019). However, uncertainties are such that over the short range of q, the trend is indistinguishable from no spectral slope change with q.

The color distribution of low-q asteroids may be more stochastic because of competing processes and the potential variety in asteroid properties, including dynamical properties and regolith properties, such as albedo and grain size, which play a role in the extent of heating and near-Sun processing effects. Phase reddening, where the spectral slope increases with increasing solar phase angle, α, is expected to contribute to the scatter in the distribution; the effect is common among S-group asteroids (Sanchez et al., 2012; Carvano & Davalos, 2015; Perna et al., 2018), but the extent varies for each individual asteroid and therefore cannot be modeled out of our measurements (Carvano & Davalos, 2015; Binzel et al., 2019; Popescu et al., 2019).

2.4.2.1 Dynamical Considerations

Near-Sun processes are generally influenced by the surface temperature and the length of time spent at that temperature. Therefore, understanding the dynamical history of low-q objects is important for interpreting our results. While dynamical modeling can give a general idea, we cannot know for certain the dynamical history of any individual object. Some objects could have recently migrated to a low-q orbit in the last couple hundred years, while others could have been in a stable low-q orbit for several thousand years and some objects might have had low-q in the past and have migrated back for the n-th time through resonance oscillations (i.e., Lidov-Kozai oscillations: Lidov, 1962; Kozai, 1962). There is likely a broad range of dynamical histories for our sample. However, we can use dynamical modeling to better understand the temperatures experienced or the duration of heating throughout an individual asteroid's lifetime.

Roughly half of the known near-Sun asteroid population have $T_J < 3$, which indicates a cometary orbit. If such asteroids are actually dormant comets, we might expect their colors to be distinct due to compositional differences or surface changes due to sublimation of volatiles (Jewitt, 2015). The percentage of NEAs that are dormant comets is estimated to be anywhere from 3 – 20 percent (e.g., Fernández et al., 2005; Bottke et al., 2002; DeMeo & Binzel, 2008; Mommert et al., 2015). We see no evidence for color difference based on Tisserand parameter with respect to Jupiter. We find the average colors for objects with asteroidal orbits to be $g' - r' = 0.54 \pm 0.11$ and $r' - i' = 0.10 \pm 0.12$ and cometary orbits to be $g' - r' = 0.56 \pm 0.07$ and $r' - i' = 0.05 \pm 0.06$. However, we find that the colors are significantly bluer than cometary nuclei ($g' - r' = 0.68 \pm 0.06$ and $r' - i' = 0.23 \pm 0.04$;

Jewitt 2015). Because dormant comets make up $\sim 10\%$ of the NEA population, a larger sample size is needed to investigate such a connection.

Low-q asteroids 2019 UJ12 and 2011 CP4 have the bluest colors in our sample. The Toliou et al. (2021) model shows an average dwell time of 200 yrs for the orbital properties of 2019 UJ12, suggesting it is likely experiencing near-Sun resurfacing processes, such as thermal fatigue, for the first time. However, 2019 UJ12 has a poorly constrained orbit (U = 8), so we consider this result inconclusive. Other than 2019 UJ12, we observe no clear trend between dwell times and color. Although, it is important to note that the Toliou et al. (2021) model uses an integration over the entire dynamical lifetime of an object. To compliment the Toliou et al. (2021) model, we conducted backward-integration of the orbits of individual low-q objects over the last 2000 yrs using the methods described in Hsieh et al. (2021) and found that 2011 CP4 has had several close encounters with Earth in the past 2000 yrs, which suggests its very blue color may be due to resurfacing caused by tidal encounters. However, space weathering occurs on timescales of $\sim 10^4 - 10^6$ yrs, so potential resurfacing events occurring more than 2000 yrs ago must be considered, but such integrations are beyond the scope of this project.

Formerly low-q asteroid 2004 LG, which spent 2500 years with $q < 0.076$ au (Vokrouhlický & Nesvorný, 2012; Wiegert et al., 2020) does not exhibit any unusual colors compared to the near-Sun population and other NEAs, though we would suspect otherwise after being in an extreme environment, within the catastrophic disruption limit determined by Granvik et al. (2016). 2004 LG may not be an S- or Q-type and therefore, experiences near-Sun properties differently. There is also the possibility that surface variability over time may play a role, which will be discussed below.

2.4.2.2 Varying Surface Properties

Albedo, emissivity, macroscopic surface roughness, and thermal inertia all affect surface temperature. Surface roughness alone can raise the average surface temperature by 20–30% (Marchi et al., 2009). Albedo affects the degree of space weathering and the amount of radiation absorbed vs. reflected. And thermal inertia governs the temperature distribution on an asteroid's surface. These surface properties, as well as rotational properties, influence the degree of thermal fatigue, which is thought to be the dominant regolith production process and resurfacing mechanism for near-Sun asteroids (Delbo et al., 2014; Graves et al., 2019) and involves the formation and expansion of cracks as a result of diurnal temperature variation. These properties vary with composition, but can also vary between objects of the same taxonomy. Because most of our objects have few observations, these properties are essentially unknown but are expected to vary between objects, contributing to the observed scatter in the color measurements.

There are more low-q asteroids with colors similar to V-types than expected given that V-types make up only ∼5% of the NEA population (Binzel et al., 2019). This could simply be small number statistics. However, V-type asteroids have high albedos (∼0.3; Usui et al. 2013), so the overabundance could be due to an observation bias. Alternatively, as proposed by Granvik et al. (2016), higher albedo objects are less likely to experience enough thermal cracking or sublimation to disrupt at low-q because they absorb less heat than lower albedo objects. Thus, there may be a survivorship bias that favors V-type asteroids. Another possibility is that Yarkovsky drift may create a slower orbital progression timescale for higher albedo objects. If so, a longer residence lifetime in near-Sun orbits could create a

bias toward these objects being noticed in a survey. However, Granvik et al. (2018) found Yarkovsky drift on the NEO steady state orbit distribution to be negligible compared to the gravitational perturbations caused by planetary encounters. Thus, such an effect may be difficult to detect.

2.4.2.3 Competing Processes

Competing processes are likely contributing to the wide color distribution we measured compared to the NEA population as shown in the $r' - i'$ KDE plot in Fig. 2.6. The space weathering rate increases by two orders of magnitude from 1 to 0.1 au because solar irradiation increases as $r_{\rm h}$ decreases (Marchi et al., 2006b; Paolicchi et al., 2007). Similarly, several resurfacing processes are expected to increase at low-q. The effects from Yarkovsky and YORP are expected to increase with solar irradiation as well. As surface temperature increases, the diurnal temperature variation increases, allowing for more resurfacing due to thermal fatigue. Space weathering caused by solar irradiation has a timescale of $\sim$ 10 kyr – 1 Myr (Hapke, 2001; Brunetto & Strazzulla, 2005; Strazzulla et al., 2005; Brunetto et al., 2006; Loeffler et al., 2009; Vernazza et al., 2009). The timescale of thermal degradation is thought to decrease with decreasing heliocentric distance as $r_{\rm h}^k$ where $k > 5$ and the timescale for space weathering should be less than half the timescale of thermal degradation to explain the decreasing spectral slope with decreasing perihelion distance trend (Graves et al., 2019). However, those timescales were estimated based on S- and Q-type NEAs with $q > 0.2$ au; those relations might not be valid at $q \leq 0.15$ au. Additionally, multiple resurfacing processes can be occurring on the same object at the same time, which

can further counter space weathering.

It is possible that the wide variety of colors we measured in the low-q population is related to the consistent battling of processes. The refreshed surface continues to be irradiated by the Sun as it is undergoing resurfacing processes. As time in low-q orbit passes, there is less and less "fresh" surface to expose. In other words, the resurfaced regolith has already been irradiated. Binzel et al. (2019) suggest that after enough time, the asteroid surface may be "saturated" by space weathering and will have maximum redness, while objects new to low-q might have the most refreshed surface. The result would be a larger variance in colors with decreasing distance to the Sun. Comparing the low-q sample with more distant NEAs, we find that the variance in $r' - i'$ color (0.010) is higher for our low-q sample compared to the SDSS MOC NEA population (0.004), but the variance in $g' - r'$ color is the same for both (0.008). This theory could also explain the bluer colors of 2019 UJ12, as well as the redder color of 2007 EP88, which has spent the most time with $q \leq 0.15$ au.

2.4.3 Activity

This study focused on observing surface properties since the goal was to sample the whole population in ~ 3 years. As a result, most were too faint to meaningfully search for comae. We visually inspected all data and did not detect any evidence of activity, e.g., tail, coma, or broadened PSF. Comparing absolute magnitudes at the time of observation to previous data, we can crudely constrain that the low-q asteroids had no activity in excess of typical NEA rotational amplitudes.

Since all objects in our sample reach perihelion within SOHO's FOV, they are observable every orbit when they are most likely to be active. SOHO's limiting magnitude of ∼8 is not sensitive enough to detect any objects in our sample unless they are active. However, because forward-scattering of comet dust grains is highly efficient (e.g., Marcus, 2007a; Hui, 2013), for some orientations only a small amount of coma is needed in order to be detected. We constructed a simple model to estimate the observability of the low-q asteroids when in the SOHO FOV ($r_{\rm h} \leq 0.15$ au). Using the limiting magnitude of SOHO, we can determine the dust cross-section needed to be detectable:

$$C = \frac{(2.25 \times 10^{22})\pi r_{\rm h}^2 \Delta^2}{p_r \phi(\alpha)} 10^{0.4(m_\odot - m_{lim})} \tag{2.3}$$

where p_r is the r'-band geometric albedo, α is the phase angle (the Sun-target-observer angle), $\phi(\alpha)$ is the phase function (we use the Schleicher-Marcus comet dust phase function; Schleicher & Bair, 2011), $m_\odot$ is the apparent r'-band magnitude of the Sun, and m_{lim} is the limiting magnitude of SOHO (∼8). We identified all instances when each asteroid in our sample was within the SOHO FOV. We then estimated the depth of global material lost in order for the object to be detectable by SOHO, assuming an average particle size of 1 μm, a density of 3000 kg/m^3, an albedo of 0.15, and the diameter estimate for each object. The minimum depth was ∼0.2 μm, though most required more than 1 μm, the approximate depth of material needed to be excavated by Phaethon to produce the amount of dust observed while Phaethon was active near perihelion (Li & Jewitt, 2013). The apparitions needing the least depth of material were either Phaethon, the largest low-q object in our sample, or objects in extreme forward-scattering geometries ($\alpha > 160°$).

Phaethon has been repeatedly detected in STEREO images at peak apparent magnitude of ∼11 (Hui & Li, 2017). As this is about ∼3 mag fainter than SOHO's limiting magnitude, it is no wonder that it has never been detected in SOHO images. Thus, it seems likely that our simple model is overly optimistic. There are numerous uncertainties in our estimates, including assuming spherical grains, uniform grain size, grain albedo, and that asteroid grains scatter in a manner analogous to comet grains, which might affect the estimated depth by an order of magnitude. Furthermore, we assumed that such dust would be present throughout the time the asteroid was in SOHO's field of view, but Li & Jewitt (2013) showed that Phaethon's activity only lasts for a few days with peak activity ∼0.5 days after perihelion, greatly reducing the window for such dust to be detected on a given apparition. Thus, we can only exclude activity in the rest of the low-q population at 1–3 orders of magnitude higher mass-loss rates per unit surface area than Phaethon since they are significantly smaller. A deeper search of the SOHO data via shifting and stacking at the ephemeris rate (e.g., Hui & Knight, 2019) could set upper limits for activity near perihelion for each object in the sample, but is beyond the scope of this thesis.

2.4.4 Rotation Periods

Only nine low-q objects have reported rotational periods, including 2006 HY51 first reported in this work (Table 2.1; Figure 2.10). While several low-q objects have rotation periods ∼3–4 hours, only one object (2011 XA3) has a rotation period of ∼45 minutes, which is below the critical spin limit for a rubble pile asteroid (Urakawa et al., 2014). 2011 XA3 has $H = 20.4$, corresponding to a diameter ∼200 – 500 meters, depending on

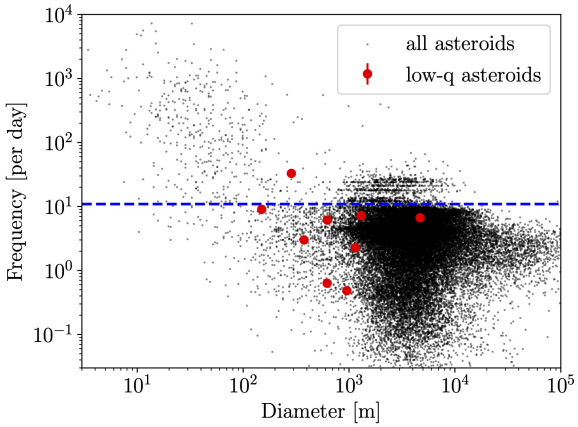

Figure 2.10: The distribution of rotational periods vs. diameter of low-q asteroids (red) compared to the general asteroid population from the JPL Small-Body Database (black). The critical spin limit of 2.2 hours can be seen for asteroids with diameters greater than 200 meters.

albedo. Because fast-rotating asteroids must resist their own centrifugal force, they have structurally significant tensile strength.

Both 322P and 96P are among the fastest-rotating known comets being at/near the spin period limit, with periods of ∼3 and ∼4 hours, respectively (Knight et al., 2016; Eisner et al., 2019). 323P is the fastest rotating comet with a period of ∼0.5 hrs, which is a suggested driver of the comet's activity (Hui et al., 2022). The fast spin-rates could be indicative of increased YORP effect near the Sun. A larger sample in the future could support this idea if more low-q objects were found to be fast-rotating.

Smaller asteroids are found to have bluer colors (Binzel et al., 2004; Thomas et al., 2012; Carry et al., 2016), likely due to resurfacing caused by YORP spin-up and failure (Graves et al., 2018). Therefore, we might assume faster-spinning objects approaching or above the spin barrier have bluer colors. On the other hand, a faster-spinning asteroid has a more smoothed-out temperature distribution in longitude than a slower rotating one, creating less diurnal variability and lessening the effects of resurfacing due to thermal

fatigue. We search for a trend of colors versus rotational period. However, the sample is very limited (nine objects) and no definitive trend could be observed.

2.4.5 Future Surveys

The upcoming Vera Rubin Observatory's Legacy Survey of Space and Time (LSST) will increase the number of known NEOs by an order of magnitude. NEOs will be observed a median of 90 times spread among *ugrizy* bandpasses (Jones et al., 2016). A similar analysis to this work with a much larger sample size will likely be possible. However, if different filters are not obtained simultaneously, colors might not be easily measured due to geometric and rotational variation between observations. Because there will be hours to days between observations of the same object, rotational periods are unlikely to be determined without dedicated prompt follow-up of LSST discoveries, unless the period is sufficiently long. LSST will observe NEOs at several epochs with various phase angles so a phase curve is likely to be obtained. Determining the phase curve for low-q objects will give us a better understanding of surface roughness, which can better constrain the models of regolith production and resurfacing due to thermal fatigue. LSST will be capable of monitoring and reporting any activity or disruption events nightly with potential pipelines and proposed surveys (Schwamb et al., 2018; Seaman et al., 2018), which will further the study of near-Sun asteroids that are more likely to be active or catastrophically disrupted (Jewitt, 2012; Granvik et al., 2016; Ye & Granvik, 2019).

The Near-Earth Object Surveillance Mission (NEOSM, previously NEOCam; Sonnett et al., 2020) aims to extend the Wide-field Infrared Survey Explorer (WISE) catalog

of diameters and visual albedos by an order of magnitude. NEOSM is expected to point closer to the Sun than NEOWISE or Spitzer, enabling the search for near-Sun activity as well as the discovery and albedo measurements of more low-q objects. More albedo measurements of low-q asteroids will help us determine the surface temperature these objects reach as well as how space weathering affects the surface, which varies with composition and can be distinguished with albedo (Lantz et al., 2017). Additionally, the combination of NEOSM with increasing cadence of visible observations like LSST (and other surveys like PANSTARRS, ZTF) should improve the size estimates.

2.5 Conclusions

We obtained magnitude and optical color measurements of 22 near-Sun asteroids with $q \leq 0.15$ au over three years from January 2017 to March 2020 primarily using various 4-m class telescopes. We obtained lightcurve data for three low-q asteroids, finding results consistent with previously published values for two and determining a rotation period for 2006 HY51 equal to 3.350 ± 0.008 hr. We provide a summary of all known properties of near-Sun asteroids including albedos, rotational periods, and spectra. These objects were studied in order to search for trends relating to surface modification due to near-Sun processes, particularly those that might lead to disruption. We find that the observed low-q asteroids exhibit bluer colors overall, though overlapping with the color distributions of NEAs. However, there are no clear trends of colors with perihelion distance, Tisserand parameter, or rotational period. Unknown dynamical histories and compositions for individual objects combined with competing surface-altering processes are likely responsible for the stochastic

color distribution. Finally, future surveys will enable studies of near-Sun objects with a much larger sample.

Chapter 3: Long-term Monitoring of Distant Oort Cloud Comets

3.1 Background

Thanks to powerful sky surveys, comets today are routinely discovered with heliocentric distances (r_h) greater than 5 au, and discoveries of comets with $r_h > 10$ au are increasing (Figure 3.1). These objects have a visible coma, so we know they are active in some manner. However, the drivers of said activity are not well understood. H_2O is the most abundant volatile and the main driver of cometary activity within ∼3 au, but water-ice sublimation is inefficient beyond ∼5 au (Meech & Svoren, 2004). Distant activity is likely driven by more volatile ices like CO and CO_2, which are next in abundance and can lift grains out to heliocentric distances of 6–8 au for CO_2 and tens of au for CO (Meech & Svoren, 2004; Jewitt et al., 2021). The one-time transition from amorphous to crystalline water-ice has also been suggested to drive activity from ∼3 up to 10 au from the Sun (e.g., Smoluchowski, 1981; Jenniskens & Blake, 1996).

As discussed in Section 1.4, there is evidence of differing brightening rates between new and returning comets. However, the majority of inbound observations were conducted within 3 au from the Sun (e.g., Whipple, 1978; A'Hearn et al., 1995), where cometary activity is primarily influenced by sublimation of water-ice (Meech & Svoren, 2004). A study conducted by Sárneczky et al. (2016) examined 50 long-period comets beyond 5.2

au and found that dynamically new comets exhibited higher activity levels on average and displayed more symmetric comae compared to returning comets. This symmetry suggests the presence of isotropic outflows. However, the orbital coverage for these comets was limited, with an average of only ∼3 observations per comet all with $r_h > 5$ au. Another study by Meech et al. (2009) tracked five comets throughout their orbits spanning heliocentric distances of 5.8 to 14.0 au, aiming to understand the drivers of distant activity by comparing observations with laboratory experiments on cometary ices. They also concluded that DNCs were more active than returning comets and one of their targets exhibited a decrease in the brightening rate as the heliocentric distance decreased, proposed to be related to the annealing of amorphous water-ice. However, all comets in their study had perihelion distances greater than 5.8 au, where water-ice sublimation is inefficient. Our study uses long-term, frequent observations over the region where an already active comet transitions into the regime dominated by water-ice sublimation.

3.2 Overview

In this Chapter, we investigate the activity of dynamically new comets by characterizing their variations in brightness with heliocentric distance compared to returning long-period comets, starting in the region where the main drivers of activity cannot be water-ice sublimation. To ensure consistency, we use telescopes of the same size (1-m) and equipped with standardized instruments and filters (discussed in Section 3.2.1). To capture the temporal variations sufficiently, we conducted frequent observations (every three days) over extended timeframes (approximately one year or longer) and a wide range of

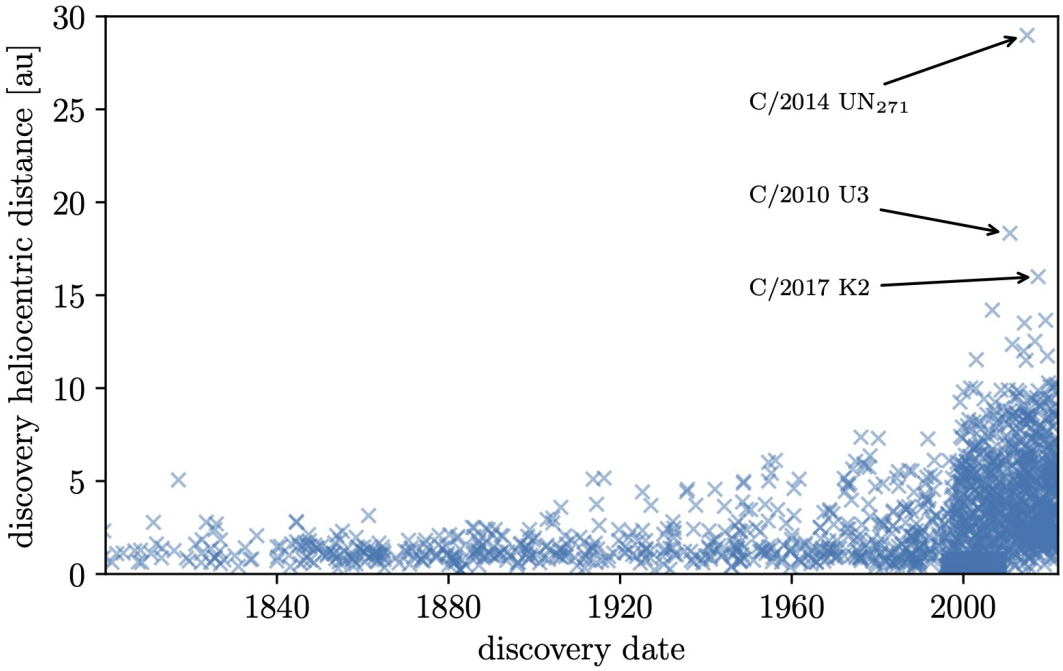

Figure 3.1: **From Lister et al. (2022):** Heliocentric distances at the time of discovery of all the long-period comets discovered after 1801 from the MPC database. The density of points increased significantly after 1996, which is when many of the major moving object sky surveys began.

heliocentric distances ($\Delta r_h > 1$ au). We focus our analysis on the evolution of photometric magnitudes, $g - r$ color, and coma morphology. We discuss our sample, observations, and reductions in Section 3.3, and our analysis methods in 3.4. In Section 3.5, we present our findings for each individual comet in the order of their discovery, including relevant published observations. The collective properties of our sample are examined in Section 2.2.1. Finally, we discuss the implications of our findings in Section 3.7 and conclude with a summary in Section 3.8.

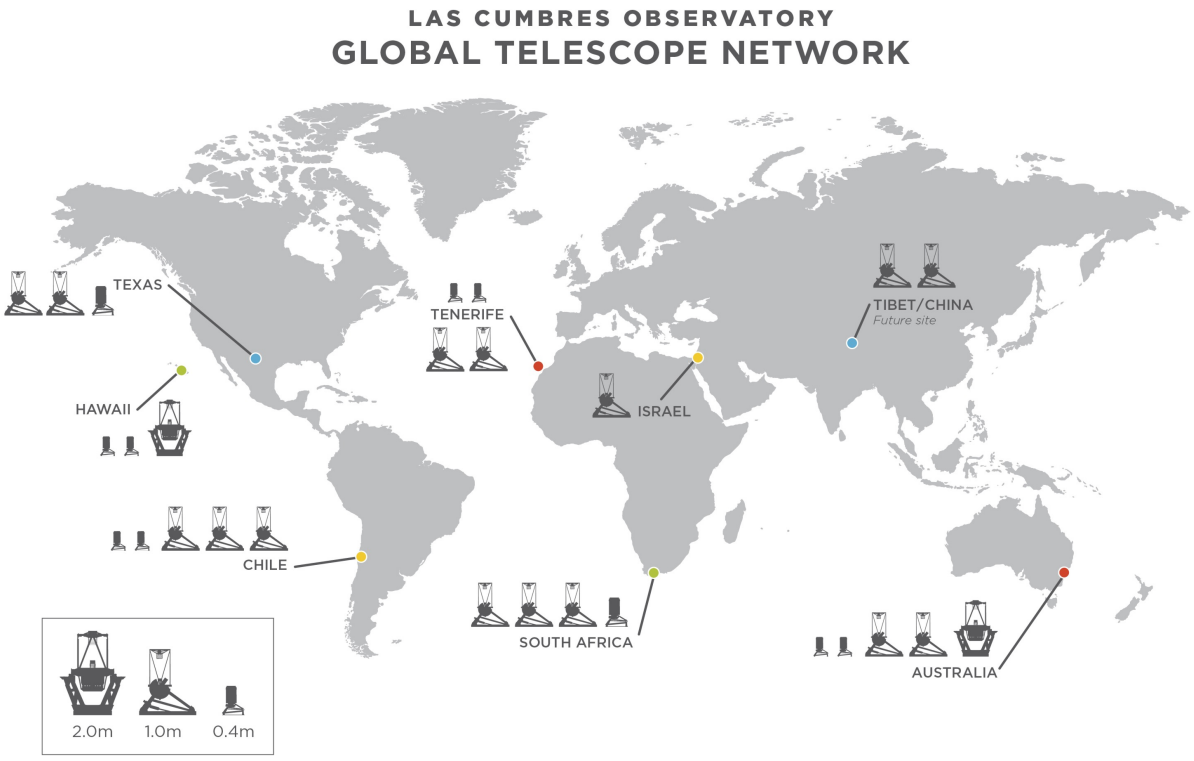

Figure 3.2: **From Lister et al. (2022):** Network map of LCO facilities.

3.2.1 The LOOK Project

The Las Cumbres Observatory (LCO) manages a global network of robotic telescopes, currently consisting of two 2-meter telescopes, thirteen 1-meter telescopes, and ten 40-cm telescopes, housed at six observatory sites in both northern and southern hemispheres (Figure 3.2). The network functions as a single, interconnected observing facility that uses a software scheduler to continuously optimize the observing schedule of each individual telescope. LCO supports a number of large, cohesive, multi-year observing programs called Key Projects that are developed to maximize the scientific results from the unique capabilities of the network.

The LCO Outbursting Objects Key (LOOK) Project is a 3-year Key Project led by

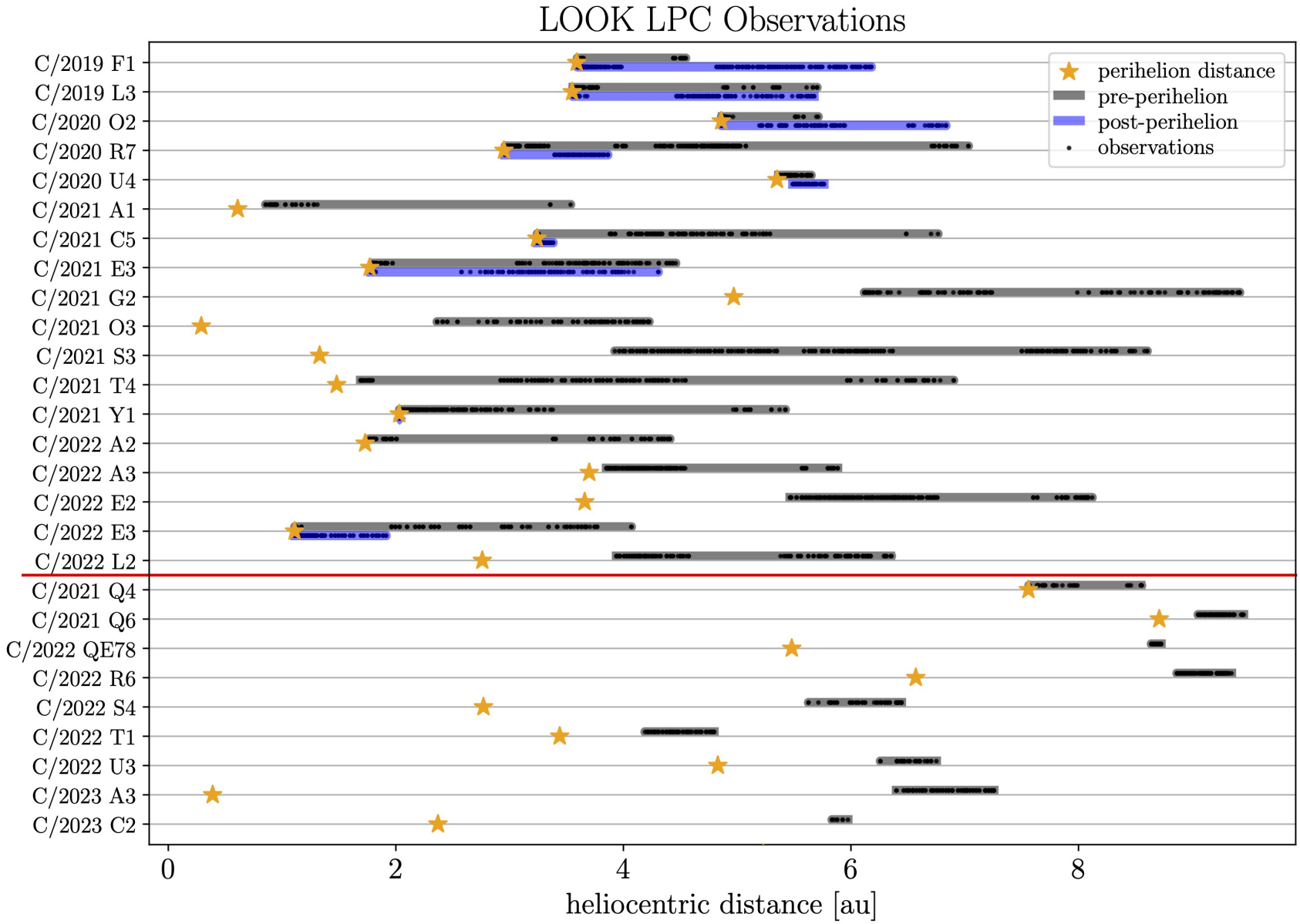

Figure 3.3: A visualization of the heliocentric range of observations for each comet. Each black point represents one visit. The shaded regions show the pre-perihelion range (gray) and post-perihelion range (blue), where the star is the perihelion distance for each comet. All comets above the red line are included in the current chapter. Observations are continuing for all comets, including those below the red line to be included in a future publication.

Co-PIs Lister & Kelley focused on the behavior of active small bodies across the Solar System, utilizing the extensive network of robotic telescopes within the LCO. The project was awarded over 1900 hours of observation time spanning from 2020B to 2023A. First-year results were presented in Lister et al. (2022). The project encompasses two main observing objectives: follow-up of outbursts and long-term monitoring of distant long-period comets (LPCs). I am leading the analysis of LPCs. This chapter presents a summary of the observations and findings related to the LPC aspect of the LOOK Project during its initial three-year phase. We were recently awarded an extension, allowing continued monitoring of LPCs through 2025B.

The LOOK Project has generated more detailed investigations of individual LPCs than are reported in this thesis, including C/2021 A1 (Leonard), which disintegrated in December 2021 and is discussed further in Lister et al. (2022). We also monitored the bright C/2022 E3 (ZTF) through its close approach to Earth and investigated the coma morphology in detail using Lowell Observatory's 42-inch telescope and Discovery Channel Telescope (Knight et al., 2023b). Comet C/2014 UN_{271} (Bernardinelli-Bernstein) has been monitored by LOOK since its discovery announcement, where our team found it to be active at $r_h = 20$ au (Kokotanekova et al., 2021). Because its perihelion distance is greater than 10 au (significantly beyond the heliocentric distance range of this study), we do not include it in our comparison. A summary of the first nine months of LOOK observations of monitoring C/2014 UN_{271} can be found in Kelley et al. (2022). I have contributed to these analyses, but have limited what is presented here to the investigation of the collective sample I am leading.

3.3 Observations and Reduction

3.3.1 Sample & Caveats

As of 2023 June 1, LOOK is monitoring 28 long-period comets (Figure 3.3). Below the red line in Figure 3.3, we show nine objects not included in this study, because they have not yet reached the minimum heliocentric distance range required for our studies but are still being observed for future analysis. We selected targets that were recently discovered inbound with a heliocentric distance $r_h \gtrsim 5\,\mathrm{au}$ and a change in heliocentric distance of at least 1 au ($\Delta r_h \gtrsim 1\,\mathrm{au}$) before perihelion (Table 3.1). Minor Planet Electronic Circulars (MPECs)*, which announce new discoveries, were continuously monitored to identify suitable targets according to our criteria. In most cases, we managed to observe a recently discovered comet within a few days of its announcement.

It is important to address the statistical robustness limited by the sample size. Our study monitored *all* new discoveries of distant comets, though our sample size is relatively small, consisting of only 18 comets for this chapter. The central limit theorem states that the sampling distribution of the sample mean approaches a normal distribution as the sample size increases, and while there is no strict minimum sample size requirement, a commonly suggested guideline is to have a minimum sample of 30 for the theorem to hold approximately. As a result, conducting rigorous statistical tests such as the K-S test, which can be used to compare the distribution of two samples, may be challenging due to the limited number of data points. However, we will make the best use of the available data to

*`https://www.minorplanetcenter.net/mpec/RecentMPECs.html`

derive meaningful insights within the scope of this study. A more comprehensive dataset, encompassing a larger number of comets, would be necessary to perform more definitive tests. Nevertheless, compiling such a dataset is beyond the timescale of this PhD research.

To ensure accurate comparisons across varying heliocentric distances and between different comets, as well as to streamline the analysis of our extensive dataset containing over 7,000 images from 18 comets, we rely on batch processing as our primary method. This approach limits our ability to optimize techniques for individual data points. For instance, while an aperture size of 20,000 km might appear appropriate for comets located between 2 and 3 au from Earth, where the angular size ranges from approximately 9 to 14 arcseconds, our observations encompass a wide range from beyond 8 au to within 1 au of Earth, resulting in angular sizes ranging from less than 3 to more than 28 arcseconds for a 20,000 km aperture. The situation is reversed when using a constant angular aperture size of 5 arcseconds, as it fails to capture the entirety of the coma during observations near Earth. Ultimately, we select the most suitable parameters for the majority of the dataset, while also taking into account the potential impact of those choices on our findings during the discussion of the results.

3.3.2 Instruments

Observations were taken with LCO's global network of 1-m robotic telescopes located at six different observatory sites spanning both the northern and southern hemispheres (Brown et al., 2013). An identical Sinistro imager is mounted on each telescope, which includes a 4096×4096 CCD with a $26'' \times 26''$ FOV, resulting in a pixel scale of $0.39''$ per

pixel. SDSS g' and r' filters were used to probe the gas and dust components of the coma (see Sec 1.2.2).

3.3.3 Data Collection

Once selected, the targets were scheduled for observations using the NEOExchange observation manager (Lister et al., 2021). Observations were scheduled to occur every three days with ± 18 hours flexibility. Because LCO covers both hemispheres, the only major gaps in otherwise continuous coverage were when the comet reaches a solar elongation less than 60 degrees, which typically lasted $\sim$ 4 months depending on the individual orbit geometry. Other constraints included an apparent V magnitude brighter than 20.1 and a Target-Observer-Moon angle greater than 45 degrees. Each observing period consisted of two exposures per filter made at the sidereal rate of each object, typically $\lesssim 1''$/min. Exposure times were nominally $\sim$180 s, but were shortened if tracking the proper motion of the comet would produce star streaks longer than 2 arcseconds as our average seeing was 2 to 3 arcseconds.

3.3.4 Data Reduction

Newly acquired images were automatically pipeline processed by LCO's BANZAI (Beautiful Algorithms to Normalize Zillions of Astronomical Images) pipeline (McCully et al., 2018), which performs basic CCD reduction (bias and dark subtraction and flat-field correction) as well as source extraction and astrometric calibration. The data were then fed into a pipeline created by M. S. P. Kelley (University of Maryland) to conduct the

photometric analysis described below.

The pipeline-produced source catalog is used to photometrically correct each image, calibrating the image to the PanSTARRS 1 (PS1) photometric system (Tonry et al., 2012) using the CALVIACAT software (Kelley & Lister, 2022), the ATLAS-RefCat2 photometric catalog (Tonry et al., 2018), and LOOK Project–derived color corrections. ATLAS-RefCat2 uses the PS1 photometric system, and the photometry pipeline considers a color correction owing to the difference between the PS1 filters and the SDSS filter set used at the LCO telescopes. Photometry calibrated to the PS1 system is hereafter denoted g and r.

The pipeline automatically ignores images that encountered processing issues, such as a missed target, an unknown World Coordinate System solution (WCS), or cases with too few stars for calibration. The remaining images are manually inspected for contamination by passing stars or scattered lunar light. If the image can be calibrated, photometry is attempted on the comet centroid. If centroiding fails, the ephemeris position is used. Photometry is also conducted on coadded images of the same filter from the same observing block. For our time-series photometry and color analysis, we chose an aperture radius of $5.0''$, which is $\sim 15,000$ km at a geocentric distance of 4 au. For our assessment of color evolution, we use a photometric aperture of 20,000 km, which only makes a difference for comets closer to the Sun. In both cases, we limited our analysis to coadded images with point-source full width at half maximum (FWHM) $\leq 4.0''$ and final photometric errors ≤ 0.15 mag, which combined ignores $\sim$7 percent of the observations. While fainter targets were detectable in the images, the signal-to-noise ratio (SNR) was too low for inclusion in the photometric studies presented here. We found our limiting magnitude for the coadded images to be $\sim$21.4 and $\sim$21.0 in the g and r filters, respectively.

Table 3.1: LPCs Monitored by the LOOK Project

Name	T_0[a] [TDB]	r_0[b] [au]	q[c] [au]	r_h[d] [au]	Δ_{r_h}[e] [au]	$1/a_0$[f] $\times 10^6$ [au^{-1}]
C/2019 F1 (ATLAS-Africano)	2020 Aug 13	4.55	3.59	6.18	3.55	28
C/2019 L3 (ATLAS)$^{\gamma}$	2020 Aug 31	5.59	3.55	5.65	4.14	27
C/2020 O2 (Amaral)$^{\gamma}$	2020 Aug 03	5.71	4.86	6.55	2.54	31
C/2020 R7 (ATLAS)	2020 Sep 30	7.03	2.95	3.54	4.67	13
C/2020 U4 (PANSTARRS)$^{\gamma}$	2020 Nov 01	6.57	5.35	5.76	1.63	12
C/2021 A1 (Leonard$^{\gamma}$)	2021 Apr 08	3.55	0.61[g]	0.85	2.70	490
C/2021 C5 (PANSTARRS)$^{\gamma}$	2021 Mar 28	6.78	3.24	3.27	3.57	18
C/2021 E3 (ZTF)	2021 May 08	4.82	1.77	3.84	5.12	-2
C/2021 G2 (ATLAS)$^{\delta}$	2021 Aug 13	9.44	[4.97]	6.35	3.09	15
C/2021 O3 (PANSTARRS)$^{\gamma}$	2021 Aug 03	4.20	0.29[g]	3.01	1.19	-42
C/2021 S3 (PANSTARRS)	2021 Nov 05	8.60	[1.33]	4.18	4.42	15
C/2021 T4 (Lemmon)$^{\gamma}$	2021 Nov 08	6.90	[1.48]	2.92	3.98	32
C/2021 Y1 (ATLAS)	2022 Jan 07	5.42	[2.03]	2.03	3.39	8
C/2022 A2 (PANSTARRS)	2022 Mar 02	4.41	1.73	1.77	2.72	17
C/2022 A3 (ATLAS)	2022 May 15	5.66	[3.70]	4.03	1.63	1153
C/2022 E2 (ATLAS)$^{\delta}$	2022 Apr 02	8.14	[3.66]	5.82	2.32	71
C/2022 E3 (ZTF)$^{\gamma}$	2022 Mar 22	4.07	1.11	1.71	3.56	713
C/2022 L2 (ATLAS)	2022 Jun 22	6.47	[2.76]	4.14	2.33	-12

[a] Date of first LOOK observation
[b] Heliocentric distance of first LOOK observation
[c] Perihelion distance; brackets indicate the comet has not yet reached perihelion
[d] Heliocentric distance of latest LOOK observation
[e] Total range of heliocentric distance observed by LOOK: $r_h - r_0$ if the comet has not yet reached perihelion or $(r_h - q) + (r_0 - q)$ if it has
[f] According to Nakano Note
[g] C/2021 A1 and C/2021 O3 disintegrated near perihelion
$^{\gamma}$ Also observed by the Lowell Discovery Telescope
$^{\delta}$ Also observed by the SOAR Telescope

3.4 Data Analysis

3.4.1 Activity

A commonly used reference normalization to ensure the most accurate comparisons for photometric magnitudes is $H(1, 1, 0)$, representing how bright the comet would be 1 au from the Earth and the Sun and a phase angle of 0°. For our study, apparent magnitudes

m_{app} were converted to heliocentric magnitudes m_{helio}, or $H(1, r_h, 0)$, which is $H(1, 1, 0)$ without removing heliocentric dependencies using the formula:

$$m_{helio} = m_{app} - 5\log_{10}(\Delta) + 2.5\log_{10}(\phi(\alpha)) \tag{3.1}$$

where Δ equals the geocentric distance in au, α is the phase angle (the Sun-Target-Observer angle), and $\phi(\alpha)$ is the phase integral, which is the ratio of the brightness at phase angle α to that at phase angle 0°. To determine $\phi(\alpha)$, we used the Schleicher-Marcus phase function for cometary dust[†], which is a composite of the phase function from comet Halley (Schleicher et al., 1998) for smaller phase angles and the phase function derived in Marcus (2007a,b) for mid- to large-phase angles (Schleicher & Bair, 2011). When using a fixed angular aperture size like 5", an aperture correction is applied by removing a factor of Δ^{-2}.

Each lightcurve was fit with a curve that follows:

$$m_{helio} = H(1, 1, 0) + 2.5n\log_{10}(r) \tag{3.2}$$

where $H(1, 1, 0)$ is the absolute magnitude and n is the *activity index*, which is used to quantify the increase of brightness associated with heliocentric distance including geometric effects and activity. An object experiencing no change in the rate of activity would have an activity index of $n = 2$, where the only increase in brightness is due to the increasing reflected sunlight. We start by modeling the entire dataset for pre- or post-perihelion using a least-squares fit to the r photometry. If the residuals of the fit are not contained within

[†]`http://asteroid.lowell.edu/comet/dustphase.html`

2σ of the median magnitude error, then the light curve was fit with a broken law. An n value less than 2 indicates a decrease in intrinsic brightness, occasionally observed as a pre- or post-perihelion peak in brightness. We show the activity indices and corresponding heliocentric distances for each comet in Table 3.2.

We can also assess the dust production using calculations of $Af\rho$, an aperture-independent quantity used as an estimator for dust production, which is the product of the albedo "A", the filling factor "f" (i.e., how much the total cross-section of grains fills the field-of-view), and the radius of the coma "ρ" (A'Hearn et al., 1984). We measured the $A(0°)f\rho$, which is $Af\rho$ corrected to a phase angle of 0 deg using the Schleicher-Marcus dust phase function (Schleicher & Bair, 2011), through each comet's orbit. We show the range of $A(0°)f\rho$ for each comet in Table 3.3.

3.4.2 Colors

By comparing the apparent magnitudes produced from the co-added images in the g and r bandpasses, we were able to determine the $g-r$ color for each visit. We then analyzed the $g-r$ color across the range of heliocentric distances for each comet. If there was no discernable change, the median value is used across all ranges (Table 3.3). Six objects exhibited a color change throughout our observations. In those instances, we either measure the median of each section of observations or determine a linear fit to the $g-r$ color versus r_h, except for C/2021 A1, which had a more dramatic color change that was fit with a polynomial. We discuss the color changes of the individual comets and how they relate to brightness changes in Section 3.5.

Table 3.2: Activity Indices

Name	r_{min} [a] [au]	r_{max} [b] [au]	n [c]	$1/a_0 \times 10^6$ [d] [au^{-1}]
C/2019 F1 (ATLAS-Africano)	3.60	3.77	4.7 ± 0.3	28
	4.87	5.75	3.2 ± 0.1	
	5.85	6.14	6.2 ± 0.4	
C/2019 L3 (ATLAS)	-5.70	-4.88	6.3 ± 0.2	27
	-3.70	-3.56	8.1 ± 0.2	
	4.48	4.89	5.4 ± 0.2	
	4.91	5.63	4.5 ± 0.1	
C/2020 O2 (Amaral)	5.27	5.94	3.8 ± 0.1	31
C/2021 C5 (PANSTARRS)	-5.23	-4.13	5.5 ± 0.1	18
C/2021 E3 (ZTF)	-4.46	-3.82	5.4 ± 0.1	-2
	-3.72	-3.09	3.3 ± 0.1	
	2.58	3.17	2.8 ± 0.1	
C/2021 G2 (ATLAS)	-9.42	-8.09	7.0 ± 0.3	15
	-7.24	-6.12	3.6 ± 0.1	
C/2021 S3 (PANSTARRS)	-8.58	-7.50	6.2 ± 0.3	15
	-6.26	-5.10	3.5 ± 0.1	
	-5.04	-3.96	2.3 ± 0.1	
C/2021 T4 (Lemmon)	-4.38	-2.92	1.9 ± 0.1	32
C/2021 Y1 (ATLAS)	-3.02	-2.58	2.2 ± 0.1	8
C/2022 A2 (PANSTARRS)	-4.36	-3.38	3.6 ± 0.1	17
	-2.01	-1.91	6.5 ± 0.1	
C/2022 A3 (ATLAS)	-4.53	-4.26	4.3 ± 0.2	1153
C/2022 E2 (ATLAS)	-8.08	-6.46	7 ± 0.1	71
	-6.41	-6.05	3.3 ± 0.2	
C/2022 E3 (ZTF)	-3.77	-1.96	2.9 ± 0.1	7133
	1.19	1.38	3.9 ± 0.1	
C/2022 L2 (ATLAS)	-6.04	-5.41	2.9 ± 0.2	-12
	-4.42	-3.97	1.5 ± 0.2	

[a] Starting heliocentric distance where a negative value represents pre-perihelion.
[b] Ending heliocentric distance where a negative value represents pre-perihelion.
[c] Activity index as defined in Equation 3.2 determined by least-squares fit with 1σ errors
[d] Reciprocal original semi-major axis $\times 10^6$ au^{-1}

Table 3.3: Color & $Af\rho$

Name	$g-r$[a]	$A(0°)f\rho$ [cm][b]		
		p10	median	p90
C/2019 F1 (ATLAS-Africano)[c]	0.50 ± 0.03	768	1586	1760
C/2019 L3 (ATLAS)	0.48 ± 0.01	11412	20753	30538
C/2020 O2 (Amaral)	0.48 ± 0.03	1072	1872	1976
C/2020 R7 (ATLAS)	0.51 ± 0.02	642	1254	1368
C/2020 U4 (PANSTARRS)	0.55 ± 0.08	265	322	384
C/2021 A1 (Leonard)[c]	0.47 ± 0.05	636	1469	1718
C/2021 C5 (PANSTARRS)	0.48 ± 0.04	169	227	276
C/2021 E3 (ZTF)[c]	0.49 ± 0.05	533	969	1646
C/2021 G2 (ATLAS)	0.49 ± 0.05	1607	3814	4862
C/2021 O3 (PANSTARRS)	0.48 ± 0.03	74	105	135
C/2021 S3 (PANSTARRS)	0.56 ± 0.03	996	2978	3256
C/2021 T4 (Lemmon)	0.50 ± 0.04	202	769	805
C/2021 Y1 (ATLAS)[c]	0.47 ± 0.02	474	568	626
C/2022 A2 (PANSTARRS)[c]	0.50 ± 0.08	184	3142	4616
C/2022 A3 (ATLAS)	0.51 ± 0.04	212	529	575
C/2022 E2 (ATLAS)	0.48 ± 0.02	1084	3344	3744
C/2022 E3 (ZTF)[c]	0.54 ± 0.03	2770	3972	4804
C/2022 L2 (ATLAS)	0.52 ± 0.03	651	957	1078

[a] Median $g-r$ color $\pm 1\sigma$ using a 20,000 km aperture
[b] 10, 50, and 90 percentile of $A(0°)f\rho$ values
[c] Experienced a change in color during observations

3.4.3 Coma Morphology

For the morphology analysis, we utilize nightly co-added images (also called "stacks") as well as monthly stacks, where the nightly stacks of each filter are median-combined with other nightly stacks of the same month and filter. Given the presence of bright C_2 emission bands in the g filter and the absence of such bands in the r filter (see discussion in Section 1.2.2), we generated simulated "gas" images. This was achieved by scaling an r image and subtracting it from the corresponding g image. The scaling coefficient was visually determined based on the disappearance of the dust tail in the resulting "gas" image,

with varying coefficients for each comet, as detailed in Section 3.5. To enhance the images, we subtracted the azimuthal median (Schleicher & Farnham, 2004; Samarasinha & Larson, 2014) to eliminate bulk brightness and highlight subtle brightness variations. We found that the five comets exhibiting a bluer color shift near the Sun, indicating a potential alteration in gas production, were the only ones for which a "gas" image could be determined.

3.4.4 Dynamical Age

As discussed in Section 1.4, the $1/a_0$ parameter is commonly used as a proxy for dynamical age. We compare the $1/a_0$ values for the comets in our sample derived from two different sources: orbital computations by Syuichi Nakano published on their Nakano Note website[‡] and the Minor Planet Center (MPC) Database[§]. When we compared the $1/a_0$ distribution for our sample from both sources, we found that the Nakano Note values followed a distribution similar to modeled distributions (e.g., Dybczyński & Królikowska, 2016) with nearly all of the objects having $1/a_0 > 0$, while MPC values have a much wider range with many objects having $1/a_0 < 0$ (Figure 3.4). This disparity could stem from different methods of dynamical modeling, as Nakano Note includes non-gravitational effects and MPC may not. Neglecting the non-gravitational effects tends to produce original orbits that appear more hyperbolic than they actually are (Marsden & Sekanina, 1973; Królikowska, 2001). Another possibility is that Nakano Note may update their calculations more frequently as more observations are being submitted. For this chapter, we use the Nakano Note $1/a_0$ values.

[‡] `http://www.oaa.gr.jp/~oaacs/nk.htm`
[§] `https://www.minorplanetcenter.net/db_search/`

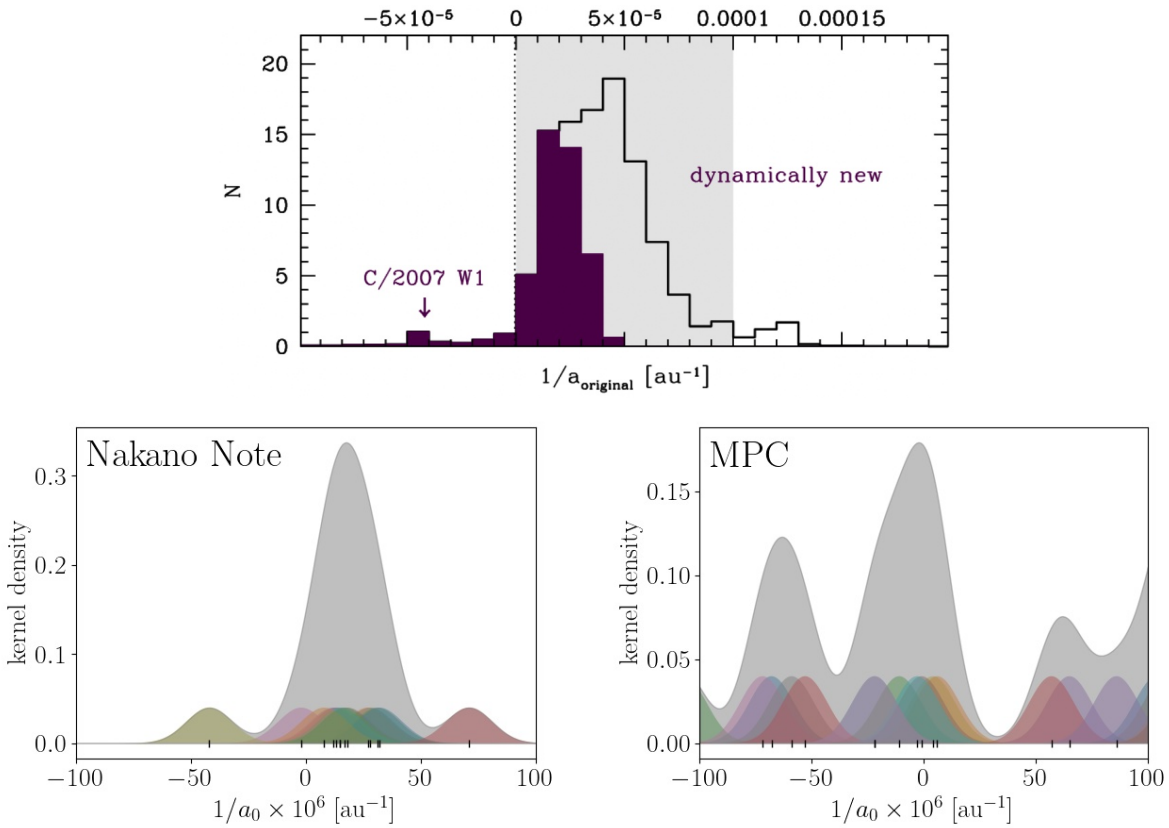

Figure 3.4: The distribution of $1/a_0$ values of our sample from two different sources: Nakano Note (**bottom left**) and Minor Planet Center (**bottom right**) compared with results from Dybczyński & Królikowska (2016) (**top**). The colored Gaussian kernels describe the individual $1/a_0$ values and are added together to make up the larger grey kernel density plot. The Nakano Note distribution is more similar to the distribution from Dybczyński & Królikowska (2016) with nearly all of the objects having $1/a_0 > 0$ compared to the MPC distribution.

3.5 Time-series Photometry Results

3.5.1 C/2019 F1 (ATLAS-Africano)

Comet C/2019 F1 (ATLAS-Africano) was discovered 2019 Mar 28 and 29 by ATLAS and Mt Lemmon Survey at $r_h = 7.65$ au with a magnitude of 18.3 in the orange filter and at $r_h = 7.64$ au with a magnitude of 18.4 in the G filter, respectively (Africano et al., 2019). LOOK has been observing this comet since the beginning of the Key Project with

the first observation 2020 Aug 13 at $r_h = 4.55$ au. Monitoring continued as the comet passed perihelion at $q = 3.59$ au 2021 Jun 22 until its latest position 2023 Jan 31 at $r_h = 6.18$ au, a range of 3.55 au over ~ 2.5 years. The reciprocal of the original semi-major axis $1/a_0 = 2.8 \times 10^{-5}$ au^{-1} suggests this comet is probably dynamically new.

C/2019 F1 was found to be decreasing in intrinsic brightest ($n < 2$) during initial observations (Figure 3.5). This decline could be a continuous decrease in brightness leading up to perihelion or, alternatively, the comet may have been discovered during an outburst that subsequently faded and then experienced a brightness increase prior to perihelion. Due to the significant gap in observations following the initial ones, no definitive conclusions can be drawn at this time.

A color change was observed where C/2019 F1 became slightly redder near perihelion ($g - r = 0.47 \pm 0.03$ to $g - r = 0.51 \pm 0.02$). Unlike the other comets in this sample that experience color changes, C/2019 F1 exhibits a unique distinction as its color shifts *redder* and the shift occurs at distances beyond 3 au from the Sun. Colors will be discussed further in Section 3.6.2.

3.5.2 C/2019 L3 (ATLAS)

Comet C/2019 L3 (ATLAS) was discovered 2019 Jun 10 by the ATLAS survey with $r_h = 8.46$ au and m_{app} of 18.1 in the orange filter (MPEC 2019-Q20). LOOK has been observing this comet since the project started in the 2020B semester with the first observations taking place 2020 Aug 31 when the comet was at $r_h = 5.59$ au. Observations continued as the comet passed perihelion at $q = 3.55$ au 2022 Jan 09 until its latest ob-

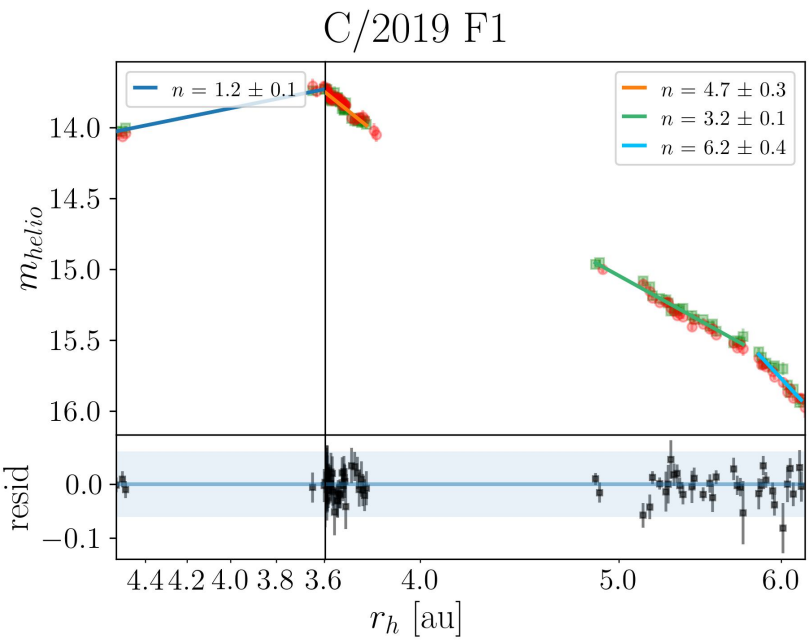

Figure 3.5: The upper panels show the variation of m_{helio} of C/2019 F1 (ATLAS-Africano) with heliocentric distance. The red circles represent the r magnitudes and the green squares represent the g magnitudes minus the $g-r$ color, which for C/2019 F1 is 0.50 ± 0.03. The solid lines represent the best-fit activity index n to the g magnitudes for each section, determined by the least squares method. We include the χ^2 value for each n fit in the legend. The bottom panels show the residuals of the fit and the shaded region is the median 2-σ magnitude error. The left panels are pre-perihelion, and the right post-perihelion and the x-axis is in log scale.

served position of $r_h = 5.65$ au 2023 June 01, with a total observed range of $\Delta r_h = 4.14$ au over > 2.5 years. The reciprocal of the original semi-major axis $1/a_0 = 2.7 \times 10^{-5}$ au^{-1} suggests this comet is most likely dynamically new.

C/2019 L3 exhibited the steepest increase in activity of the sample with $n = 6.3 \pm 0.2$, later increasing to $n = 8.1 \pm 0.2$ within 5 au of the Sun. After a post-perihelion peak in activity, m_{helio} decreased as $n = 5.4 \pm 0.2$ then $n = 4.5 \pm 0.1$ (Figure 3.6). Color was constant throughout observations, both pre- and post-perihelion with $g - r = 0.48 \pm 0.01$.

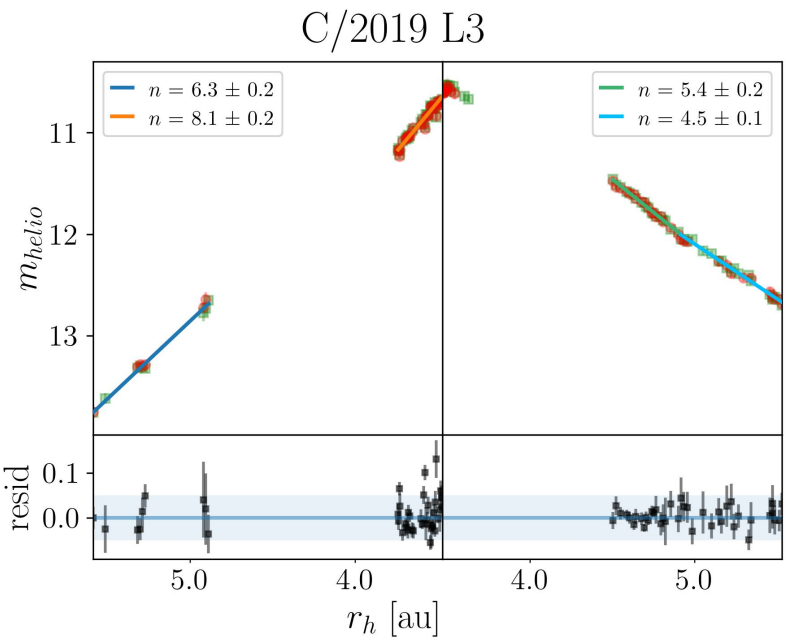

Figure 3.6: Same as Figure 3.5 for C/2019 L3 (ATLAS) using $g - r = 0.48 \pm 0.01$.

3.5.3 C/2020 O2 (Amaral)

Comet C/2020 O2 (Amaral) was discovered 2020 Jul 23 by Leonardo S. Amaral at the Observatório Campo dos Amarais with $m_{app} = 18.1$ in the r filter and $r_h = 5.84$ au (MPEC 2020-P10). LOOK observed this comet from the beginning of the 2020B semester 2020 Aug 03 when it had a heliocentric distance $r_h = 5.84$ au through perihelion at $q = 4.86$ au 2021 Aug 28 until the latest observation 2023 Mar 31 with $r_h = 6.55$ au. The comet was in a crowded star field during the latest observations and m_{app} was approaching the limiting magnitude, so we only include observations through 2022 Nov 15 with $r_h = 5.94$ au in this analysis. The reciprocal of the original semi-major axis $1/a_0 = 3.1 \times 10^{-5}$ au^{-1} suggests this comet is likely dynamically new, but since it is near the "cut-off" of 4×10^{-5} au^{-1}, it could be returning.

Comet C/2020 O2 exhibited a constant brightness as it approached perihelion ($n \sim 2$),

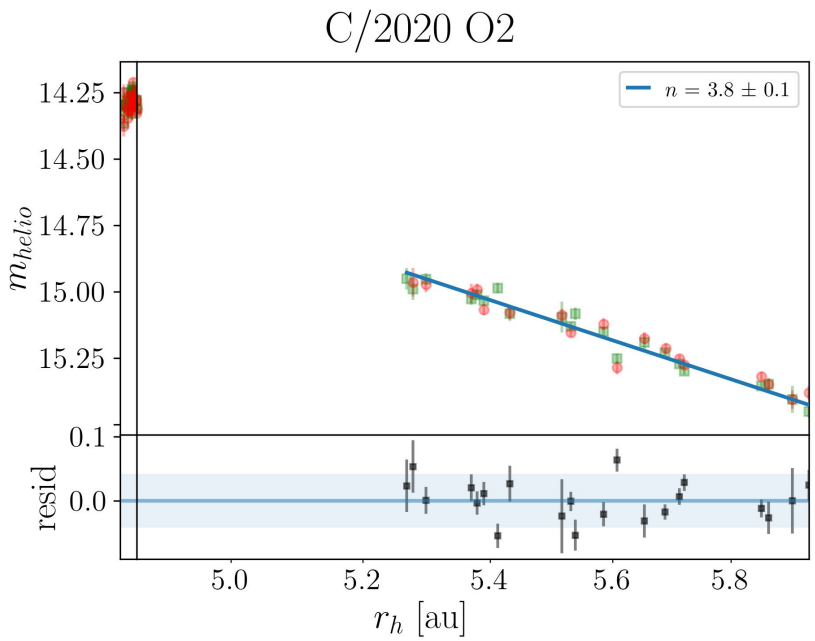

Figure 3.7: Same as Figure 3.5 for C/2020 O2 (Amaral) using $g - r = 0.48 \pm 0.03$.

but the range of heliocentric distance was too small to conduct a proper least-squares fit. Following a gap of 7 months post-perihelion, the comet faded at a rate of $n = 3.8 \pm 0.1$ from 5.2 – 5.9 au (Figure 3.7). The comet maintained a color of $g - r = 0.48 \pm 0.03$ throughout observations.

3.5.4 C/2020 R7 (ATLAS)

Comet C/2020 R7 (ATLAS) was discovered by the ATLAS survey 2020 Sep 15 with $r_h = 7.13$ au and magnitude of 19.0 in the orange filter (MPEC 2020-S168). Observations by the LOOK project began 2020 Sep 30 when $r_h = 7.03$ au through perihelion at $q = 2.95$ au on 2022 Sep 16 until the most recent observations 2023 May 29 with $r_h = 3.86$ au resulting in $\Delta r_h = 4.99$ au over more than 2.5 years. C/2020 R7 is predicted to be dynamically new with $1/a_0 = 1.3 \times 10^{-5}$ au^{-1}.

C/2020 R7 first exhibited an increase of activity of $n = 5.9 \pm 0.8$ at the start of

observations when $r_h \sim 7$ au until a slight decrease that quickly flattened out to $n = 2.0 \pm 0.4$ around 5 au. This "bump" in the secular light curve could be explained by seasonal effects, where active areas move into and out of sunlight throughout the orbit. Starting in 2022 at $r_h \sim 3.4$ au, C/2020 R7 had a constant activity level of $A(0^\circ)f\rho \sim 1500$ cm for six weeks until a decrease in brightness occurred near $r_h \sim 3.1$ au. The decrease resulted in a decrease in apparent magnitude from 15.1 to 15.8 over two months before perihelion. Because the activity picks up again post-perihelion, we can rule out volatile depletion as a cause of the pre-perihelion activity peak. Therefore, the more likely explanation for this behavior is seasonal effects. If this is true, then it is unlikely that C/2020 R7 is dynamically new since seasonal effects imply the presence of less active surface areas created by a previous solar passage. Post-perihelion, the brightness decreased as $n = 5.0 \pm 0.1$ from $r_h = 3.4$ to 3.9 au (Figure 3.8). While several changes in brightness occurred throughout C/2020 R7's observed epoch, no drastic color changes occurred during observations, holding at $g-r = 0.51 \pm 0.02$. It is worth noting that overall the changes in magnitude are minimal with $H(1, 1, 0)$ (not plotted) ranging only one magnitude throughout pre-perihelion observations.

3.5.5 C/2020 U4 (PANSTARRS)

Comet C/2020 U4 (PANSTARRS) was discovered with a magnitude of 20.1 in the w filter and $r_h = 6.62$ au on 2020 Oct 22 (MPEC 2020-U260). The LOOK project began observing the target 2021 Aug 07 with $r_h = 5.65$ au through perihelion at $q = 5.35$ until the latest observations 2023 Jan 21 with $r_h = 5.76$ au. C/2020 U4 is most likely dynamically new with $1/a_0 = 1.2 \times 10^{-5}$ au^{-1}

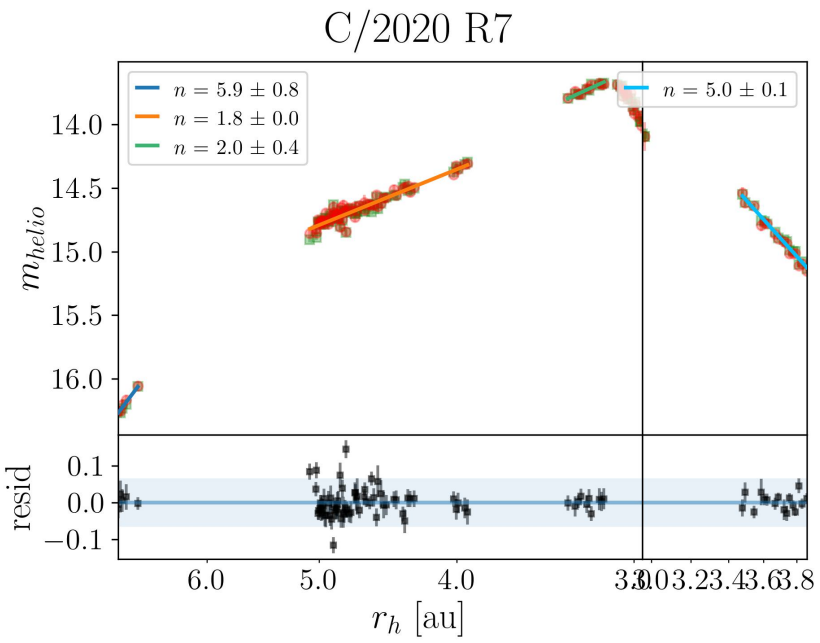

Figure 3.8: Same as Figure 3.5 for C/2020 R7 (ATLAS) using $g - r = 0.51 \pm 0.02$.

C/2020 U4 has the shortest heliocentric distance coverage of our sample with $\Delta r = 0.71$ au. The light curve dips in brightness during perihelion, correlating with a geocentric distance local maximum, even though geometric effects have been accounted for (Figure 3.9). However, the shape of the pre- and post-perihelion curves do not align with geocentric distance or phase angle. It is worth noting that the magnitude range of m_{helio} is less than 0.7. The steep activity index of $n \sim 11$ post-perihelion is not discussed further because of the limited range in r_h.

3.5.6 C/2021 A1 (Leonard)

Comet C/2021 A1 was discovered by Gregory J. Leonard 2021 Jan 03 with a magnitude of 19.0 in the G filter and $r_h = 5.08$ au at the Mt. Lemmon Observatory (Leonard et al., 2021). The LOOK project made a single observation 2021 Jun 09 at $r_h = 3.36$ au and began monitoring consistently from 2021 Nov 06 at $r_h = 1.31$ au until 2021 Dec 06 at

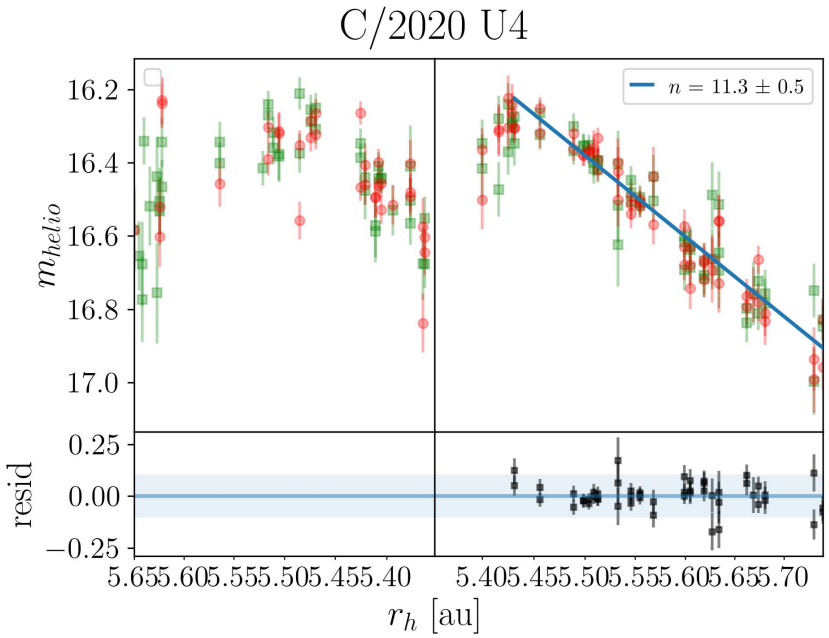

Figure 3.9: Same as Figure 3.5 for C/2020 U4 (PANSTARRS) using $g - r = 0.55 \pm 0.08$.

$r_h = 0.86$ au. C/2021 A1 made its close approach to Earth with $\Delta = 0.23$ au on 2021 Dec 12 followed by perihelion 2022 Jan 03 where $q = 0.62$ au. A reciprocal semi-major axis outside of the Oort spike $1/a_0 = 4.9 \times 10^{-4}$ au^{-1} suggests this comet is not dynamically new.

C/2021 A1 is one of the two comets in our sample that experienced disintegration. It is notable for its brightness, reaching a peak apparent magnitude brighter than 3, which has led to extensive study (e.g., Faggi et al., 2023; Jewitt et al., 2023). Prior to its disintegration, a decline in the rate of brightening was observed starting in mid-November, a finding that was corroborated by other observers[¶]. Multiple outbursts were reported after our observations ended throughout the month of December (e.g., Crovisier et al., 2021). Jewitt et al. (2023) argue rotational instability as the most plausible disruption mechanism, accelerated by the sublimation of buried volatiles.

[¶]https://groups.io/g/comets-ml/message/30254

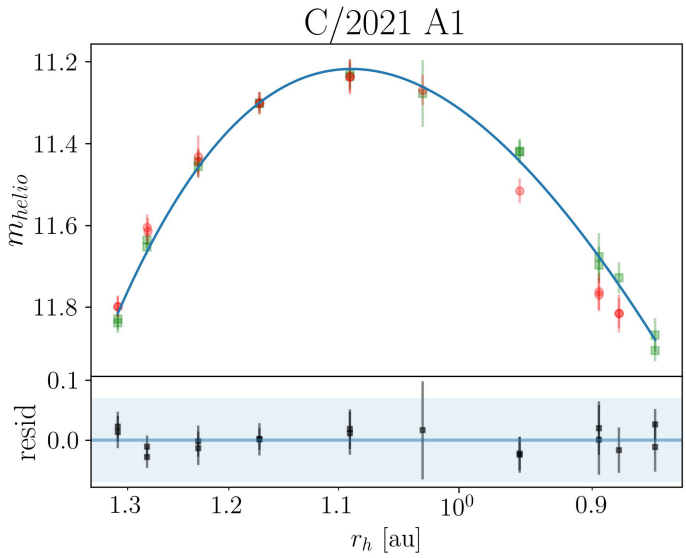

Figure 3.10: Same as Figure 3.5 for C/2021 A1 (Leonard) using $g - r = 0.47 \pm 0.05$.

When we assess the coma morphology of the enhanced synthetic gas image, we immediately identify two jets oriented near positional angles 40° and 220° (Figure 3.11). The jets appear to be nearly perpendicular to the tail, which extends to the northwest direction of the dust images, though a very faint residual dust tail is still observed in the northwest direction of the "gas" image.

The LOOK data are significantly better described by a second-order polynomial rather than Equation 3.4 (Figure 3.10). The $g - r$ color is also best fit with a polynomial where the color ranges from $g - r = 0.27 \pm 0.05$ to $g - r = -0.30 \pm 0.09$ using a 20,000 km aperture over $\Delta r_h \sim 0.5$ au. As discussed in Section 3.3.4, we use a 20,000 km aperture for color analysis as opposed to the 5″ aperture used for the lightcurve analysis. The data in Figure 3.10, measured using a 5″ aperture, exhibited a less extreme color change than the 20,000 km aperture measurements described above, probably because the smaller aperture (5″) does not contain as much of the gas coma. The decrease in color occurred earlier than the decrease in brightness, which could indicate that an increase in gas production that

contributed to the disintegration occurred prior to early November.

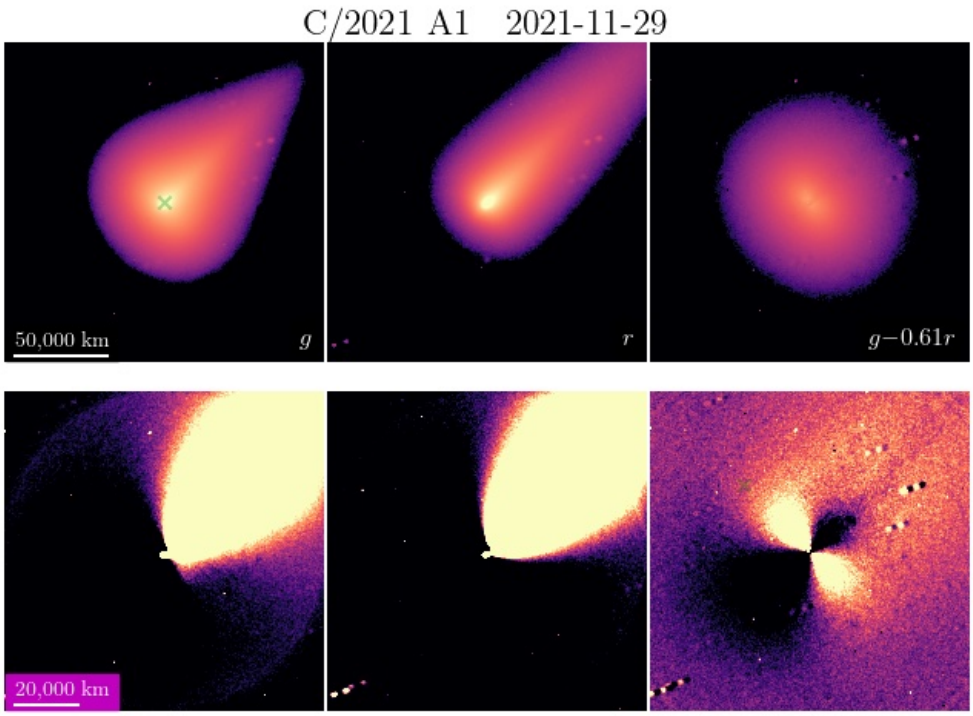

Figure 3.11: Unenhanced (top row) and enhanced (bottom row) images of C/2021 A1 (Leonard) in g and r filters (left and middle column) and a synthetic "gas" image (right column) on 2021 November 29. The synthetic "gas" image was created by scaling an r image (median of all images taken that night) by the estimated dust color and subtracting this scaled image from a median-combined g image. All images are centered on the opto-center of the comet with north up and east to the left. Light is bright and dark is faint in all panels. The images in the top and bottom row are 200,000 km and 100,000 km across, respectively. The images in the bottom row have been enhanced by subtracting the azimuthal median profile. The morphology of this synthetic gas image is very different from the "dust" (r-band) image. Two jets can be seen oriented near positional angles 40° and 220° (measured from north through east) in the enhanced gas images, seemingly perpendicular to the tail in the northwest direction in the dust images, though a very faint residual dust tail is still in the northwest direction of the "gas" image. This image uses the same data and creation process as Figure 11 in Lister et al. (2022).

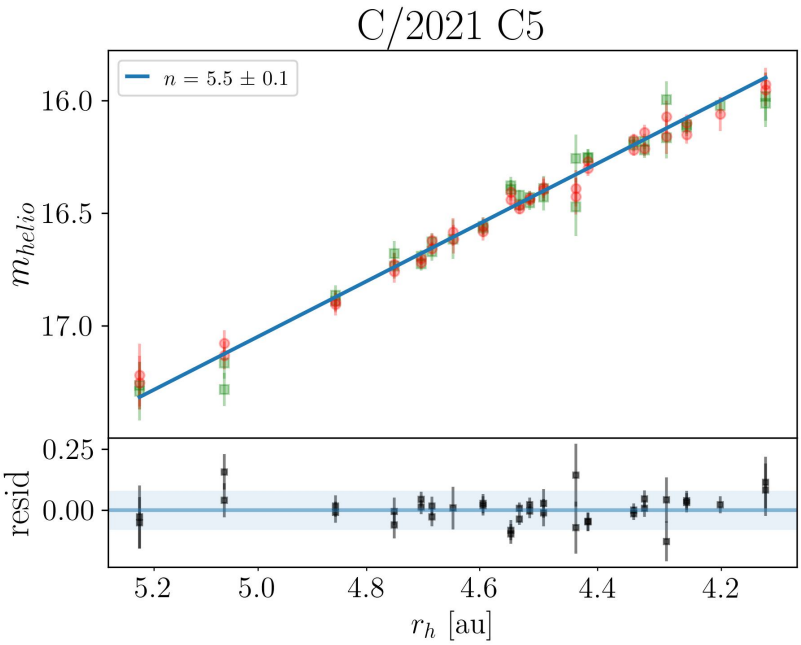

Figure 3.12: Same as Figure 3.5 for C/2021 C5 (PANSTARRS) using $g - r = 0.48 \pm 0.04$. Only pre-perihelion observations are shown.

3.5.7 C/2021 C5 (PANSTARRS)

Comet C/2021 C5 (PANSTARRS) was discovered 2021 Feb 12 with a heliocentric distance $r_h = 7.07$ au (MPEC 2021-E64). LOOK has observed this comet since 2021 Mar 28 when $r_h = 6.78$ au until 2022 May 24 when $r_h = 4.06$ au. The reciprocal of the original semi-major axis $1/a_0 = 1.8 \times 10^{-5}$ au^{-1} suggests this comet is most likely dynamically new. C/2021 C5 maintained a brightness increase of $n = 5.5 \pm 0.1$ (Figure 3.12) and a steady color of $g - r = 0.48 \pm 0.04$.

3.5.8 C/2021 E3 (ZTF)

Comet C/2021 E3 was discovered 2021 Mar 09 by ZTF with a magnitude of 19.6 in the r filter when $r_h = 5.34$ au (Bolin et al., 2021). The LOOK project began observing

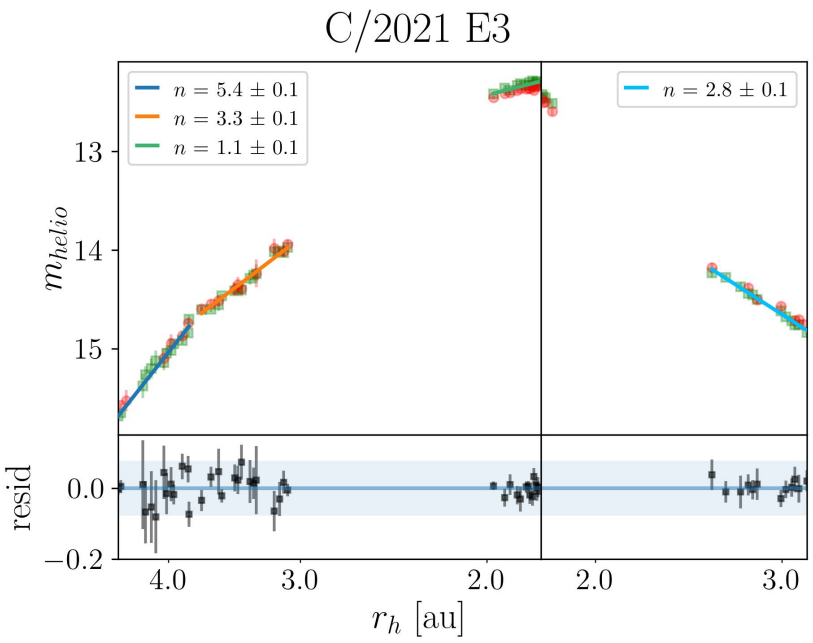

Figure 3.13: Same as Figure 3.5 for C/2021 E3 (ZTF) using $g - r = 0.49 \pm 0.05$.

this comet 2021 May 08 when $r_h = 4.82$ au through perihelion at $q = 1.77$ au on 2022 June 11 until 2023 Mar 29 with $r_h = 3.84$ au. Observations span $\Delta r_h = 5.12$ au over nearly two years. C/2021 E3 is most likely dynamically new with $1/a_0 = -2 \times 10^{-6}$ au^{-1}.

C/2021 E3 increased in brightness as $n = 5.4 \pm 0.1$ until the rate decreased to $n = 3.3 \pm 0.1$ near 3.7 au. The object began to decrease in brightness ($n < 2$) before perihelion (Figure 3.13), as well as exhibited a change in color from $g - r = 0.48 \pm 0.08$ to $g - r = 0.40 \pm 0.03$. Post-perihelion, the color returns to $g - r = 0.48 \pm 0.04$, and the brightness decreases as $n = 2.8 \pm 0.1$. The synthetic gas image exhibits asymmetry likely caused by jets on the surface (Figure 3.14). The potential jets along with the pre-perihelion peak in intrinsic brightness provide evidence that C/2021 E3 may not be as dynamically new as the reciprocal semi-major axis suggests.

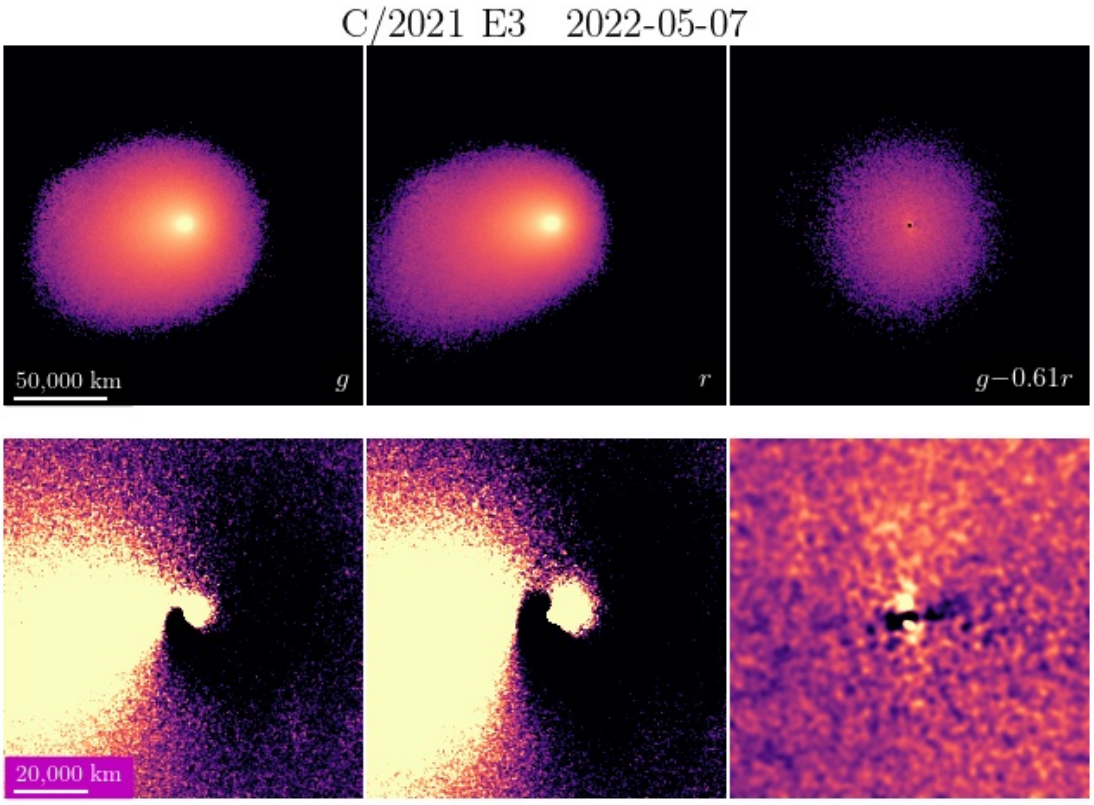

Figure 3.14: Same as Figure 3.11 for median-combined images of C/2021 E3 (ZTF) from May 2022. The synthetic "gas" image in the bottom right panel has been smoothed using a 2-σ gaussian filter. The image shows faint wide fan-like features near position angle 10° and 190°, perpendicular to the darkest regions.

3.5.9 C/2021 G2 (ATLAS)

C/2021 G2 (ATLAS) was discovered inactive 2021 Apr 11 with a magnitude of 19.3 in the cyan filter and $r_h = 10.12$ au (MPEC 2021-M79). The LOOK project has observed this comet since 2021 Aug 13 at $r_h = 9.44$ au until the most recent observations 2023 Apr 05 with $r_h = 6.35$ au. We found C/2021 G2 to be active 2021 Sep 29 at $r_h = 9.19$ au using the 4-m SOAR telescope (Holt et al., 2022b). A reciprocal semi-major axis of $1/a_0 = 1.5 \times 10^{-5}$ au^{-1} suggests this comet is dynamically new.

C/2021 G2 had an initial increase in brightness as $n = 7.0 \pm 0.3$ until 8.0 to 7.3 au

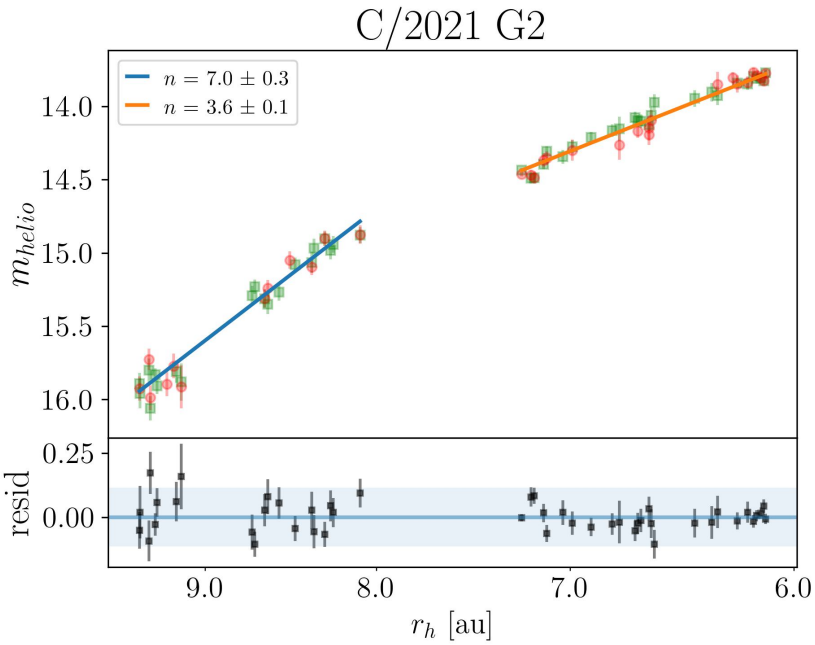

Figure 3.15: Same as Figure 3.5 for C/2021 G2 (ATLAS) using $g - r = 0.49 \pm 0.05$. Only pre-perihelion data are shown.

when the rate of brightness increase lessened to $n = 3.6 \pm 0.1$ (Figure 3.15). While we apply a broken power law to describe the data, it is also possible that the activity index n was changing linearly with heliocentric distance, which we discuss further in Section 3.7.1. A color of $g - r = 0.49 \pm 0.05$ was maintained throughout observations.

3.5.10 C/2021 O3 (PANSTARRS)

Comet C/2021 O3 (PANSTARRS) was discovered 2021 Jul 26 when $r_h = 4.31$ au and $m_{app} = 19.8$ in the i filter (MPEC 2021-P05). The LOOK project began observing this object 2021 Aug 03 from $r_h = 4.20$ to $r_h = 3.01$ au 2021 Nov 10. Once it reached a smaller solar elongation angle, C/2021 O3 was not observable again until after reaching a perihelion of $q = 0.29$ au 2022 Apr 20. However, it was found to be disintegrated 2022 Apr 29 (Zhang et al., 2022), making it one of two disintegrated comets in our sample (the

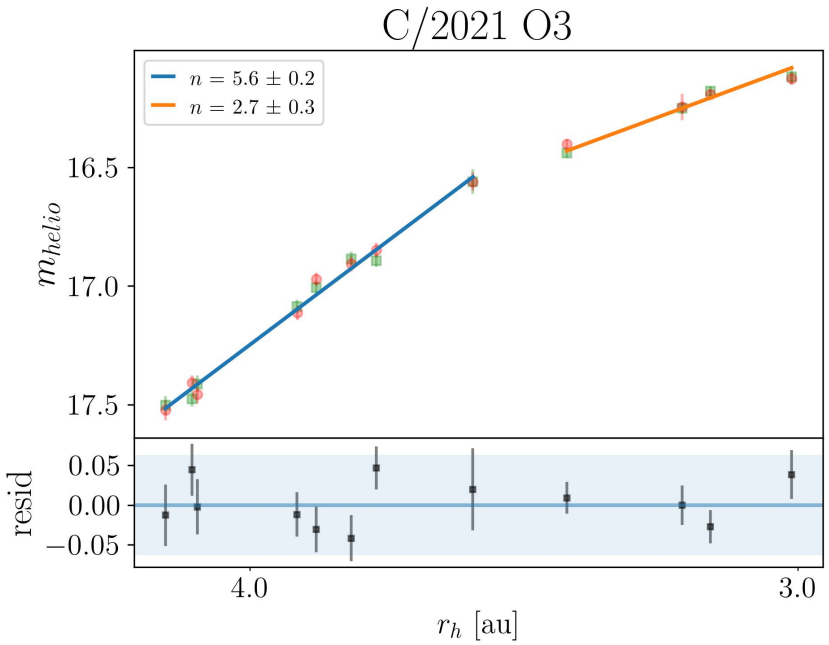

Figure 3.16: Same as Figure 3.5 for C/2021 O3 (PANSTARRS) using $g - r = 0.48 \pm 0.03$. Only pre-perihelion data are shown.

other being comet C/2021 A1). C/2021 O3 had the lowest reciprocal semi-major axis of the sample with $1/a_0 = -4.2 \times 10^{-5}$ au^{-1} — a value similar to $1/a_0 = -4.3 \times 10^{-5}$ au^{-1}, the reciprocal semi-major axis of C/2007 W1 (Boattinni), which has been suggested to be a candidate for interstellar origin (Dybczyński & Królikowska, 2015).

The activity of C/2021 O3 initially increased as $n = 5.6 \pm 0.2$ before n began to gradually decrease (Figure 3.16). However, $H(1, 1, 0)$ only varied by less than one magnitude throughout observations. The color remained constant with $g - r = 0.48 \pm 0.03$.

3.5.11 C/2021 S3 (PANSTARRS)

Comet C/2021 S3 was discovered on 2021 Sep 24 with an apparent magnitude of 20.1 in the i filter and $r_h = 8.92$ au (Bulger et al., 2021). The LOOK project began observing this comet 2021 Nov 05 when $r_h = 8.60$ au through the most recent observations 2023 Apr

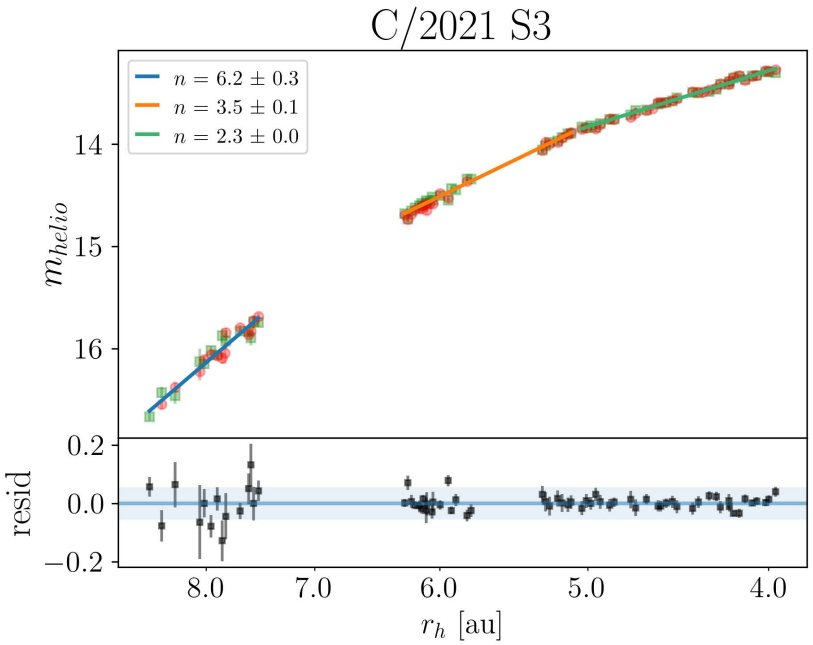

Figure 3.17: Same as Figure 3.5 for C/2021 S3 (PANSTARRS) using $g - r = 0.56 \pm 0.03$. Only pre-perihelion data are shown.

26 when $r_h = 3.97$ au, ultimately spanning $\Delta r_h = 4.63$ au over 18 months. A reciprocal semi-major axis of $1/a_0 = 1.5 \times 10^{-5}$ au^{-1} suggests this comet is dynamically new.

The overall shape of the secular light curve is best fit with a second-order polynomial, indicative of a more gradual transition between different rates of brightening. However, for the sake of comparison, we separate the light curve into three different sections and determine the best-fit activity index for each section. Using this method we determine that from $r_h \sim 8.5$–4.0, the rate of activity increase lessens from $n = 6.2 \pm 0.3$ to $n = 2.3 \pm 0.1$ (Figure 3.17). The $g - r$ color did not change throughout our observations and remained $g - r = 0.56 \pm 0.03$.

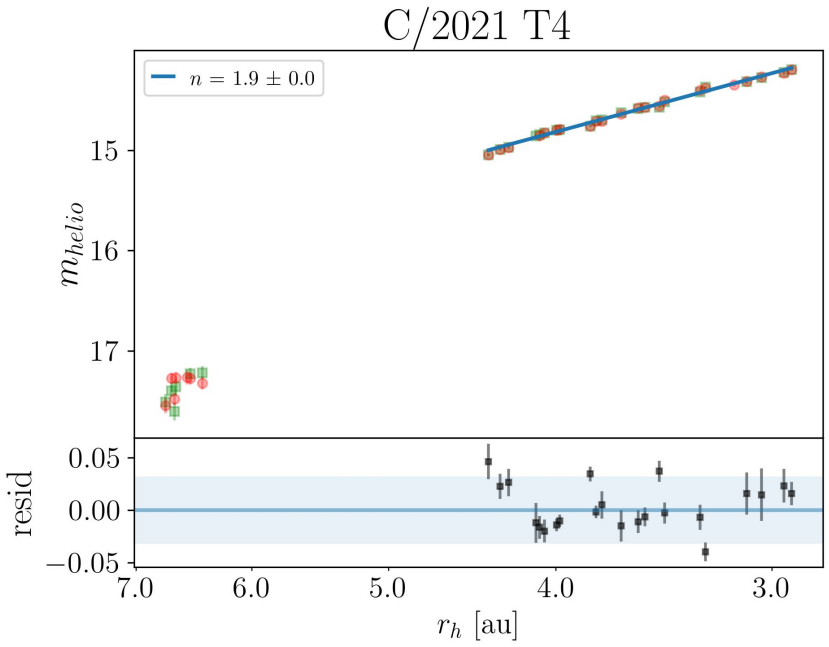

Figure 3.18: Same as Figure 3.5 for C/2021 T4 (Lemmon) using $g - r = 0.50 \pm 0.04$. Only pre-perihelion data are shown.

3.5.12 C/2021 T4 (Lemmon)

Comet C/2021 T4 was discovered by the Mt. Lemmon survey 2021 Oct 07 with $m_{app} = 20.2$ in the G filter and $r_h = 7.17$ au (MPEC 2021-U187). The LOOK project has been observing this comet since 2021 Nov 08 when $r_h = 6.90$ au until 2023 Jan 19 when $r_h = 2.92$ au. C/2021 T4 will reach perihelion at $q = 1.48$ au on 2023 Jul 31 while also closely approaching Earth with $\Delta \sim 0.5$ au. The proximity and brightness of the comet will enable observing opportunities that are not usually possible, inspiring us to conduct dedicated observations in June and July 2023 using the 4.1-m SOAR Telescope (not reported here). C/2021 T4 has a reciprocal semi-major axis of 3.2×10^{-5} au^{-1}. As discussed in Section 1.4, dynamical simulations by Dybczyński & Królikowska (2015) suggest that a comet with $1/a_0$ between 3×10^{-5} and 4×10^{-5} is only slightly more likely

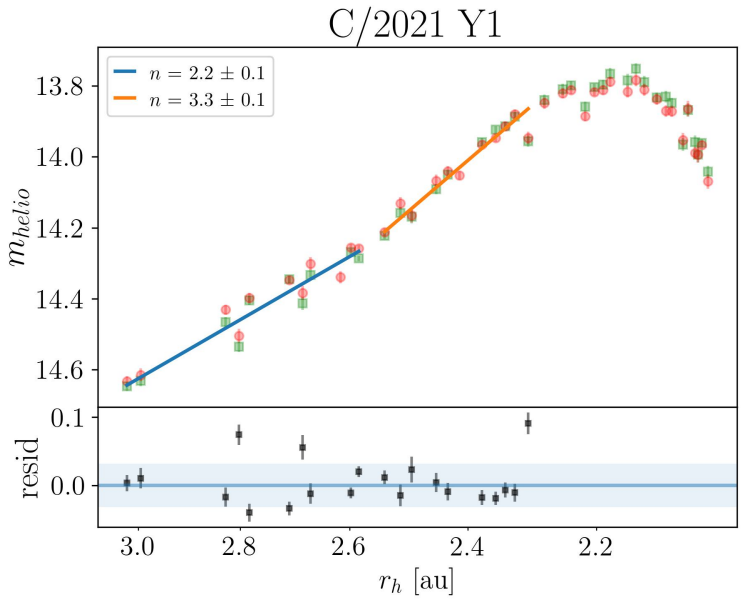

Figure 3.19: Same as Figure 3.5 for C/2021 Y1 (ATLAS) using $g - r = 0.47 \pm 0.02$. Only pre-perihelion data are shown.

to be dynamically new ($\sim$ 40% compared to $\sim$ 25% for returning and $\sim$ 35% uncertain). Near-Earth observations of the coma morphology could shed light on the dynamical history of this object.

Initial observations are near the limiting magnitude of the telescopes, but the increase in brightness observed when $r_h = 4.5$ au would require $n = 5.2$. The activity index then decreased to $n = 1.9 \pm 0.1$ and $Af\rho$ values have remained constant near 800 cm ever since (Figure 3.18). A constant color of $g - r = 0.50 \pm 0.04$ was observed.

3.5.13 C/2021 Y1 (ATLAS)

The ATLAS survey discovered comet C/2021 Y1 2021 Dec 26 with $r_h = 5.52$ au and an apparent magnitude of 18.9 in the orange filter (MPEC 2022-A50). The LOOK project began observing this comet 2022 Jan 07 with $r_h = 5.42$ au. However, the seeing for several of the early observations was larger than the required 4", so our analysis begins

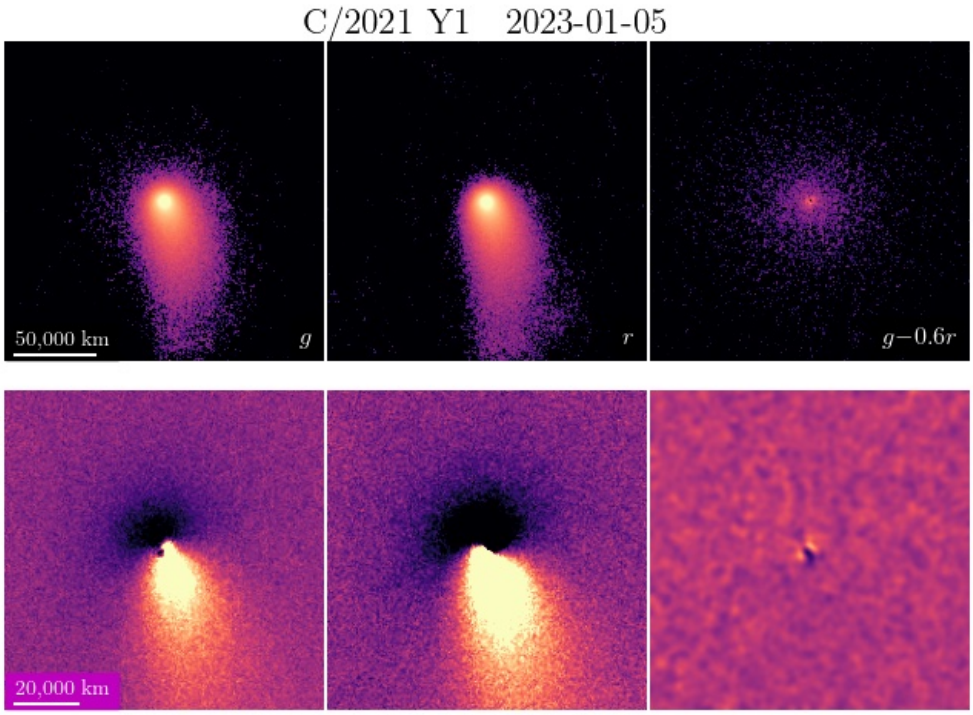

Figure 3.20: Same as Figure 3.14 for median-combined images of C/2021 Y1 (ATLAS) from January 2023. The synthetic "gas" image in the upper right panel appears symmetric and the enhanced image in the bottom right panel shows no distinct features, suggesting the comet is experiencing isotropic outgassing.

when $r_h = 3.0$ au. Observations continued through 2023 Mar 31 with $r_h = 2.0$ au, where we make the cutoff for this chapter.

After C/2021 Y1 had its closest approach to Earth with $\Delta = 1.67$ au and $r_h = 2.62$ au, its brightness increased as $n = 3.3 \pm 0.1$, followed by a decrease in brightness starting at $r_h = 2.2$ au (Figure 3.19), which continued until the latest observations. A decrease in color occured after closest approach from $g - r = 0.50 \pm 0.02$ to $g - r = 0.45 \pm 01$. Enhancement of the synthetic gas image reveals the gas production is isotropic (Figure 3.20), suggesting C/2021 Y1 is dynamically new. Therefore, the decrease in brightness could very well be due to the depletion of surface-level volatiles, but further observations are needed to make further conclusions.

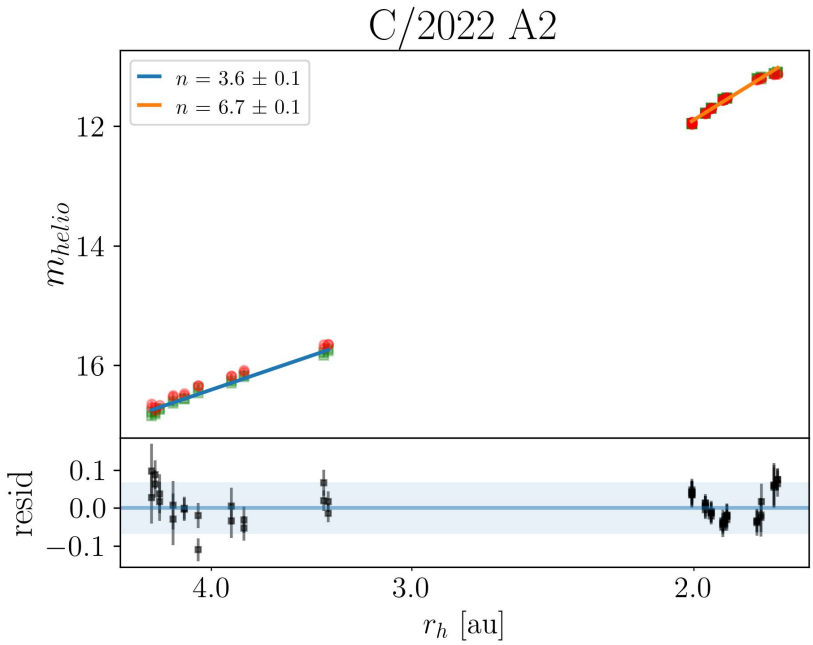

Figure 3.21: Same as Figure 3.5 for C/2022 A2 (PANSTARRS) using $g - r = 0.50 \pm 0.08$. Only pre-perihelion data are shown.

3.5.14 C/2022 A2 (PANSTARRS)

Comet C/2022 A2 (PANSTARRS) was discovered 2022 Jan 10 by PANSTARRS when the comet had a heliocentric distance $r_h = 4.87$ au and a magnitude of 20.5 in the w filter (MPEC 2022-C01). The LOOK project has been observing this comet since 2022 Mar 02 with $r_h = 4.41$ au until the most recent observations 2023 Jan 23 with $r_h = 1.77$ au. C/2022 A2 passed perihelion at $q = 1.73$ au on 2023 Feb 18 but was not observable again until June 2023. The data obtained since then is not included in this chapter.

Initial observations of C/2022 A2 showed an activity index of $n = 3.6 \pm 0.1$ and $g - r = 0.50 \pm 0.05$. Sometime between ∼2–3.5 au, the activity began a steep increase of $n = 6.7 \pm 0.1$ (Figure 3.21). The rate of increase may be decreasing towards the end of observations, but there is not enough heliocentric distance coverage to confidently identify

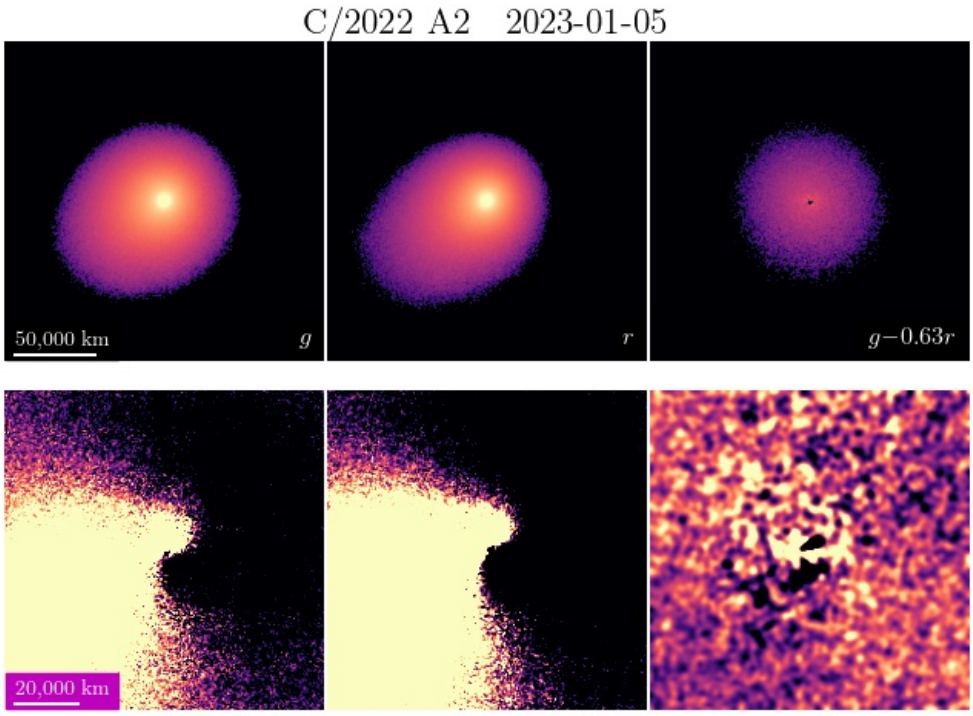

Figure 3.22: Same as Figure 3.14 for median-combined images of C/2022 A2 (PANSTARRS) from January 2023. The enhanced synthetic "gas" image shows faint wide fan-like features near position angle 40° and 220°, perpendicular to the darker regions.

a break. During the activity increase, the $g-r$ color decreased from $g-r = 0.43 \pm 0.03$ to $g-r = 0.38 \pm 0.03$. The synthetic gas image shows signs of faint asymmetry in the coma (Figure 3.22), suggesting C/2022 A2 may have experienced prior heating.

3.5.15 C/2022 A3 (ATLAS)

Long-period comet C/2022 A3 (Lemmon – ATLAS) was discovered 2022 Jan 10 by the Mt. Lemmon Survey when the comet had a heliocentric distance $r_h = 6.42$ and a magnitude of 20.3 in the G filter (MPEC 2022-E107). The discovery was confirmed by the ATLAS survey 2022 Mar 01 with $r_h = 6.11$ and a magnitude of 19.2. LOOK has been observing C/2022 A3 since 2022 Mar 02 ($r_h = 4.31$ au) through perihelion at $q = 1.73$ au

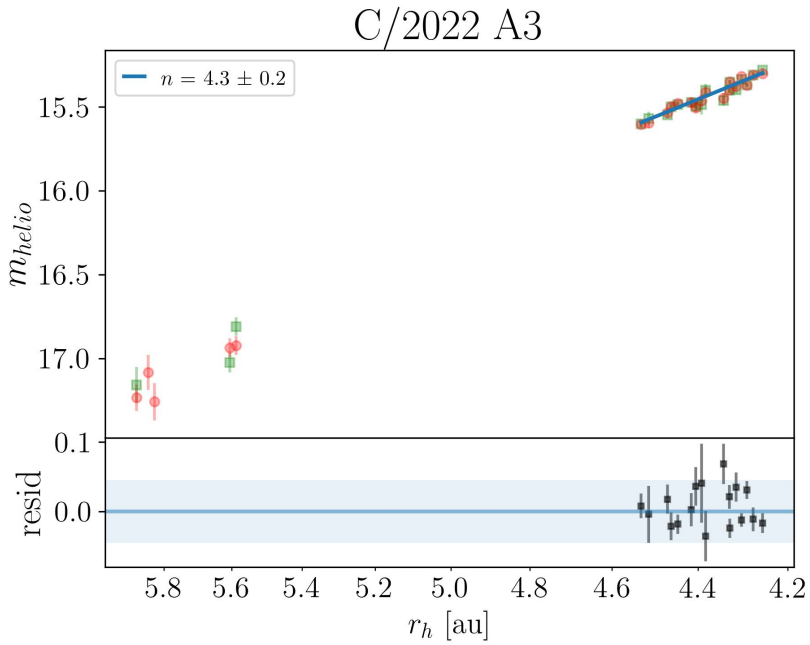

Figure 3.23: Same as Figure 3.5 for C/2022 A3 (ATLAS) using $g - r = 0.51 \pm 0.04$. Only pre-perihelion data are shown.

on 2023 Feb 18 until the most recent observations with $r_h = 4.06$ au on 2023 Mar 25. C/2022 A3 is a returning comet outside of the Oort spike with a reciprocal semi-major axis of $1/a_0 = 1.153 \times 10^{-3}$ au^{-1}.

Our first images of comet C/2022 A3 were near the limiting magnitude for detection with large uncertainties. Our later observations beginning 4.6 au from the Sun show an increase in activity as $n = 4.3 \pm 0.2$ (Figure 3.23). Modeling the increase in activity from the earlier observations results in a $n = 5.3 \pm 0.1$ with a $\chi^2 > 50$, so we only use the later observations as our only activity index for comparison to other comets. A color of $g - r = 0.51 \pm 0.04$ was consistent for all observations.

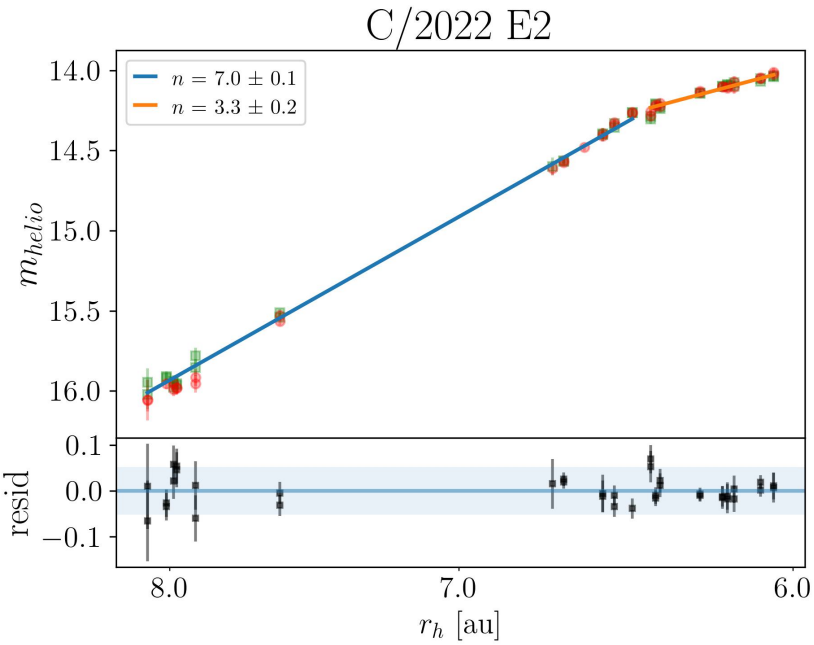

Figure 3.24: Same as Figure 3.5 for C/2022 E2 (ATLAS) using $g - r = 0.48 \pm 0.02$. Only pre-perihelion data are shown.

3.5.16 C/2022 E2 (ATLAS)

Comet C/2022 E2 was discovered 2022 Mar 07 by ATLAS when the comet had a heliocentric distance of $r_h = 8.30$ au and a magnitude of 18.7 in the cyan filter (Denneau et al., 2022). LOOK began monitoring the comet 2022 Apr 04 with $r_h = 8.14$ au and continued observations until the most recent visit on 2023 Mar 23 at $r_h = 5.88$ au. The reciprocal of the original semi-major axis is $1/a_0 = 7.1 \times 10^{-5}$ au^{-1} and while this characterizes C/2022 E3 as part of the "Oort spike", dynamical models suggest it is most likely a returning comet (Dybczyński & Królikowska, 2015).

Comet C/2022 E2 had an activity index of $n = 7.0 \pm 0.1$ until a break in activity occured around $r_h \sim 6.5$ au and the activity index flattened to $n = 3.3 \pm 0.2$ (Figure 3.24). The comet maintained $g - r = 0.48 \pm 0.02$ throughout observations.

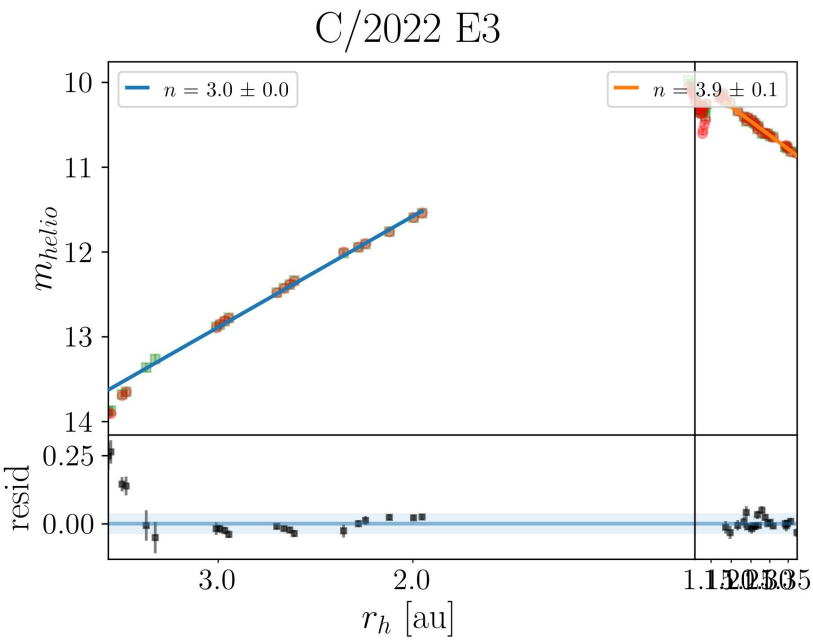

Figure 3.25: Same as Figure 3.5 for C/2022 E3 (ZTF) using $g - r = 0.51 \pm 0.04$. The dip observed post-perihelion is due to the small size of the aperture not containing most of the coma.

3.5.17 C/2022 E3 (ZTF)

Comet C/2022 E3 (ZTF) was discovered by the Zwicky Transient Survey (ZTF) 2022 Mar 02 with a heliocentric distance of $r_h = 4.27$ au and magnitude of 17.2 with the r filter (Bolin et al., 2022). LOOK began observing C/2022 E3 2022 Mar 22 when the comet had a heliocentric distance $r_h = 4.07$ au through perihelion at $q = 1.11$ au on 2023 Jan 12 until the most recent observations near the end of 2023 March with $r_h = 1.71$ au. Observations span a range of $\Delta r_h = 3.56$ au and ~ 1 yr. C/2022 E3 has a reciprocal semi-major axis of $1/a_0 = 7.13 \times 10^{-4}$ au^{-1}, which is outside of the "Oort spike" and suggests it is a returning comet.

C/2022 E3 was one of the brightest comets in our sample, reaching an apparent magnitude of less than 10 in the r-band during its closest approach to Earth with a minimum

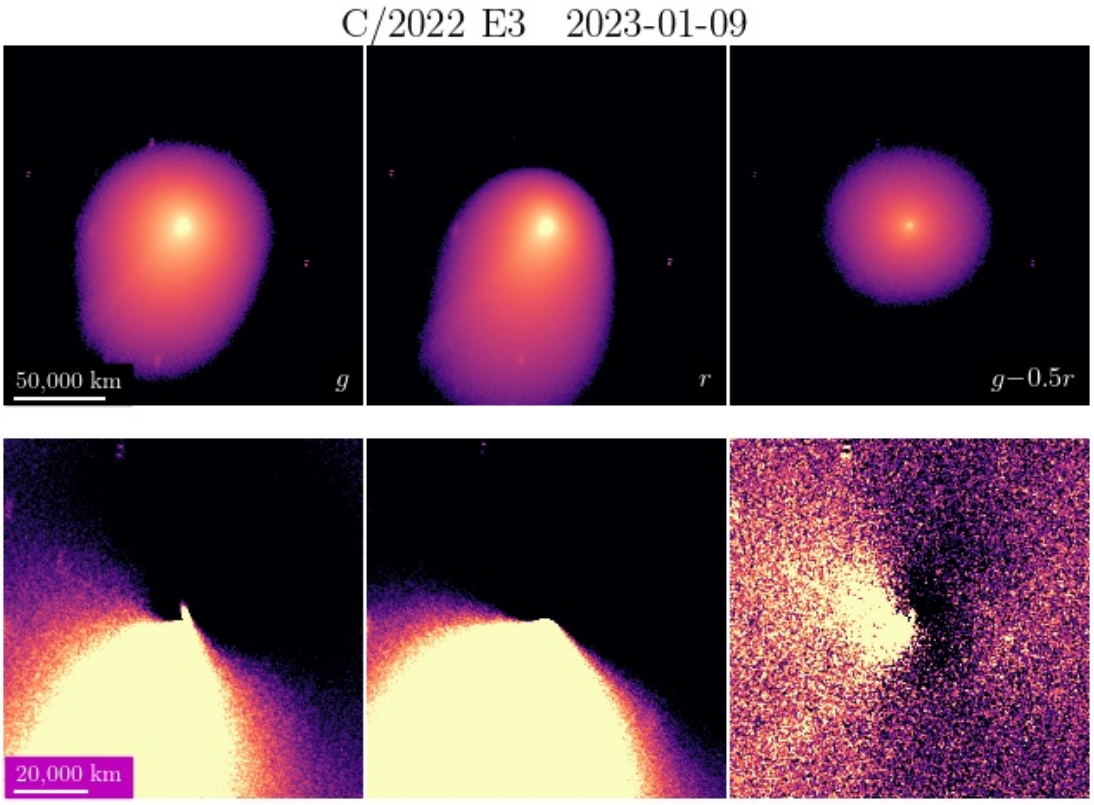

Figure 3.26: Same as Figure 3.11 for median-combined images of C/2022 E3 (ZTF) from 2023 January 9. The enhanced synthetic "gas" image shows structure in the coma the left of the image, including what we know to be an ion tail at position angle ∼130°. A more faint fan of gas can be seen to the right of the image.

geocentric distance of $\Delta \sim 0.28$ au. It was observed by many observatories including JWST (Milam et al., 2023). We obtained time at Lowell Observatory and measured a rotation period of 8.7 ± 0.1 hr using coma morphology (Knight et al., 2023a). This method can only be achieved if a comet is in close proximity to Earth, which is why C/2022 E3 is only the 13th long-period comet with a measured rotation period (Knight et al., 2023c).

During initial observations, C/2022 E3 had a color of $g - r = 0.54 \pm 0.03$, which decreased to $g-r = 0.30 \pm 0.04$ near perihelion. The heliocentric magnitude m_{helio} increased with $n = 6.0 \pm 0.6$ until around 3 au when the rate decreased to $n = 3.0 \pm 0.1$ (Figure 3.25). During its close approach to Earth, the comet took up most of the FOV and our

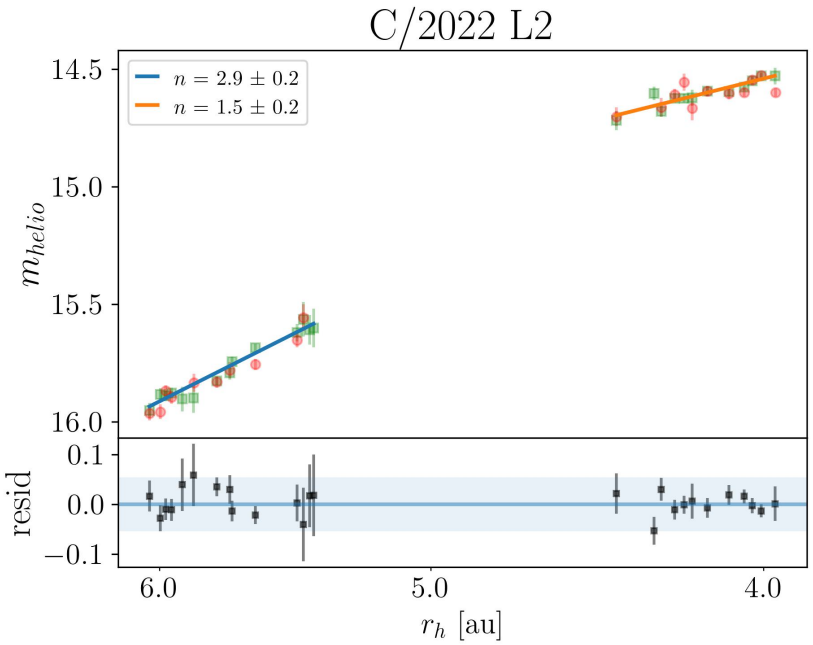

Figure 3.27: Same as Figure 3.5 for C/2022 L2 (ATLAS) using $g - r = 0.52 \pm 0.03$. Only pre-perihelion data are shown.

small aperture size did not capture the full brightness, which is why a dip in brightness is observed post-perihelion, followed by a decrease in brightness as $n = 3.9 \pm 0.1$. The synthetic gas image shows asymmetries in the gas production and what we know (from our Lowell observatory observations) to be an ion tail at position angle $\sim 130°$ (Figure 3.26).

3.5.18 C/2022 L2 (ATLAS)

Comet C/2022 L2 (ATLAS) was discovered 2022 June 10 by the ATLAS Survey when $r_h = 6.54$ au with an apparent magnitude of 18.4 in the orange filter (Fitzsimmons et al., 2022). The LOOK Project began observing C/2022 L2 on 2022 July 06 when $r_h = 6.36$ au until the most recent observations 2023 May 28 when $r_h = 3.97$ au. A reciprocal original semi-major axis of -1.2×10^{-5} au^{-1} suggests this comet is dynamically new.

C/2022 L2 was observed to increase in brightness as $n = 2.9 \pm 0.2$ until sometime

between $r_h = 5.4$ to 4.5 au, when the rate decreased to $n = 1.5 \pm 0.2$ (Figure 3.27), suggesting a decrease in intrinsic brightness. Further observations are necessary to discern if the decrease is a lasting trend or the remnant effects of an outburst. A constant color of $g - r = 0.52 \pm 0.03$ was observed.

3.6 Sample Comparison

3.6.1 Activity

Most of the sample experienced a range of activity indices over their observation period. However, all were between $n = 1$ and $n = 8$, which is consistent with previous studies (Meech & Svoren, 2004). The rate of activity is observed to decrease with decreasing heliocentric distance (Figure 3.28). This is true for individual objects and when considering the entire sample. Two objects that do not fall into this trend are C/2019 L3 and C/2022 A2, which experience a "surge" in brightness near perihelion.

When we compare the overall pre-perihelion activity indices (i.e., without any breaks) of the sample, we find that "new" and returning comets have different n distributions (Figure 3.29). Returning comets exhibit an overall steeper increase in activity (though a broad distribution) around $n \sim 5$, whereas "new" comets have a more shallow increase around $n \sim 3$. These values are higher than the usually associated values of $n = 2$ for "new" comets and $n = 4$ for returning comets (Meech & Svoren, 2004), though we still find a difference of 2 between "new" and old n values. The discrepancy could be due to our more distant observations and so the trend described in the above paragraph would affect the average rate of brightening. It is also important to note that our sample size is very small, with

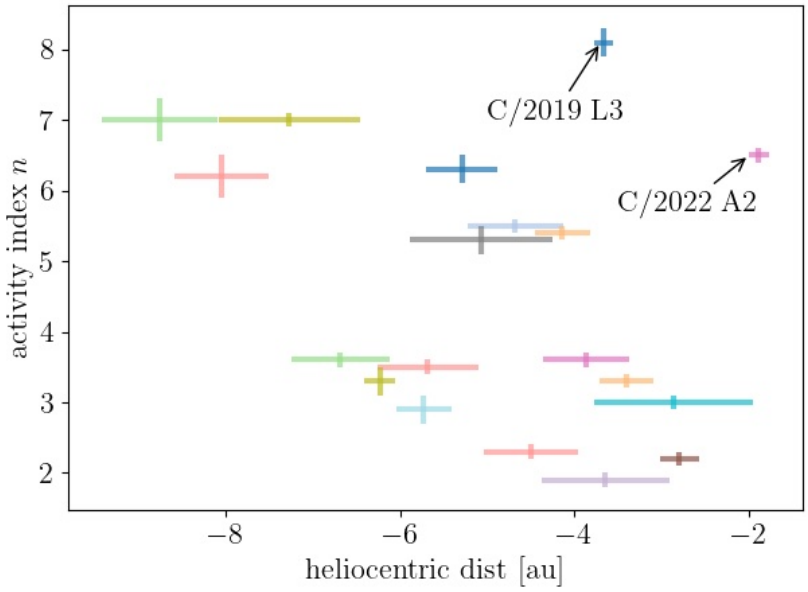

Figure 3.28: The activity indices for the sample vs heliocentric distance, where each color is an individual comet with multiple n values. The error values show the range of heliocentric distance and the 1σ error on the activity index. The rate of activity is observed to decrease with decreasing heliocentric distance for individual comets and the entire sample. Two objects that do not fall into this trend are C/2019 L3 and C/2022 A2, which experience a "surge" in brightness near perihelion.

only three returning comets and seven "new" comets in Figure 3.29. We remove the two comets that experience a surge during perihelion increasing their pre-perihelion activity index.

The $A(0°)f\rho$ values for the entire sample range over two orders of magnitude throughout observations (Figure 3.30). We see no trend with heliocentric distance except that more distant discoveries have higher $A(0°)f\rho$ values to start. Such a trend is expected as more active targets are brighter and can be discovered at greater distances than less active or smaller comets. We also find no clear trend with $1/a_0$.

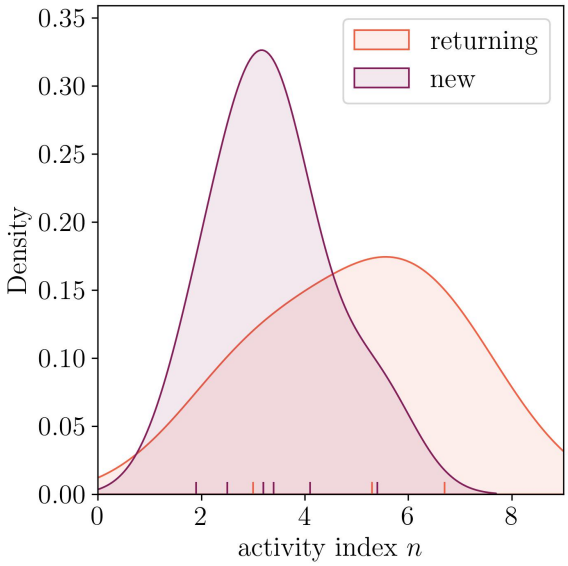

Figure 3.29: A kernel density plot (KDE) showing the color distribution of the overall pre-perihelion activity indices for "new" (red) versus returning (blue) comets using a threshold of $1/a_0 = 4.0 \times 10^{-5}$ au^{-1}. The value for each comet is shown as a small line below the KDE. Returning comets exhibit an overall steeper increase in activity around $n \sim 5$, whereas "new" comets have a more shallow increase around $n \sim 3$.

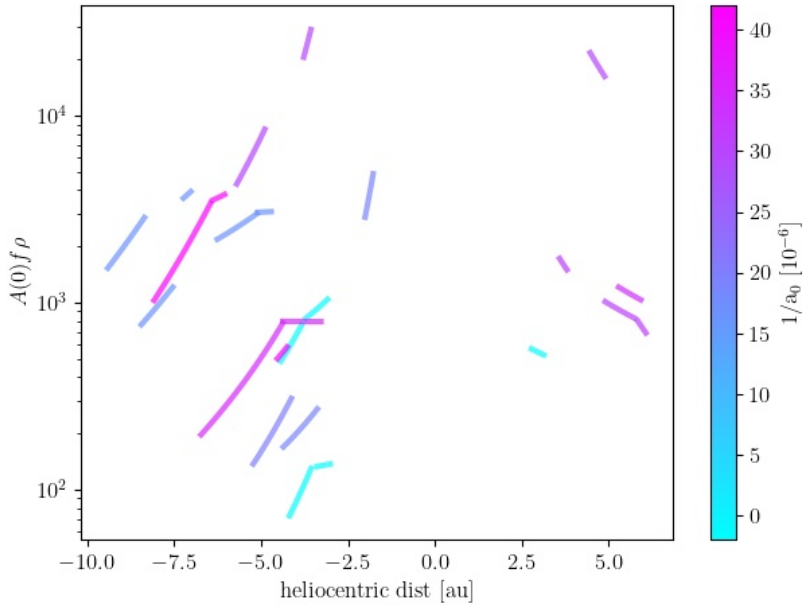

Figure 3.30: $A(0°)f\rho$ (an aperture-independent quantity used as an estimator for dust production) versus heliocentric distance, where the line(s) for each comet is colored according to its $1/a_0$ value. We find no clear trend with $1/a_0$ or r_h.

3.6.2 Colors

The average color of the sample is $g - r = 0.50 \pm 0.03$, which is consistent with other active LPCs (Jewitt, 2015). We find no significant difference between new and returning comets (Figure 3.31). We also observe no trends with heliocentric distance until comets reach $r_h \lesssim 2.5$ au.

A color-change was observed in six objects in our sample (Figure 3.32). Most of them exhibited a bluer color during perihelion, which is expected as gas emission increases in the g-band relative to the r-band. However, one comet, C/2019 F1, showed a redder color during perihelion, while also experiencing a "surge" in brightness, potentially due to an increase in larger dust particles, which scatter in proportion to their physical cross-section (Kolokolova et al., 2004). We assess the heliocentric distance where a bluer color-change occurs for all objects and found that the two returning comets, C/2021 A1 and C/2022 E3, changed color closer to the Sun ($r_h < 1.5$ au) compared to "new" comets. The three "new" comets that changed color, did so around $r_h \sim 2.5$ au and followed the same color vs r_h trend (Figure 3.33). However, no "new" comet with a heliocentric distance less than $\sim$1.5 au was observed.

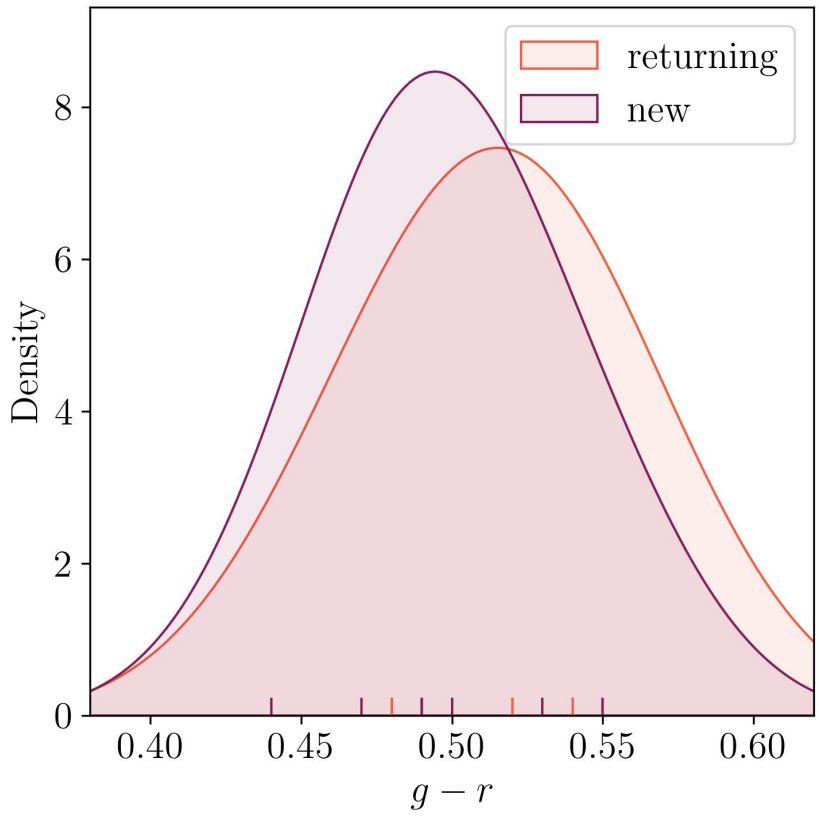

Figure 3.31: A KDE plot showing the color distribution of "new" (purple) versus returning (orange) comets using a threshold of $1/a_0 = 4.0 \times 10^{-5}$ au^{-1}. Each comet is plotted as a gaussian with $\sigma = 0.05$. The value for each comet is shown as a small line below the KDE. There is no significant difference in color where "new" comets exhibit an average color $g - r = 0.50 \pm 0.03$ and returning comets with $g - r = 0.51 \pm 0.03$.

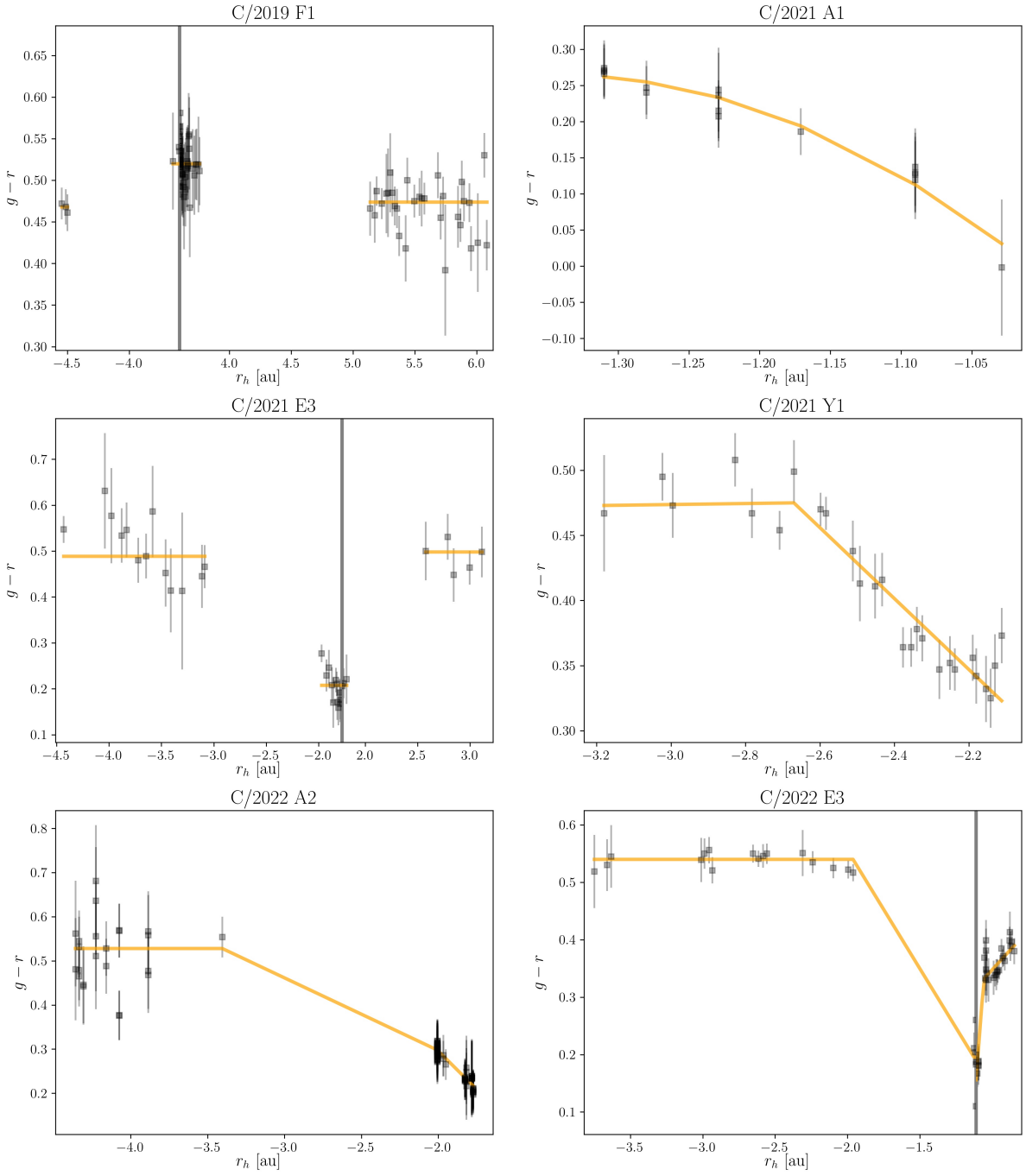

Figure 3.32: Comets in our sample that experienced a change in $g - r$ color. We use a 20,000 km aperture. Most exhibit a bluer color with $r_h \leq 2.5$ au, except for C/2019 F1, which becomes redder during perihelion $q = 3.6$ au.

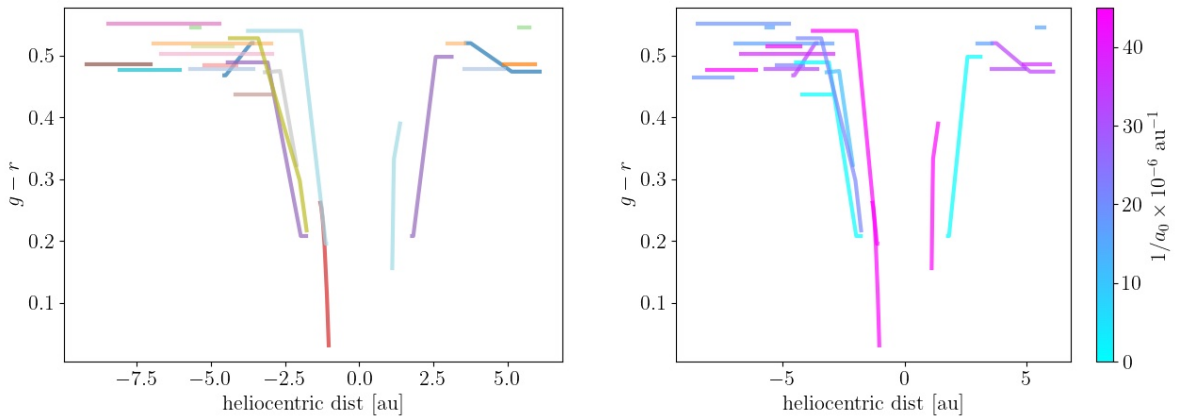

Figure 3.33: The evolution of $g - r$ color with heliocentric distance. The data is the same except for the color of the lines. The **left** figure has multiple colors, where each color represents data from a single comet. The **right** figure is colored according to $1/a_0$. Since most of our sample are likely dynamically new with $1/a_0 \times 10^6 < 40$ au^{-1}, only the bright pink are "returning comets". The comets that change to a bluer color do so within 2.5 au from the Sun. Returning comets become bluer within 1.5 au from the Sun, suggesting that the volatile ices in returning comets are more deeply buried.

3.6.3 Morphology

We assessed the coma morphology of the five comets that exhibited a $g - r$ color decrease within 3 au of the Sun (Figure 3.32) since this implied that they had enough gas production to probe coma morphology with a synthetic gas image (as described in Section 3.4.3). Two comets displayed clear jets in the enhanced images: C/2021 A1 Leonard (Figure 3.11) and C/2022 E3 ZTF (Figure 3.26). They were the only comets observed within 1 au of Earth and the only comets of the five with $1/a_0$ values outside of the Oort spike, suggesting they are dynamically new.

Faint asymmetries in the coma can be seen in the enhanced synthetic gas images of comets C/2021 E3 ZTF (Figure 3.14) and C/2022 A2 (Figure 3.22), which were observed with heliocentric distances less than 2 au and geocentric distances beyond 1 au. C/2021 Y1 (ATLAS) was the most distant observation of the five with a geocentric distance $\Delta \sim 2.4$ au. No structure in the coma is detected from the enhanced synthetic gas image, which could be due to isotropic outgassing. We discuss this idea further in Section 3.7.3. All three of these comets have $1/a_0$ values that indicate they are dynamically new.

When creating a synthetic gas image (described in detail in Section 3.4.3), we scaled a "dust" r image before subtracting it from the g image. We can use that scale to roughly approximate dust color. For our sample of five comets, we found that four of them had dust colors $g - r \sim 0.50$ to 0.55, which is within 2σ of the mean $g - r$ colors of the entire LOOK sample. The exception is C/2022 E3 (ZTF), which had a "dust color" of $g - r = 0.75$.

3.7 Discussion

3.7.1 Heliocentric Distance Effects on Brightening Rates

As discussed in Section 1.4, dynamically new comets have been observed to be 1) more active (e.g., Sárneczky et al., 2016) and 2) have a more shallow increase in brightness compared to returning comets (e.g., Whipple, 1978). These trends inspired the idea that dynamically new comets may rapidly brighten at large heliocentric distances and brighten more slowly near perihelion (e.g., Oort & Schmidt, 1951; Whipple, 1978). However, those studies were based on observations with $r_h \lesssim 3$ and therefore, did not include the rapid brightening phase of the light curve. Our study provides evidence for the hypothesized distant brightening phase.

We found that the rate of brightening decreases with heliocentric distance for all long-period comets. Certain comets in our study displayed a gradual decline in the activity index (e.g., C/2021 S1, C/2021 G2), indicating the presence of a continuous mechanism or a series of mechanisms dominating their activity. On the other hand, other comets exhibited discontinuous steps in the activity index (e.g., C/2021 F1, C/2022 E2), indicating the sudden initiation of a separate activity mechanism. Suggested drivers of the distant rapid brightening include the sublimation of a "frosting" of highly volatile material from irradiation by galactic cosmic rays while in the Oort Cloud (Whipple, 1978; Johnson et al., 1987) and/or the sublimation of ices more volatile than water (i.e., CO, CO_2; Meech & Svoren, 2004).

In addition to LOOK observations, we have been monitoring 8 newly discovered

LPCs that are inbound beyond 10 au from the Sun using the 4.1-m SOAR telescope in Chile on roughly monthly timescales starting February 2021. Analysis of the time-series photometry of these comets will provide insight into how far from the Sun the brightening rate vs heliocentric distance trend hold, further constraining the responsible mechanisms.

Previous studies have reported that DNCs have a more shallow brightening rate pre-perihelion than post-perihelion compared to returning comets (e.g., Whipple, 1978; A'Hearn et al., 1995). Our observations show that only observations within 3 au of the Sun (where H_2O sublimation dominates and most of the observations from previous studies occurred) exhibit an activity index $n \sim 2$ that then increases to $n \sim 4$ post-perihelion, agreeing with the past studies (e.g., C/2021 E3, C/2022 E3). A dust mantle created during peak water-ice sublimation could cause a steeper decrease in activity by decreasing the percentage of active area on the surface (e.g., Whipple, 1978; A'Hearn et al., 1995). However, LPCs with $q > 3$ au have higher activity indices pre-perihelion (e.g., C/2019 F1, C/2019 L3). These objects may not experience enough water-ice sublimation to form a dust mantle. Our results are still consistent with prior studies, because those observations occurred when objects were less than 3 au from the Sun.

3.7.2 Drivers of Sudden Brightness Decrease

Three comets in our sample experienced a decrease in apparent brightness pre-perihelion: C/2021 A1, C/2020 R7, and C/2021 Y1. Such trends could be caused by seasonal effects where the position of the rotational pole causes an active region on the comet to no longer be insolated by the Sun. Other possibilities include a decrease in activity due to the deple-

tion of volatiles. For C/2020 R7, the rapid decrease was seen to return to a steady activity index post-perihelion, suggesting seasonal effects are responsible for the change in activity. However, C/2021 Y1 continued to decrease through perihelion at a constant rate with time. Further observations are required to understand if this decrease is truly a depletion of volatiles since the comet has only recently passed perihelion.

3.7.3 Dynamically New vs Returning Comets

Studies have previously reported $n \sim 2$ for dynamically new comets and $n \sim 4$ for returning comets, suggesting that DNCs have a larger fractional active surface area ($\sim 100\%$) than returning comets. However, our sample shows DNCs have an overall pre-perihelion $n \sim 3$ and returning comets have a wider spread with $n \sim 5.5$ (Figure 3.29). While the overall difference of $\Delta n \sim 2$ is the same, this discrepancy could be due to the heliocentric distance range of our observations. Activity indices are larger further from the Sun (Figure 3.28) and most of our observations are further from the Sun causing our overall mean to be higher, whereas previous studies conducted all observations with $r_h \leq 5$ au.

If we assume dynamically new comets have yet to build up a dust mantle before their first solar passage, then we would expect the surface to be uniformly active. Therefore, any fractional active area less than 100% would imply a previous solar passage. Active areas would present themselves in the form of jets or seasonal effects (i.e., pre-perihelion peak). However, the shape of the comet nucleus can affect the heterogeneity of the coma (e.g., a shadowed region). DNCs have been known to have a larger fractional active area than returning comets (e.g., A'Hearn et al., 1995). The presence of asymmetries in the

coma morphology and pre-perihelion peaks in activity may not be as closely related to the dynamical age as we once thought.

Five comets in our sample reach a heliocentric distance of less than 2.5 au and all experience a decrease in $g-r$ color (Figure 3.33). Because the g-band contains gas emission lines and the r-band is mostly depleted of such lines, a bluer color suggests a change in gas production, which is expected to increase as water-ice sublimation "turns-on" during a comets approach to the Sun. The three comets that are predicted to be dynamically new all change colors near $r_h \sim 2.5$ au and at similar rates, whereas the returning comets change colors closer to the Sun. Our results suggest that returning comets have more deeply buried volatiles after depleting the upper layers on a previous solar passage, and therefore require solar radiation to penetrate further into the nucleus to cause water-ice sublimation, resulting in a rapid increasing in activity closer to the Sun for returning comets compared to dynamically new comets.

3.7.4 Predicting Brightness Behavior

The methods for predicting brightness today involve fitting a constant rate of activity increase as more data points are added. Our work suggests that a more dynamic prediction model where the activity index changes over heliocentric distance would be more accurate. The degree of the change in the brightening rate may be related to dynamical age if we continue the assumption that DNCs have more hypervolatiles and larger active areas. However, we do not have enough objects or heliocentric distance coverage to thoroughly investigate at this time.

3.8 Summary

Since August 2020, we have used LCO's network of 1-m telescopes and SDSS g and r filters to create a frequent and long-term dataset, which we used to characterize the brightness evolution, colors, and coma morphology of distant long-period comets. We found:

1. The brightening rates decreased with decreasing heliocentric distance for all long-period comets. Observations of the rapid brightening portion of the light curve will help constrain the potential mechanisms for activity.

2. When predicting future magnitude estimates, we should consider including a dynamic model where the brightening rate decreases with heliocentric distance compared to the constant value used today.

3. Comets with $r_h < 3$ au exhibit a color change suggesting an increase in gas production driven by water-ice sublimation.

4. Returning LPCs experience a surge in gas production closer to the Sun compared to returning comets suggesting volatiles are more deeply buried. The upper layers of the surface may have been depleted on a previous solar passage.

5. We created synthetic gas images by subtracting a scaled r image from a g image. Some of our objects have very faint asymmetries in the coma, which could indicate that the surface is not as pristine as previously thought. The method can potentially be used to assess gas morphology when narrowband filters (e.g., Farnham et al., 2000)

are not accessible, but further study is needed.

6. The addition of more distant comets from the upcoming LSST and the continuation of LOOK will enable better characterization of the population.

Chapter 4: Comparing the Dynamical History and Brightness Behavior of LPCs Using Amateur Photometry

4.1 Introduction

Past evolutionary studies of long-period comets (e.g., Chapter 3 and studies discussed in Section 1.4.2 have used mostly self-consistent data, collected by the authors (e.g., A'Hearn et al., 1995) and/or using the survey data from the same telescope (e.g., Gardener et al., 2023). Photometric observations of long-period comets from amateur astronomers provide long-term, frequent collections of data but have largely been underutilized by the professional community. One of the greatest assets of amateur observers lies in their extensive network of telescopes, which collectively span the globe. This distributed infrastructure greatly enhances the coverage and efficiency of comet observations. By collaborating with amateurs worldwide, professional astronomers can gather data from different geographical locations, thereby overcoming limitations posed by local weather conditions and time zone constraints. And unlike professionals who often focus on specific projects, amateur observers have the flexibility to dedicate significant time to the long-term monitoring of comets. The ability to capture frequent observations during a comet's apparition allows for the construction of detailed light curves, providing insights into the object's brightness

variations and activity levels (Figure 4.1). Previous studies have incorporated amateur observations from databases (e.g., Meech et al., 2017b; Sekanina & Kracht, 2018; Womack et al., 2021), and others have solicited amateur observations directly (e.g., Samarasinha et al., 2015; Snodgrass et al., 2017). Analysis of the methods used by professional/amateur collaborations and recommendations for the future have been discussed in the past few decades (e.g., Kidger, 2002; Boyd, 2011; Mousis et al., 2014). However, their work mainly focuses on the reporting of visual magnitudes.

Previous studies comparing observations of brightness behavior with dynamical age solely use $1/a_0$ value as a proxy. $1/a_0$ is typically determined by tracing the motion of the comet backward through the planets, taking into account gravitational perturbations, relativistic effects, and non-gravitational forces up to the heliocentric distance where such perturbations can be neglected ($\sim$250 au). However, some models do not account for non-gravitational forces (see Section 1.4.1). M. Królikowska and P. A. Dybczyński have dedicated decades of research to the dynamical modeling of long-period comets (e.g., Królikowska & Dybczyński, 2010, 2013; Dybczyński & Królikowska, 2015; Królikowska & Dybczyński, 2017). In Królikowska (2020), they presented a new cometary catalog containing extensive orbital information for nearly 300 comets discovered before 2018 with orbits within the "Oort Spike", including the previous perihelion distance. Their methods include rigorous data selection and weighting, multiple non-gravitational acceleration parameters, and the incorporation of Galactic and stellar perturbations (Królikowska, 2020, discussed in-depth in Section 4.4).

In this chapter, we assess how the dynamical history of a comet affects brightness behavior by comparing the long-term photometric measurements from amateur observers

to orbital parameters derived from robust dynamical models that include nongravitational accelerations, galactic tides, and stellar perturbations. The model requires long-term astrometric measurements, so such parameters cannot be determined with the newly acquired data presented in Chapter 3 within the timescale of a thesis. We aim to identify any trends in observable properties that relate to dynamical age to allow for better predictions of brightness behavior of future discoveries and/or to discern dynamical age using brightness behavior. In Section 4.2 we attempt to create a methodology for synthesizing CCD photometric magnitudes submitted by amateur observers. In Section 4.3, after applying the methodology from 4.2 to the CCD data and from Womack et al. (2021) to the visual data for the comets in our sample, we analyze their brightening rates versus heliocentric distances. Finally, in Section 4.5, we compare the observational results to orbital properties from the extensive models by M. Królikowska and P. A. Dybczyński. We discuss the implications of our findings in Section 4.6 and provide a summary and future outlook in Section 4.7.

4.2 Synthesizing Amateur Data

For our study, we are using reported magnitudes made publicly available by individual observers using their own instrument setups and reduction pipelines. While this is extremely valuable to the professional community, it comes with challenges in comparison to data collected by individual researchers as was done in Chapter 3. Below, we will describe the observed inconsistencies and explain our process for synthesizing the data so it can be used for our analysis.

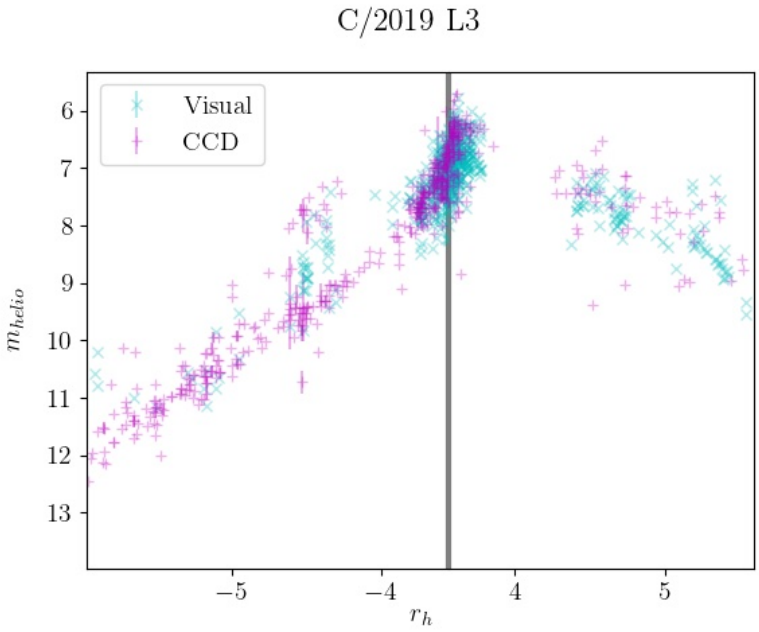

Figure 4.1: An example of the scatter present in submitted observations of comet C/2019 L3, where the blue points are visual observations and the pink are CCD observations. A negative r_h is representative of data collected pre-perihelion.

4.2.1 Inconsistencies Between Observers

Visual magnitude estimations have a historical record spanning a century, making them the longest-standing source of comet data after astrometry (see review in Larson et al., 1991). The method of obtaining a visual magnitude estimate consists of an observer visually comparing the brightness of the comet to a nearby reference star. The International Comet Quarterly (ICQ) archive (Green et al., 1986) has compiled a significant portion of these visual magnitude estimations. However, it is important to note that visual observations of comets are inherently subjective, influenced by factors such as human perception, memory biases, recall biases, and the lack of standardized procedures. These elements contribute to variations and subjective interpretations within the observations. CCD observations are inherently more objective by using photon counts to determine the

apparent magnitude, but this method only recently experienced widespread adoption in the professional community in the 1980s and 1990s, and much more recently in the amateur community as described below.

Several factors can affect the determined CCD magnitude. Atmospheric conditions, such as dust or pollution levels, extinction, and weather, can affect the amount of light that reaches the CCD sensor, potentially influencing the measured magnitudes. Various instrumental factors, including the sensitivity and calibration of the CCD camera, the filter used, and the observing setup of the telescope itself, can introduce systematic biases into the photometric measurements. The data reduction process, including background subtraction and flat-fielding, and image registration, can remove artifacts and improve the accuracy of the measured magnitudes. Finally, the methods of the photometric calibration, including the size and shape of the photometric aperture, the stars used for calibration (e.g., brightness, color, reference catalog), and method of sky determination, can all affect the final magnitudes.

With a consistent methodology between observers, CCD observations should have significantly less observer bias than visual observations. After reviewing several cometary datasets, Kidger (2002) concluded that defining an appropriate standard aperture for measurements, a standard photometric system, and a standard reference catalog can greatly reduce the dispersion of amateur CCD photometry data. They proposed employing a fixed aperture size of 10 arcseconds in an R-filtered image. They also suggested using the USNO A2.0 reference catalog, which at the time was the only widely available catalog that gave B and R magnitudes and covered the full sky to a faint magnitude with reasonable photometric reliability (on the order of 0.2 magnitudes). While these recommendations represent a

movement to standardize the methodologies among amateur astronomers, the recommendations have never been fully implemented (and are now outdated) as current methodologies vary from observer to observer. Some guides are available, but most of them are decades old (e.g., Howell, 1989; Green, 1997). The 2022 Pro-Am Comet Workshop, organized in cooperation with Europlanet 2024 Research Infrastructure (RI), the British Astronomical Association, Planetum Prague, and the Czech cometary community SMPH, consisted of many in-depth discussions related to the standardization of CCD observations (Usher et al., 2022). Now that CCD submissions are more popular among amateur astronomers, we can assess the self-consistency between methods on actual submitted data and measurements from professional facilities.

4.2.2 Comet OBServation Database (COBS)

The Comet OBServation database (COBS)*, maintained by Crni Vrh Observatory since 2010, provides a freely available singular location for the submission, display, and analysis of cometary data (Zakrajsek & Mikuz, 2018). One of the primary functions of COBS is to provide a platform for individuals to contribute their comet observations in the form of astrometric and/or photometric data points. Users can create profiles, communicate with other members, and participate in discussions related to comet observations. The platform also offers tools for generating tables and figures to visualize comet data, further aiding in analysis and research.

The COBS database includes over 250,000 observations of ∼1500 comets (mostly

*https://www.cobs.si/

LPCs) from ∼2400 contributing observers in 72 countries[†]. The majority of submissions are visual observations. However, CCD observations, where magnitudes are determined by adding the counts of the pixels of the CCD within an aperture, are becoming increasingly more popular among the amateur community as the necessary instruments and software become more accessible. In COBS, the number of CCD submissions has nearly doubled the number of visual submissions consistently over the last three years.

Data are submitted in the ICQ format (Green, 1997), which allows observers to describe the observing conditions and reduction/calibration methods in more detail. In 2001, the format was extended for CCD observations only. Several columns use keys to describe certain parameters[‡] and these keys range in detail. For example, in the methods category there is a key for "Kron-Cousins V filter employed (m2 estimate)", "Kron-Cousins V filter employed", "Johnson/Bessel/Kron/Cousins V with CCD". Any amount of detail can be useful to determine biases in the observations that can potentially be corrected. However, the options should be simple enough to automatically parse the data in a way that makes sense for any science goal.

4.2.3 Analysis of CCD Variables

We analyzed the CCD lightcurves of the comets with the most data and assessed how different observing methods affect the final reported magnitudes, with the goal of discovering cuts and/or conversions that can be made to improve accuracy and reduce scatter of the lightcurve. We assessed 13 comets with over 100 submitted CCD magnitudes that

[†]`https://www.cobs.si/statistic/`
[‡]for example, `https://www.cobs.si/help/icq_list/obs_methods/`

covered a heliocentric distance range of $\Delta r_h > 1$ au. Some of these do not have corresponding orbital information from the CODE catalog, but possess a substantial amount of data points, making them ideal examples for the first part of our study.

This data "trimming" was done for studies of comet Hale-Bopp that used amateur data (e.g., de Almeida et al., 2009; Womack et al., 2021). During their research, Womack et al. (2021) formulated an algorithm named ICQSPLITTER[§] to minimize variation and enhance the accuracy of a lightcurve compiled from many observers. Our initial CCD data pruning began with three cuts made during the Hale-Bopp study, followed by additional reductions not used by Womack et al. (2021), ultimately decreasing the number of data points for each comet by ∼15% on average. Our study did not include any values where:

- poor observing conditions were noted
- observations occurred under 20 degrees elevation with no extinction correction applied
- the image was not fully reduced (bias-subtracted and flat-fielded)
- pixel resolution was worse than 6 arcseconds per pixel
- exposure time was less than one second
- the photometric aperture size was not listed
- the reported magnitude error was greater than 0.5

After the initial cuts were made, we assessed the distribution of the different variables for each parameter and searched for any trends that may contribute to the overall scatter. Below we discuss our findings for the parameters that show significant variance.

[§]`https://github.com/curtisa1/ICQSplitter`

4.2.3.1 Broadband Filters

Broadband filters are designed to transmit light within a certain range of wavelengths while blocking or attenuating light outside that range. Different filters have different transmission profiles, which determine the specific wavelengths they transmit and the amount of light they allow through. Comets have unique spectral properties and can exhibit significant variations in their brightness at different wavelengths, resulting in different apparent magnitudes for different filters. These variations arise from a combination of factors related to the comet's composition and physical properties, which impact the scattering and absorption of light in the coma. For amateur astronomers who may only have a single filter, it is generally recommended to probe the dust in the coma by using a filter that contains minimal gas emission lines frequently seen in comets, such as the Johnson-Cousins R filter, which also has a high throughput, allowing for fainter observations.

In the ICQ format, the filter used does not have its own column but is entered in the *method type* category[¶]. In our comet sample, a variety of filters are used, but the most common are the Johnson-Cousins $BVRI$ filters or no filter at all (listed as "Unfiltered total CCD magnitude"). Jonathan Shanklin introduced a method called "CCD Visual Equivalent", where a CCD image of a comet is compared to the same image blurred using a transform to simulate the in-out focus method used for visual observations (Shanklin, 2004). A tutorial for this method was conducted at a comets and meteors observers workshop coordinated by the British Astronomical Association in 2015 and has since dominated the *method type* category in the CCD submissions in the last few years. However, because there

[¶]see `https://www.cobs.si/help/icq_list/obs_methods/`

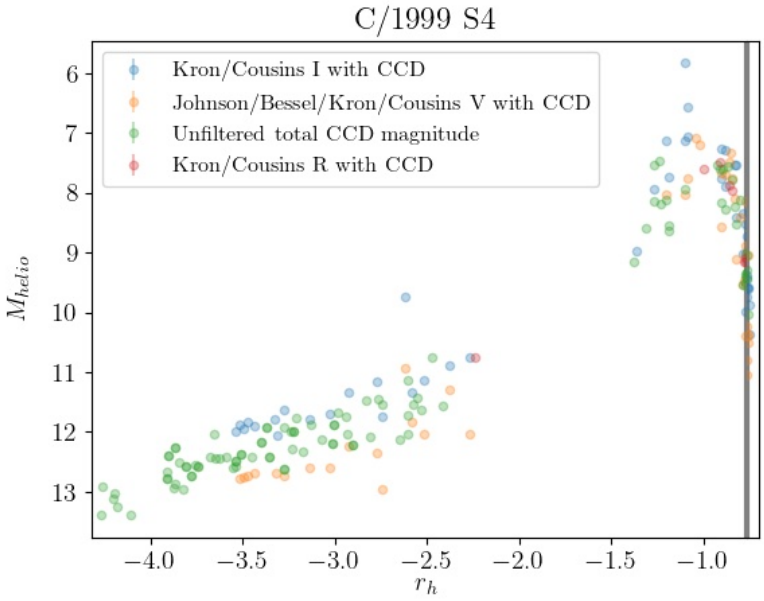

Figure 4.2: Amateur observations from COBS of comet C/1999 S4, colored according to the photometric filter. The unfiltered observations are the most abundant. A clear offset between filters can be seen, which is representative of the coma color.

is not a separate *filter* category and only one option can be chosen for the *method type*, choosing "CCD Visual Equivalent" leaves the filter used unstated. Sometimes a filter may be listed in the comments column, but not in a standardized way that is simple to parse. The comets that we use in our study of dynamical age were discovered prior to 2018 and the amount of "CCD Visual Equivalent" magnitudes reported is negligible, so we exclude them from our analysis in Section 4.3, but for comets observed today, this method is the most common, eliminating the reporting of the used filter for most of the submissions.

We find a noticeable offset between filters, especially Johnson-Cousins V and I (Figure 4.2). If we remove the data points associated with the CCD Visual Equivalent method, we find that unfiltered images and those using the R filter significantly outnumber other filters used. For our purposes of constraining the CCD lightcurve, we remove all data points using any filter other than Johnson-Cousins R.

4.2.3.2 Photometric Aperture Size

The size of the photometric aperture has a notable influence on the measured magnitude (Kidger, 2002), yet there is no universally optimal aperture size applicable to all comets at any given heliocentric distance. For any given image, the ideal aperture size is larger than several times the seeing, but small enough to minimize contamination from the background.

Even though a standard aperture size has not been implemented, the latest ICQ format contains a column for aperture size. We find that most observers use a dynamic aperture size, most likely determined by the photometry software used. In a few instances, one or two observers used a fixed angular aperture size, which diverged from the other observations as the heliocentric distance decreased since the fixed angular aperture encompassed progressively less physical distance (Figure 4.3). In these instances, we can make a correction for aperture size by fitting the difference between the consensus fit without the fixed aperture observations and the fixed aperture observations.

4.2.3.3 Observer

The software and reference catalog used has the potential to play an important role in standardization. We did find a correlation between software and reference catalog but ultimately discovered that both variables are tied to the observer (Figure 4.4). Unfortunately, there is not enough data to disentangle the catalog or software from the observer to determine which method is the most consistent between observers. Therefore, it seems that even with CCD observations, observer bias is still quite present. We investigate ICQSplitter's

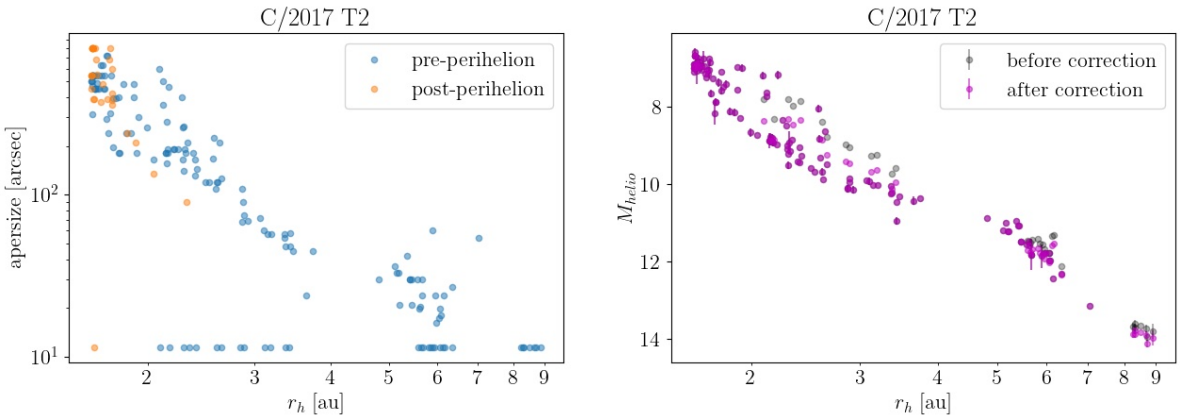

Figure 4.3: **Left:** The aperture size for all observations vs heliocentric distance. Most follow a dynamic aperture size that changes with r_h, but one observer uses a constant aperture size of ∼10 arcseconds, causing a deviation near perihelion. **Right:** The same observations with m_{helio} vs r_h before (gray points) and after (pink points) correcting the observations that used a static aperture size.

treatment of observer bias in the next section.

4.2.4 ICQSplitter

The ICQSplitter algorithm was developed to synthesize visual observations of comet Hale-Bopp. For this chapter, we use the algorithm to constrain the visual lightcurves for our analysis. In addition to the cuts listed in Section 4.2.3, ICQSplitter removes any visual observations that use an observing method other than the Vsekhsvyatskij-Stevenson-Sidgwick, Van Biesbroeck-Bobrovnikoff-Meisel, Modified Out-Out, Infocus, or Extrafocal-Extinction methods. They also remove any observations where telescopes were used for an apparent magnitude brighter than 5.5 and where binoculars were used for an apparent magnitude brighter than 1.5.

The essential feature of ICQSplitter is the way it handles observer bias by correcting three categories of assumed errors using an iterative process. 1.) Every observer has a bias

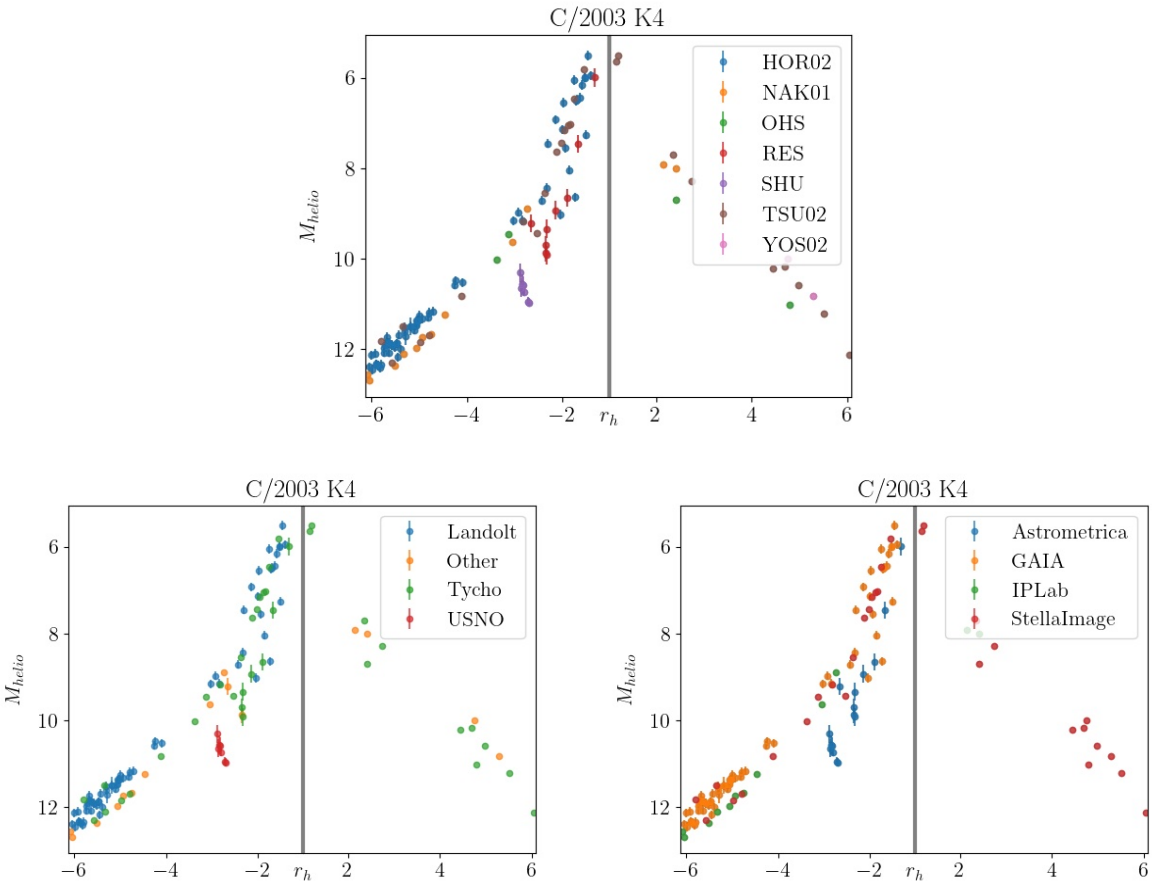

Figure 4.4: Heliocentric light curve of C/2003 K4 with color-coded ICQ variables. The upper panel is colored by observer, bottom left is colored by reference catalog, and the lower left has colors related to software. We ultimately found that these variables are closely tied to each other.

shifted up or down from other observers which is determined by the deviation from the consensus fit and corrected for. 2.) Some observers have more scatter in their data but not a shifted bias, so the observations are weighted less when determining a fit. 3.) Some observers may have what the authors call a "slope bias", where the brightness of dimmer objects is underestimated and overestimated for brighter objects or vice-versa. ICQSplitter detects the slope bias relative to the consensus fit and discards that observer's data. While the observer bias is still present in the CCD data, the ICQSplitter algorithm is able to correct for most of these biases (Figure 4.5).

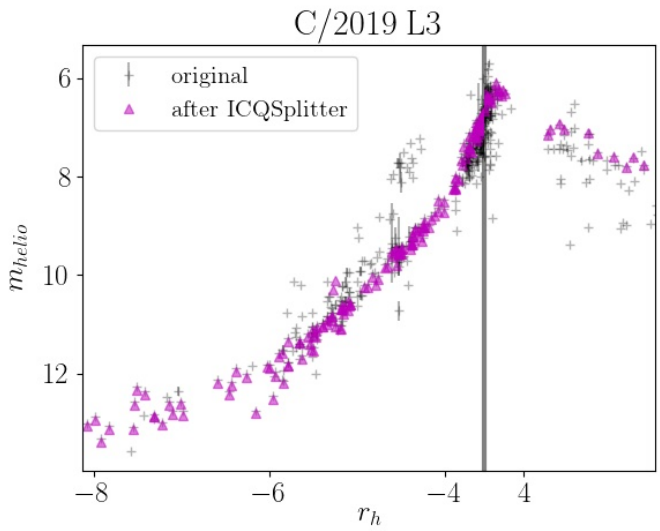

Figure 4.5: An example of ICQSplitter cuts and shifts for comet C/2019 L3 where the gray crosses are the original data, and the magenta triangles are the data after processing by ICQSplitter. The scatter is minimized significantly.

4.3 Data Analysis

For each comet, we use five datasets: all visual data with no cuts, visual data with cuts and observer shifts by ICQSplitter, all CCD data with no cuts, CCD data with CCD-specific cuts, and CCD data with cuts and observer shifts by ICQSplitter. Using the same methods as in Section 3.4.1, we first converted the apparent magnitudes to heliocentric magnitudes, then fit each dataset with a pre-perihelion and post-perihelion curve that follows:

$$m_{helio} = m_0 + 2.5n \log_{10}(r_h) \tag{4.1}$$

to determine the activity index, n, using a least squares fit. In the equation, r_h represents the distance from the Sun to the comet in au, while m_0 corresponds to the absolute magnitude—an indicator of the comet's intrinsic brightness under specific conditions: 1 au from both the Earth and Sun, with a phase angle of 0 degrees. If a "break" is detected,

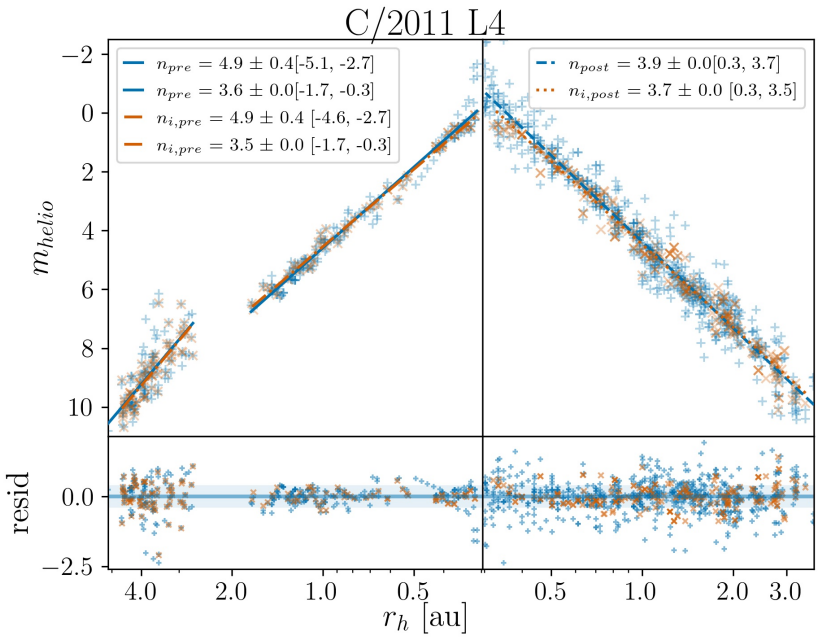

Figure 4.6: An example lightcurve with least-squares fit to the activity index. The blue plus signs is the lightcurve after initial cuts and the orange 'x' is after ICQSplitter processing. The bottom panel shows the residuals of the fits and the blue shaded area is the standard deviation of the residuals.

we independently fit each section. Since the algorithms may occasionally trim excessive or insufficient portions of the original dataset, we select the best-fit activity index from all datasets for each comet (see example in Figure 4.6). In Table 4.1, we present an overview of the analyzed comets and their range of heliocentric distances and corresponding activity indices where the fitting process converged, using the σ value from the dataset with the best fit. Once we determined the activity indices, we compared our results with the dynamical model for each comet to characterize the effects of dynamical age on brightness behavior. We describe the model below in Section 4.4 before discussing our final results in Section 4.5.

Table 4.1: Activity Indices

Name	r_{min}[a]	r_{max}[b]	n[c]	$r_h < 3$ au behavior[d]
C/1995 Y1	1.1	1.4	4.3 ± 0.5	
C/1997 BA6	-8.9	-4.6	5.3 ± 0.1	
	4.1	9.0	3.3 ± 0.5	
C/1997 J2	-4.1	-3.1	4.0 ± 0.4	
	3.1	4.0	3.0 ± 0.5	
C/1998 P1	1.2	3.2	3.7 ± 0.2	power-law
C/1999 S4	-4.1	-2.4	3.0 ± 0.2	
	-1.4	-1.0	6.8 ± 0.5	disintegration
C/1999 Y1	-5.2	-3.1	5.0 ± 0.2	
C/2000 SV74	-4.4	-3.5	3.0 ± 0.4	
C/2001 B2	5.4	9.9	3.7 ± 0.3	
C/2001 Q4	1.0	2.0	2.2 ± 0.4	
	2.0	3.0	6.5 ± 0.3	surge
C/2002 T7	-4.0	-2.4	3.0 ± 0.3	
	-2.4	-1.8	7.5 ± 0.4	surge
	-1.8	-0.6	2.0 ± 0.2	
	0.9	7.7	3.0 ± 0.2	
C/2003 K4	-6.1	-4.1	4.4 ± 0.3	
	-3.5	-2.0	7.0 ± 0.6	surge
	-1.9	-1.2	3.1 ± 0.1	
	1.2	6.0	3.3 ± 0.2	
C/2003 T3	-2.3	-1.6	3.7 ± 0.4	
C/2004 B1	-7.6	-4.3	4.1 ± 0.7	
	1.7	4.7	2.4 ± 0.4	
C/2005 B1	-4.9	-3.2	3.3 ± 0.3	
C/2005 E2	-3.9	-1.7	3.7 ± 0.2	power-law
C/2006 P1	0.4	1.3	3.0 ± 0.1	
	1.3	2.5	6.3 ± 0.4	
C/2007 Q3	-4.1	-2.6	7.4 ± 0.4	surge
C/2008 A1	-2.7	-1.1	4.0 ± 0.2	power-law
C/2009 K5	1.5	2.0	4.9 ± 0.2	
C/2009 R1	-1.2	-0.5	3.0 ± 0.4	
C/2010 X1	-4.2	-1.3	4.7 ± 0.2	disintegration
C/2011 L4	-4.6	-2.7	4.9 ± 0.4	
	-1.7	-0.3	3.5 ± 0.1	power-law
	0.3	3.5	3.8 ± 0.1	
C/2011 R1	-4.5	-2.1	3.6 ± 0.3	
C/2012 K1	-5.8	-1.4	3.8 ± 0.1	
	1.1	4.1	3.8 ± 0.1	
C/2012 S1	-6.1	-0.1	2.8 ± 0.1	disintegration
C/2017 B3	4.0	6.8	2.3 ± 0.2	
C/2017 K2	-16.0	-1.9	3.0 ± 0.1	surge

[a] Starting heliocentric distance where a negative value represents pre-perihelion.
[b] Ending heliocentric distance where a negative value represents pre-perihelion.
[c] Activity index as defined in Equation 4.1 determined by least-squares fit with 1σ errors
[d] Brightness behavior when $r_h < 3$ au where "power-law" means a steady increase in activity, "surge" means a rapid increase in brightness that was quickly followed by a lower rate of brightening, and "disintegration" means the comet disintegrated.

4.4 Catalogue of Cometary Orbits and their Dynamical Evolution (CODE)

The Catalogue of Cometary Orbits and their Dynamical Evolution (CODE) is a new cometary catalog containing extensive orbital information for nearly 300 comets discovered before 2018 with orbits within the "Oort Spike" (Królikowska, 2020). This catalog is the first of its kind, featuring cometary orbits in five stages of their dynamical evolution and spanning three consecutive passages (previous, current, and next) through perihelion. Different orbital solutions based on alternative force models or specific subsets of positional data are provided for many of the featured comets, with the preferred orbit clearly indicated. The catalog includes non-gravitational orbits for around 100 long-period comets, along with their orbits calculated without considering non-gravitational acceleration for comparison.

In their determination of the osculating orbit, they use the Bessel criterion for their data selection procedure, as well as weight each astrometric point in relation to the observing site and time of observations (Królikowska & Dybczyński, 2010; Królikowska et al., 2014). They also include non-gravitational acceleration when detected (Królikowska, 2020), which has been found to greatly influence the $1/a_0$ value (see Section 1.4.1). Their dynamical modeling is unique compared to other models because they include the effects of galactic tides and stellar perturbers to determine past and future movement of the comet. These effects are negligible when determining original orbits, but must be included in the model in order to determine the past motions, such as the previous perihelion distance (Dybczyński, 2001, 2006). The orbital parameters from the preferred model related to the dynamical age for each of the comets with sufficient COBS data are summarized in Table 4.2.

Table 4.2: Orbital Parameters from CODE[a]

Name	$1/a_0 \times 10^6$ [au^{-1}]	$q_{prev}[au]$[b]			Dynamical Status[c]
		p10	median	p90	
C/1995 Y1	-48.77 ± 9.04	21.048	23.61	26.474	DN+
C/1997 BA6	31.83 ± 1.15	3.1	3.922	7.359	DO+
C/1997 J2	44.64 ± 0.88	3.56	3.619	3.692	DO+
C/1998 P1	228.12 ± 5.4	1.1408	1.1413	1.1419	DO+
C/1999 S4	6.24 ± 1.67	46.118	46.165	46.41	DN+
C/1999 Y1	37.94 ± 1.85	11.4	13.864	17.617	DU
C/2000 SV74	68.28 ± 1.16	12.891	13.263	13.73	DU
C/2001 B2	199.3 ± 1.1	5.3285	5.3293	5.3301	DO+
C/2001 Q4	49.29 ± 0.96	16.858	17.049	17.407	DU
C/2002 T7	21.65 ± 0.86	21.56	22.43	23.3	DN+
C/2003 K4	51.07 ± 1.6	6.044	6.496	6.972	DO+
C/2003 T3	-1.82 ± 4.85	12.425	17.235	22.025	DN
C/2004 B1	35.85 ± 0.71	3.382	172.366	245.462	DN
C/2005 B1	3.99 ± 0.61	18.887	19.363	19.839	DN+
C/2005 E2	7.30 ± 1.38	64.89	67.57	70.25	DN+
C/2006 P1	57.17 ± 4.03	1.217	7.707	261.712	DO
C/2007 Q3	40.79 ± 0.58	31.194	34.36	37.526	DN+
C/2008 A1	123.07 ± 1.5	1.164	1.666	1.171	DO+
C/2009 K5	46 ± 0.26	5.289	5.457	5.625	DO+
C/2009 R1	12.16 ± 3.29	672.853	1369.967	1989.129	DN+
C/2010 X1	27.24 ± 3.95	87.16	169.011	402.953	DN+
C/2011 L4	30.84 ± 0.47	63.315	70.29	77.989	DN+
C/2011 R1	45.44 ± 0.67	12.789	14.091	15.247	DU
C/2012 K1	40.31 ± 0.27	7.175	7.751	8.327	DO+
C/2012 S1	22.39 ± 12.63	9.341	75.558	996.939	DN
C/2017 B3	301.44 ± 0.85	3.9291	3.92915	3.9292	DO+
C/2017 K2	35.49 ± 2.33	373.5	441.6	490	DN+

[a] All parameters use the significant figures described by CODE, which corresponds to the precision of the model.

[b] Three deciles at 10, 50 (median), and 90 percent of the q_{prev} distribution for the modeled test particles.

[c] Dynamical status as described by CODE where DU is dynamically uncertain ($10 < q_{prev} < 20$ au), DN is dynamically new ($q_{prev} > 20$ au) (DN+ if 95% of the test particles have $q_{prev} > 20$ au), and DO is dynamically old ($q_{prev} < 10$ au) (DO+ if 95% of the test particles have $q_{prev} < 10$ au).

4.5 Results

4.5.1 Activity with Heliocentric Distance

The activity indices for our sample remained between 2 and 8, which is consistent with other comet observations (Meisel & Morris, 1976; Meech & Svoren, 2004). We find that for inbound long-period comets, the rate of brightening is the steepest for comets further from the Sun and is more shallow for comets closer to the Sun (Figure 4.7). However, when we consider the comets individually and their breaks in activity rate, we find that only one comet has an observed shallower break during pre-perihelion, C/2011 L4. Other comets with an observed break exhibit a "surge" around 3 au from the Sun followed by a more shallow increase, which we discuss further below. While there is a gap between the two portions of the secular light curve for C/2011 L4, the starting magnitude of the second portion is too low for a surge to have taken place during that gap.

Post-perihelion, the activity indices generally remain below 4, averaging $n = 3.2 \pm 0.5$ (Figure 4.8), with the exception of C/2001 Q4 and C/2009 K5. Only 7 objects in our sample have enough data to determine an activity index both pre- and post-perihelion (Figure 4.9). Of those objects, two exhibit a surge pre-perihelion but return to an activity index below 4 post-perihelion. The objects that showed no break pre-perihelion had a similar or lower activity index post-perihelion. The other three objects that have an observed break and a perihelion distance less than 2.5 au have a higher activity index post-perihelion than the last activity index measured pre-perihelion.

For comets that pass within 2.5 au of the Sun (14/27 objects in our sample), the

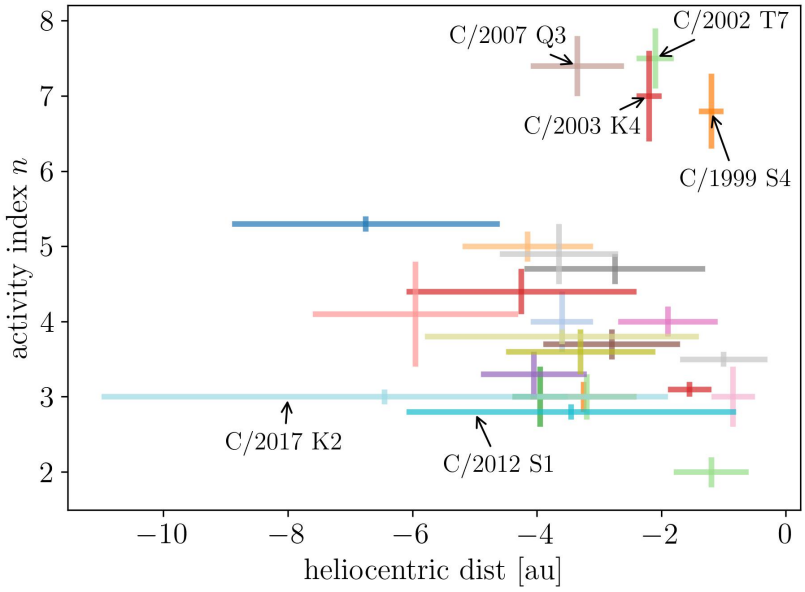

Figure 4.7: The changing activity indices of the sample with heliocentric distance, where each color relates to a single comet. The y-error is the 1σ uncertainty for n and the x-error is the heliocentric distance range corresponding to that activity index. More distant objects have a higher activity index compared to objects closer to the Sun. The exceptions are the four objects in the top right, which experienced surges in activity at those points.

brightness behavior as it relates to heliocentric distance can be categorized into three different groups. The first is a power law, where a single activity index is consistent with all observations. Comet C/2005 E2 is the only object in our sample with observation within 2.5 au that fits into this category, so we also include C/2011 L4 as the only object where the activity index decreases when it is closer to the Sun. The second category contains the majority of the near-Sun sample with 10 objects that exhibit a "surge" where the activity significantly increases around $r_h \sim 2 - 3$ au. Two of the 14 comets in our near-Sun subsample do not have enough frequently-cadenced data to determine a category. We only determined post-perihelion activity indices for comets C/1998 P1 and C/2001 Q4, so our investigation into characterized pre-perihelion behavior with $r_h < 2.5$ au is limited to 10 objects.

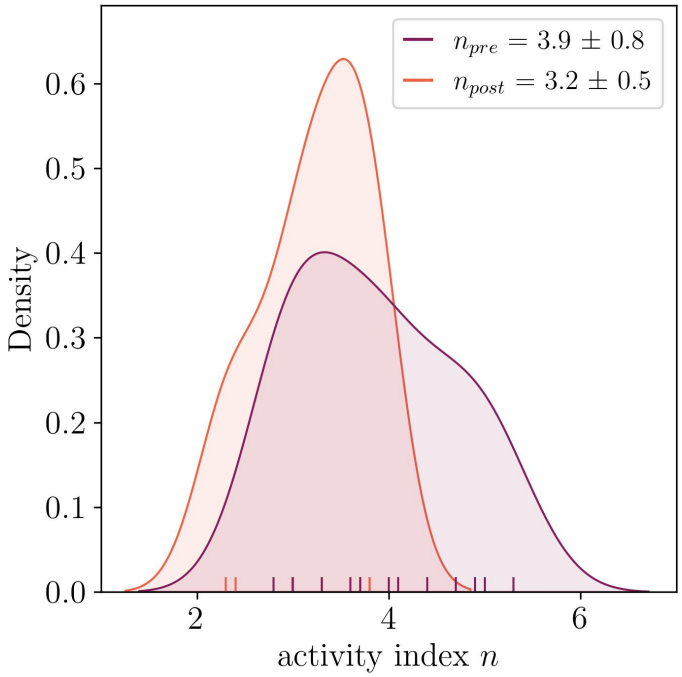

Figure 4.8: Distribution of activity indices pre- and post-perihelion using only observations beyond 3 au from the Sun. Though having similar peaks, pre-perihelion has several objects with $n > 4$, compared to no objects post-perihelion.

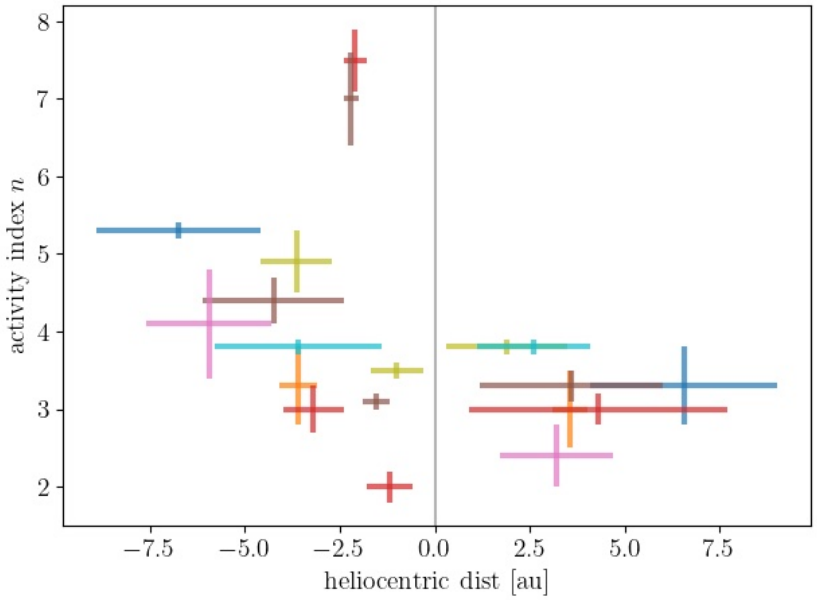

Figure 4.9: Activity index vs heliocentric distance for the comets in our sample with determined activity indices both pre- and post-perihelion, where each color is a single comet. The three objects within 2.5 au are the only objects that have a larger n post-perihelion.

The surge category can be further broken down into the third category - disruption. Five of the comets had their brightening rate become more shallow post-surge (see example in Figure 4.10). However, three of these disintegrated near perihelion: C/1999 S4 (Bockelée-Morvan et al., 2001; Farnham et al., 2001), C/2010 X1 (Korsun et al., 2012; Li & Jewitt, 2015), and C/2012 S1 (Knight & Battams, 2014; Sekanina & Kracht, 2014). Comets C/1999 S4 and C/2010 X1 both exhibited a rapid decrease in brightness post-surge, but still pre-perihelion. C/2012 S1's surge did not show a rapid decrease or a flattening out of activity pre-perihelion. All three comets that disintegrated had a perihelion distance $q < 1$ au. The perihelion survival limit by Bortle (1991) places C/2012 S1 past the survival limit, while the other two were predicted to survive. However, the updated limit by Sekanina (2019), which incorporates the dust parameter $Af\rho$, accurately places all three comets past the survival limit. We summarize the near-Sun brightness behavior in Table 4.1.

In order to investigate early signs of near-Sun activity changes, we compare the comet's behavior (disintegration, surge, or power law) with its n when $r_h > 3$ au. Because two of the near-Sun objects only have categorized behavior post-perihelion and one object was first observed with $r_h < 3$ au, we are limited to a small sample size of nine objects. We find that comets with a lower activity index beyond 3 au from the Sun are more likely to experience a surge in brightness near the Sun and potentially disintegrate (Figure 4.11). However, the opposite is not true for higher activity indices ($n \sim 4 - 5$), where the comet may experience a surge or may not.

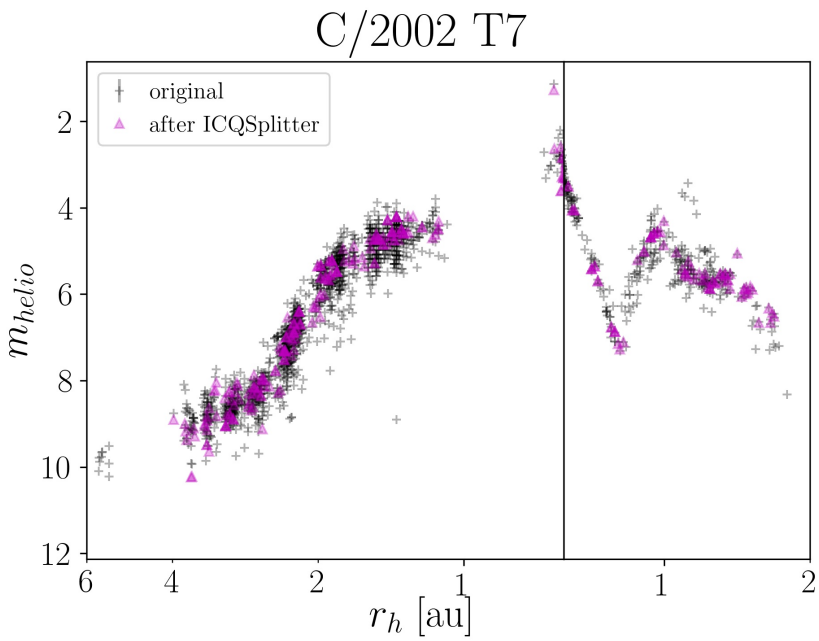

Figure 4.10: Secular lightcurve of C/2002 T7 with heliocentric distance where the left plot is pre-perihelion, and the right is post-perihelion. The gray points are the original COBS data and the magenta are after ICQSplitter cuts and shifts. A surge in brightness is observed where $r_h \sim 2$ au pre-perihelion. The dip in brightness post-perihelion corresponds to the comet's close approach to Earth, so a likely explanation is that the apertures used were not large enough to encompass the entire coma.

4.5.2 Comparisons with Dynamical Age

Comparing the total pre-perihelion activity index (best-fit with no breaks) to the CODE-derived dynamical status revealed that dynamically old comets exhibit a steeper rate of brightening compared to dynamically new comets, although there is significant overlap (Figure 4.12). When we compared the activity indices to previous perihelion distance q_{prev} from CODE, there is large scatter, but a slight trend can be observed where a smaller q_{prev} correlated to a higher activity index (Figure 4.13). The lightcurves of two comets (C/2007 Q3 and C/2010 X1) are dominated by a period of rapid brightening (surge), which consequently results in a higher activity index than it would otherwise be.

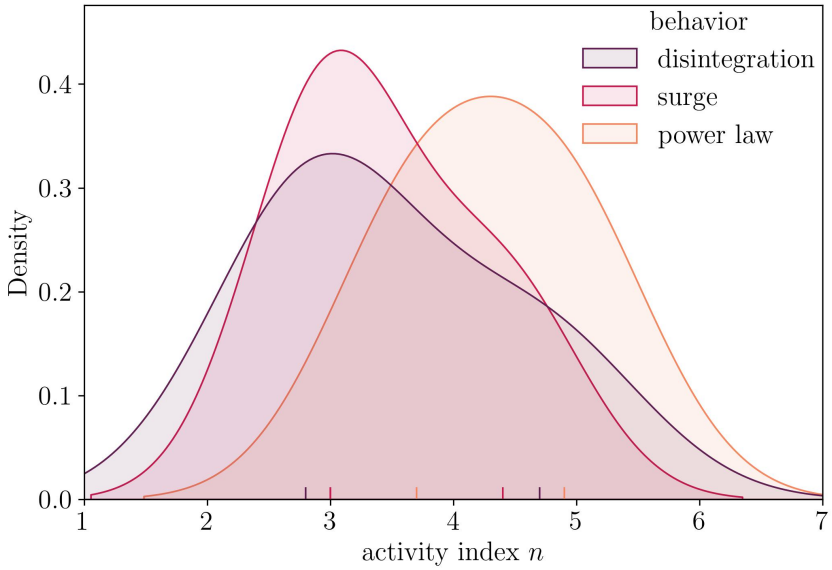

Figure 4.11: The distribution of activity indices when $r_h > 3$ au compared to the brightness behavior when $r_h < 3$ au. We find that comets with a lower activity index beyond 3 au from the Sun are more likely to experience a surge in brightness when $r_h < 3$ au and potentially disintegrate. However, the opposite is not true for activity indices $n \lesssim 4 - 5$, where the comet may experience a surge or may not.

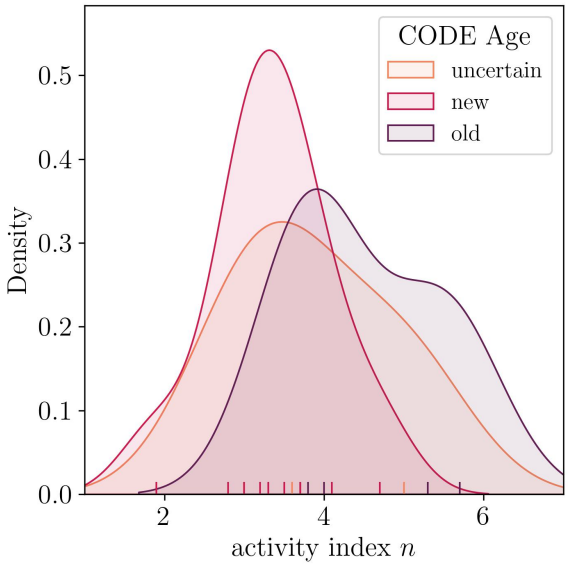

Figure 4.12: Distribution of activity indices for different dynamical statuses. Though there is large overlap, the peaks of each distribution vary so that dynamically new comets have a lower activity index and dynamically old comets have a higher activity index.

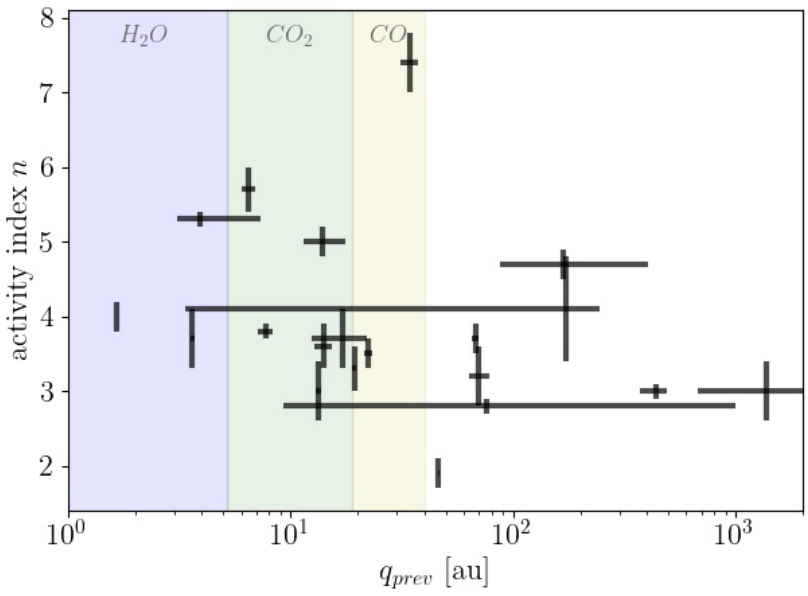

Figure 4.13: The brightening rate as a function of q_{prev}. We only include observations with $r_h > 3$ au and fit one activity index per comet. The shaded vertical sections indicate the sublimation regions of three major cometary volatiles. There is a slight trend where dynamically older comets (comets with a smaller q_{prev}) have a higher activity index than dynamically newer comets. However, some activity indices are heavily influenced by the heliocentric distance region where it was determined.

When examining the q_{prev} distribution of different near-Sun behaviors, we discover that the extent of prior heating plays a significant role. Among the five objects exhibiting an activity surge when $r_h < 3$ au, four have a q_{prev} falling within the range of CO and/or CO_2 sublimation but outside the range of water-ice sublimation (Figure 4.14). Additionally, the three comets that disintegrated were all found to be dynamically new with $q_{prev} > 40$ au, and they all approached within 1 au of the Sun during their observed epoch. However, the dynamically new comet C/2011 L4 successfully orbited within 1 au of the Sun without disintegrating.

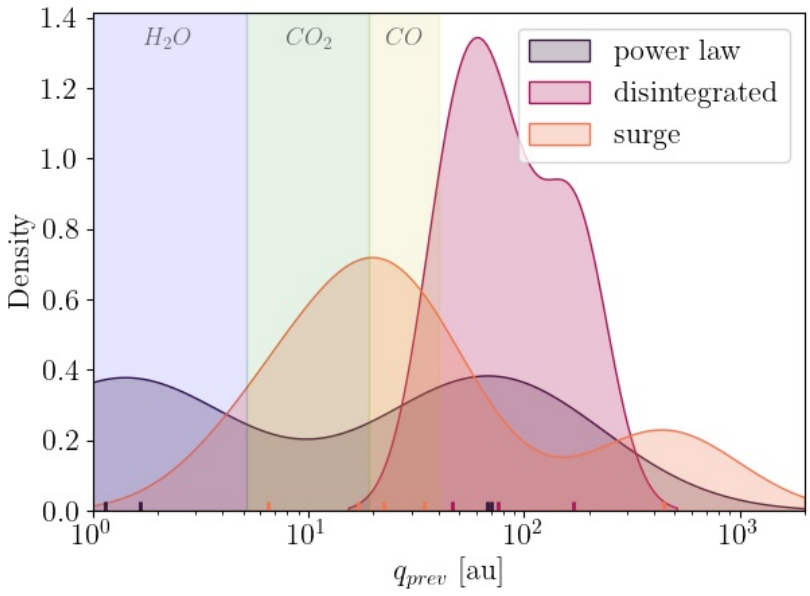

Figure 4.14: q_{prev} distribution of different near-Sun brightness behaviors. The shaded vertical sections indicate the sublimation regions of three major cometary volatiles. The q_{prev} value can be seen as a small line at the bottom of the figure. Comets that experience a surge in brightness have a previous perihelion distance within the sublimation regimes of CO and CO_2, but not water. All three of the disintegrated comets have a previous perihelion distance beyond the sublimation region of CO.

4.6 Discussion

Before delving into our interpretations, it is important to acknowledge that we are working with a limited dataset. While we can offer speculations based on the available information, drawing more conclusive statements will require a substantially larger sample of comets.

4.6.1 Dynamic Brightening Rates

A shallow increase in activity for long-period comets has been frequently observed. In most of these cases, a rapid brightening further from the Sun is either implied (e.g., Whipple,

1978) or observed (e.g., Meech et al., 2017b). By comparing the brightening rate versus heliocentric distance for multiple objects, we find that rapid brightening that shallows near perihelion is common for nearly all long-period comets, regardless of dynamical age (Figure 4.7). There are some exceptions to this, which we discuss further in Section 4.6.2.

The post-perihelion phase does not exhibit the same pattern as pre-perihelion. This divergence is likely attributable to the accumulation of a dust mantle, which is presumably a uniform process among all long-period comets, resulting in a consistent decline in activity at a rate of approximately $n \sim 4$. Previous investigations have demonstrated that dynamically new comets display a lower activity index ($n \sim 2$) before perihelion, which subsequently decreases more steeply ($n \sim 4$) after perihelion (Whipple, 1978; A'Hearn et al., 1995). In our sample, this phenomenon occurs solely in comets that underwent an initial surge followed by sustained activity with an index of $n \sim 2$ within 3 au of the Sun. Other comets may not attain equivalent levels of peak gas production, either due to their larger perihelion distance or as a consequence of a prior close encounter with the Sun.

4.6.2 Activity Mechanisms

We separate our objects into three categories based on q_{prev}: dynamically old ($q_{prev} <$ 6 au where water-ice sublimates), dynamically new ($q_{prev} > 40$ au outside the sublimation region of CO and CO_2), and in-between ($6 < q_{prev} < 40$ au where CO or CO_2 sublimation has occurred on a previous passage but not water-ice sublimation). The q_{prev} range of the in-between comets is much larger than the "uncertain" category defined by CODE as $10 < q_{prev} < 20$ au because we use different methodologies. Our range is based on

the physics of the ice sublimation, whereas CODE is focused on statistical analysis. In this discussion, we attempt to describe the pre-perihelion brightness behavior and possible activity mechanisms for each category based on our results.

4.6.2.1 Dynamically New Comets

Dynamically new comets are considered to have the least amount of processing since their cold storage phase in the Oort Cloud and likely contain more volatile ices, such as CO. C/2017 K2 and C/2012 S1 are the only two comets with $r_h > 5$ au that do not follow the overall trend of decreasing n with decreasing r_h, but instead, maintain a more shallow rate of activity near $n \sim 3$. They are also both considered dynamically new. One other suggested dynamically new comet C/2004 B1 has a larger activity index of $n \sim 4$ when $r_h > 5$ au. However, there is a possibility that it is actually dynamically older as there is much uncertainty in its q_{prev} value, ranging from ∼3–245 au. Using a sublimation model K2's distant activity has been attributed to CO sublimation (Meech et al., 2017a). So the shallow increase in activity when $r_h > 5$ au is likely driven by CO sublimation that began much further from the Sun (e.g., ∼35 au as suggested by Jewitt et al., 2021, for K2).

If a dynamically new comet has $q < 2.5$ au, it will sometimes experience a surge in brightness followed by disintegration, which occurred for approximately half of the DNCs with $q < 2.5$ au. The objects that disintegrated had a higher estimated total magnitude according to JPL Horizons[‖], suggesting that smaller objects are more likely to disrupt. The larger comets do not experience a significant surge either, suggesting that the mechanism responsible for the surge in brightness could be the same mechanism responsible for the

[‖] `https://ssd.jpl.nasa.gov/tools/sbdb_lookup.html`

disruption. Possibilities include water-ice sublimation or the transition from amorphous to crystalline water-ice (e.g., Herman & Podolak, 1985; Meech & Svoren, 2004).

4.6.2.2 Dynamically Old Comets

Dynamically old comets are the smallest in our sample with only two definite objects and two that are uncertain, which is expected because Oort cloud comets are thought to fade or disintegrate after their first few solar passages (Wiegert & Tremaine, 1999; Levison et al., 2002). Because these objects have previously experienced water-ice sublimation and have built up a dust mantle, they experience a brightening rate of $n \sim 4$, as more areas become active. Comet C/2008 A1 also exhibits a pre-perihelion peak, consistent with seasonal effects, wherein an active region alternates in and out of sunlight due to the orientation of the rotational pole, which leads to an activity peak that is offset from perihelion.

4.6.2.3 Dynamically In-Between Comets

The last category is dynamically in-between, where hypervolatile sublimation was possible on their previous solar passage, but not water-ice sublimation. We call these objects dynamically "in-between" comets. We find that within 2.5 au of the Sun, all dynamically in-between comets experienced a rapid increase in brightness that then decreased to a constant activity rate. This S-shape curve is indicative of a previously inactive species "turning on", causing an outburst. As the dust from the initial outburst disperses, the brightness rate continues to increase at a similar rate as before the "surge". This behavior has been used

to explain the steep brightening behavior of Kreutz comets (Knight et al., 2010). Another explanation could be the transition from the crystallization of amorphous water-ice, which releases trapped gases in a "surge" of activity (Meech & Svoren, 2004).

Harrington Pinto et al. (2022) reports that dynamically new comets are more depleted in CO compared to returning comets. However, when we investigate the CODE q_{prev} values of the six Oort spike comets with CO/CO_2 measurements reported in the Harrington Pinto et al. (2022) study, we find that the most depleted comets are dynamically in-between (four out of six). The one dynamically old comet and one dynamically new comet both have comparable values of CO and CO_2 in their coma. Therefore, the depletion of CO in the surface layers may not be due to processing in the Oort Cloud as suggested, but by volatile outgassing during a previous solar passage. During the surge, the upper layers depleted of CO are blown off of the surface, allowing the observed CO/CO_2 ratio to increase during the comet's next solar passage. With the upper layers depleted of CO, some of the in-between comets increase in activity when $r_h \lesssim$ 5–6 au, consistent with the beginning of water-ice sublimation (Meech & Svoren, 2004). Others experience a brightening increase between $\sim$ 6–8 au, which has been attributed to CO_2 sublimation (Meech et al., 2017b). The surge sometimes observed in dynamically new comets does not appear to be as strong, perhaps because so much of the solar insolation is going into CO sublimation causing the change in brightness to be less noticeable.

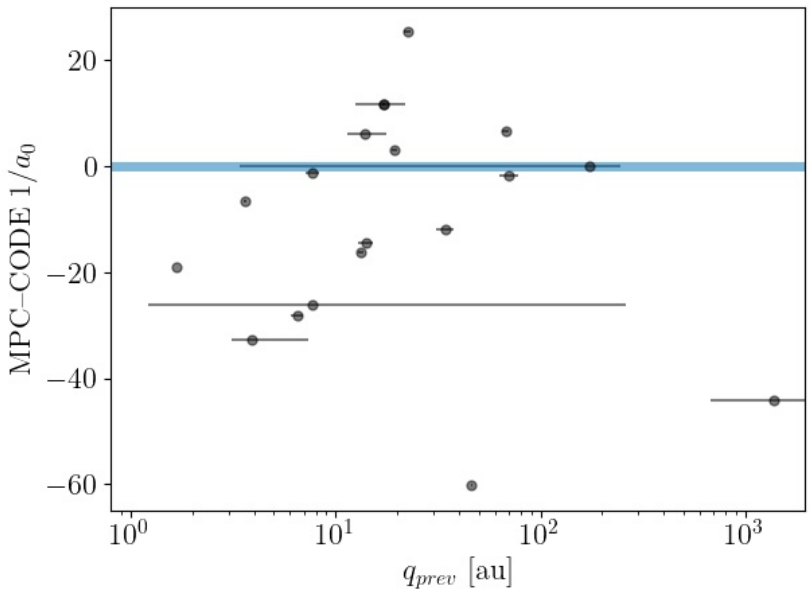

Figure 4.15: Difference between CODE and MPC $1/a_0 \times 10^6$ values with q_{prev}. The blue line highlighting 0 represents when both $1/a_0$ values are equal. Most points are below the line, suggesting the MPC values are usually lower than the CODE values.

4.6.3 Dynamical Considerations

As discussed in Section 1.4.1 and Section 4.4, the implementation of nongravitational effects is essential for accurate derivations of $1/a_0$. Our sample consists of frequently observed comets that, therefore, have well-determined orbits. MPC $1/a_0$ values are generally lower than the CODE values (Figure 4.15), a known bias direction when not considering nongravitational effects (Marsden et al., 1978; Królikowska & Dybczyński, 2010).

q_{prev} provides a better interpretation of prior solar heating, since $1/a_0$ and q_{prev} are somewhat correlated (Figure 4.16), but not exact (Dybczyński & Królikowska, 2015). Our early results show that it may be a better predictor of brightness behavior (Figure 4.14); however, more data is needed to confirm. The derivation of q_{prev} requires the implementation of galactic tides and stellar perturbers in the orbital models. The developers of CODE

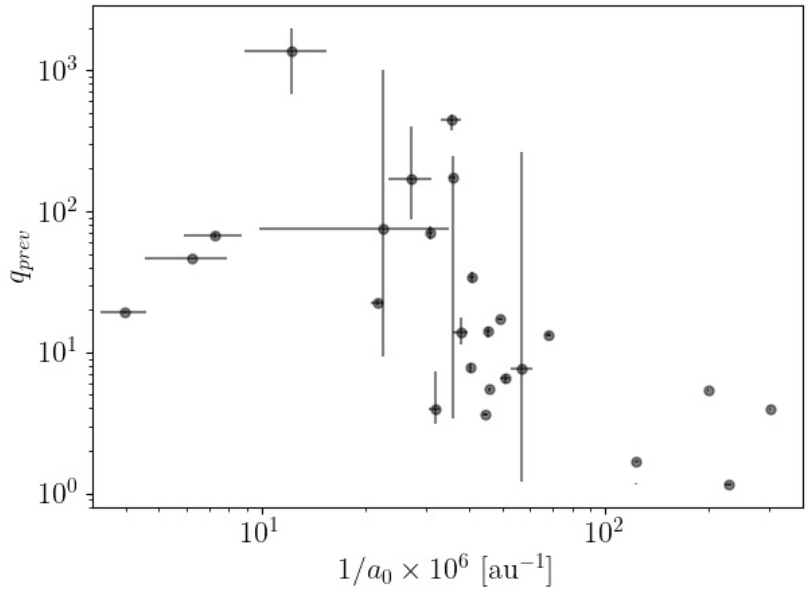

Figure 4.16: Relationship between $1/a_0$ and q_{prev}. We find a correlation where a higher $1/a_0$ has a smaller q_{prev} but the correlation is not very tight. Even if $1/a_0$ is accurately known, it cannot give us an exact q_{prev}. This is seen more clearly in Królikowska & Dybczyński (2017) Figure 13.

are some of the few researchers that attempt to determine q_{prev} and they are continuously updating their catalog of stellar perturbers (Dybczyński & Królikowska, 2022; Dybczyński & Breiter, 2022).

Observations can potentially be used to constrain dynamical models. For example, if all "surges" have a q_{prev} beyond the water snow line, for a comet that exhibits that behavior, we could eliminate the models that suggest the comet is dynamically old. However, an investigation into the brightness behavior of comets with multiple models in CODE is outside the scope of this chapter. When LSST comes online, more distant comets will be discovered, increasing our ability to monitor over longer data arcs and at heliocentric distances where nongravitational effects are less important, increasing the accuracy of original orbits. Nevertheless, a large astrometric data arc is required to determine the original orbits with

or without nongravitational accelerations, so q_{prev} will likely not be reliable early enough to use to predict future activity.

4.6.4 Leveraging Amateur Data

As equipment and software become more accessible, amateur observations of comets are becoming more and more frequent and therefore capable of filling in observation gaps between professional surveys for long-term monitoring. In the comet community, communication between professionals and amateurs is frequent via online mailing lists. It is clear that collaboration is desired on all sides. At the ProAm Comet Workshop in Prague in 2022 (Usher et al., 2022), a major topic was "what should amateurs do to make their observations better for professionals?". Based on the science goals described in this chapter, I will outline methods that observers can use to best contribute to the long-term monitoring of LPCs.

The easiest way to minimize observer bias in reported magnitudes is for all observers to utilize a standard processing pipeline. The easiest way to do this is to develop software designed for this purpose. The software must be easily accessible with minimal barriers to entry. Most software today uses a dynamic aperture size, which chooses an aperture size based on the size of the coma. This allows the majority of the coma to be included in the aperture with minimum background noise. However, each software does this slightly differently. A better solution would be to include multiple apertures and corresponding magnitudes for each submission. This process should be relatively simple with photometry software. Standardized software would also enable a uniform determination of magnitude

error, which can be a useful initial metric for data quality. Most submissions of CCD magnitudes today do not include magnitude error.

Standardization of reduction techniques seems to be the best way to remove most of the observer bias. However, achieving a standardization routine that caters to every observer, comet, and science goal is impractical. To fully utilize amateur observations, professional astronomers can benefit greatly from a database of raw images. With access to raw images, researchers can process the data using standardized methods that are suitable for the specific comet or scientific objectives. Gardener et al. (2022) employed this approach by creating a pipeline to calibrate and conduct photometry on images of 67P obtained from various facilities. Currently, a collaborative effort between COBS and the Pro-Am community is underway to develop an accessible database of raw CCD images geared towards submissions from amateur astronomers (Helen Usher, 2023, private communication).

In the upcoming LSST era, a large influx of discoveries will require follow-up observations at a rate too large for the number of professional observatories. Therefore, follow-up from amateurs will become increasingly important. A method that enables quality, standard submissions of amateur observations must be developed before LSST begins in ∼2025. Fortunately, the development of such a method is one of the projects I will be working on during my postdoc position preparing for LSST.

4.7 Summary

Archived cometary magnitudes from amateur observers are a relatively untapped dataset. However, the scatter in the data relating to observer bias can be too much to

accurately characterize lightcurves. Submission of CCD magnitudes is becoming increasingly popular with the potential of reducing the bias between observers. After investigating the reported variables, we find observer bias to be the main contributor to scatter, even with CCD observations. However, ICQSplitter (Womack et al., 2021) works well with both CCD and visual data to correct the observer bias and minimize scatter. We suggest that a database of raw files, rather than magnitudes, would be the most helpful solution so that individual astronomers can process the images in a uniform way that works best for their science goals.

The CODE catalog provides the previous orbital parameters for Oort spike comets using robust dynamical modeling that includes nongravitational accelerations, as well as galactic tides and stellar perturbers. After applying ICQSplitter to a subset of COBS comets that are modeled in CODE and also have sufficient data, we investigated how the brightness behavior compares to dynamical age. We find:

1. an overall decrease in brightening rate with decreasing heliocentric distance, suggesting the uniform activity index that is currently used to predict brightness behavior may not be the best method.

2. a wide distribution of activity indices pre-perihelion likely caused by the range of brightening behaviors, such as "surges" (e.g., C/2002 T7) and shallow brightening rates of distant objects (e.g., C/2017 K2).

3. a smaller distribution of activity indices near $n \sim 4$ post-perihelion, which has been attributed to the build-up of a dust mantle post-perihelion that is likely a similar process for all comets.

4. comets with $q_{prev} > 40$ au exhibited a shallow increase in brightness starting $r_h > 5$ au, suggesting they are the most pristine of the sample with CO sublimation driving activity causing a rapid increase in brightness much further from the Sun. These objects (we call dynamically new comets) with $q < 1$ au are more likely to disintegrate than other dynamical types.

5. a group of comets we classify as dynamically "in-between" that have experienced the sublimation of hypervolatiles such as CO and/or CO_2 during their previous solar passage but did not reach perihelion distances within the regime of water-ice sublimation. The previous passage caused the upper layers to be depleted in CO resulting in a lower observed CO/CO_2 ratio compared to the other classes. This group experiences a more dramatic surge in activity near $r_h \sim 3$ au than dynamically new comets, likely caused by the initiation of water-ice sublimation for the first time.

6. q_{prev} can be used as a more accurate predictor of brightness behavior compared to $1/a_0$, but building the data arc required to determine the previous orbit takes too long for this method to be used for predictions.

7. More comets covering a wider range of heliocentric distances are needed to confirm these findings. The upcoming LSST survey may greatly contribute to the number of distant comets we discover allowing for longer data arcs.

Chapter 5: Conclusions & Future Work

Most scientific endeavors are forever ongoing and such is the case with the work presented in this thesis; it is only the beginning. Below, I summarize our conclusions for each chapter, followed by a description of upcoming projects and observations.

5.1 Summary of Results

In Chapter 2, we obtained magnitude and optical color measurements of 22 near-Sun asteroids with $q \leq 0.15$ au over three years from January 2017 to March 2020 primarily using various 4-m class telescopes. These objects were studied to search for trends relating to surface modification due to near-Sun processes, particularly those that might lead to disruption. We found that the observed near-Sun asteroids exhibit bluer colors overall, suggesting these objects are being resurfaced to a higher degree. However, unknown dynamical histories and compositions for individual objects combined with competing surface-altering processes make constraining the primary resurfacing mechanisms difficult.

Chapter 3 utilized LCO's network of 1-m telescopes and SDSS g and r filters to create a frequent and long-term dataset, which we used to characterize the brightness evolution, colors, and coma morphology of 18 distant long-period comets. We found that the brightening rate decreased with decreasing heliocentric distance for all inbound comets,

motivating the establishment of a dynamic model for brightness prediction compared to the constant value used today. Based on a limited number of objects, we find evidence that returning LPCs experience the surge in activity associated with the activation of water closer to the Sun than DNCs, suggesting the upper layers of returning comets are more depleted of water-ice, likely from a prior solar passage.

Finally, Chapter 4 compared the brightness behavior of 27 LPCs determined from magnitudes collected by amateur astronomers with high-quality orbital models that detail the dynamical history of each comet. We found that the brightness behavior is related to the degree of prior heating and introduce a dynamically in-between category of LPCs that have experienced CO/CO_2 sublimation, but not water-ice sublimation. These objects likely have upper surface layers depleted of CO, resulting in a more dramatic surge in activity when water sublimation becomes significant.

5.2 Future Work

5.2.1 Ongoing Projects

The LOOK Project discussed in Chapter 3 has been extended through July 2024, enabling the lengthening of heliocentric distance baselines and the addition of new comets to our study. We anticipate adding ∼15–20 more objects to the objects included in Chapter 3, creating a large enough sample to conduct statistical tests. Furthermore, extended observations can improve the dynamical models used to estimate dynamical age.

We also plan to expand the parameter space of our long-term monitoring of distant comets described in Chapter 3, by incorporating comets discovered at even further distances

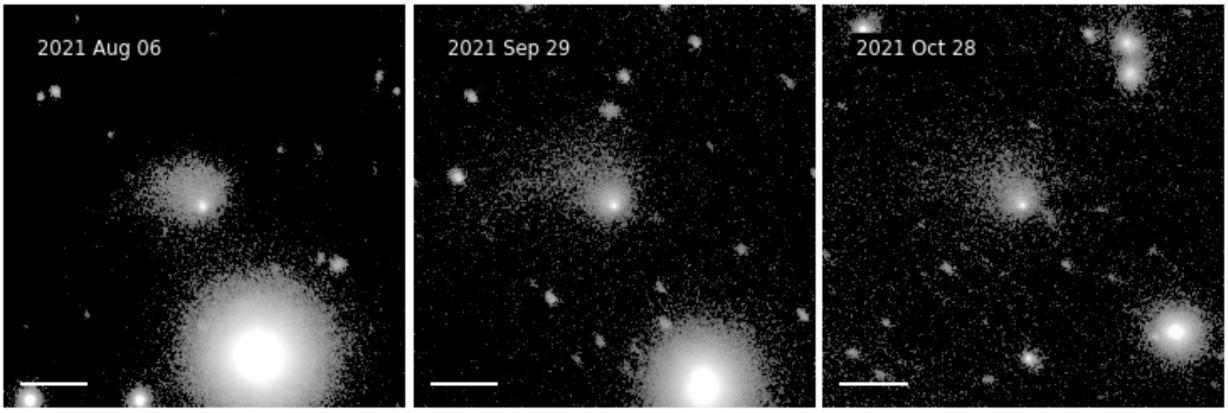

Figure 5.1: Coma morphology evolution of comet C/2014 UN_{271}. Each image in the panel is a median-combined r image from the 4.1-m SOAR telescope from each night. The white bar in the corner of each image represents 100,000 km. The morphology shows clear changes on monthly timescales.

($r_h \gtrsim 10$ au). We have been monitoring eight such comets beginning February 2021 using the 4.1-m SOAR telescope in Chile on ∼monthly timescales, including comet C/2014 UN_{271} (Bernardinelli-Bernstein; Figure 5.1). With this study we will be able to further examine the drivers of distant activity and assess how the brightness behavior of more distant objects relates to the LOOK objects.

5.2.2 JWST

Commissioned in 2022, JWST is the only telescope capable of directly detecting the major volatile drivers of activity (e.g., CO, CO_2, H_2O) for LPCs beyond 4 au from the Sun (Kelley et al., 2016). A robust infrared survey that monitors the activity across the different sublimation regimes in coordination with optical surveys would allow us to constrain how different volatile species affect the brightness behavior seen in the optical.

5.2.3 Vera Rubin Observatory's Legacy Survey of Space and Time (LSST)

With a limiting magnitude of 24.5 (in the r-band), the forthcoming Legacy Survey of Space and Time (LSST) at the Vera Rubin Observatory is projected to detect LPCs at significantly greater heliocentric distances than previously observed, potentially reaching distances beyond 20 au from the Sun regularly. A newly identified comet is likely to be observed approximately 50 times throughout its orbital path, allowing for detailed investigations of its activity as a function of its distance from the Sun. Over the initial decade, LSST is expected to discover around 10,000 comets (Solontoi, 2010), thereby providing a substantially larger sample size for long-period comets.

Such a large amount of data cannot be processed on a case-by-case basis but must be analyzed algorithmically. The studies described in this thesis will be used to prepare algorithms to process the incoming LSST data. LOOK data in particular will be used to simulate the survey cadence and test automated characterization pipelines.

The large dataset will also require a large-scale, semi-automatic schema for follow-up observations of newly discovered and interesting comets. Automated observing management platforms, like the ones used during my time in graduate school, such as NEOexchange and AEON, will be implemented at even more facilities, greatly enhancing follow-up capabilities. Additionally, the LSST Solar System Science Collaboration (SSSC) plans build a platform that can be used for communication and data-sharing between observers conducting follow-up, which includes maintaining a productive collaboration with amateurs.

5.2.4 Comet Interceptor

The Comet Interceptor mission is a pioneering space mission selected by the European Space Agency (ESA) that aims to study a pristine comet for the first time by targeting a dynamically new comet or interstellar object as it makes its first approach to the inner Solar System (Snodgrass & Jones, 2019). To do this, it will employ a novel approach where the mission will be designed and launched before its target is discovered. Comet Interceptor will wait in a parking orbit around the Sun-Earth L2 point, where it can station-keep with very little fuel consumption until a reachable target is found. The spacecraft will depart L2 to encounter the comet following a cruise period of up to 3 years. The mission is dependent on proper characterization of potential targets at large heliocentric distances and the work started in this thesis contributes to that goal. By investigating the surface composition, shape, and structure of a pristine nucleus and coma, the Comet Interceptor mission has the potential to unlock crucial insights into the early Solar System's composition, dynamics, and the processes involved in the formation and evolution of Oort cloud comets

Appendix A: Facilities and Software used in this Thesis

A.1 Facilities

1. 4.1–m Isaac Newton Telescope (INT): Wide Field Camera (WFC). *La Palma, Spain.*
2. Las Cumbres Observatory (LCO) 1–m: Sinistro.
3. 4.3–m Lowell Discovery Telescope (LDT): Large Monolithic Imager (LMI). *Happy Jack, AZ, USA.*
4. Lowell Observatory Hall 42–inch: NASA42 Camera. *Flagstaff, AZ, USA.*
5. Lowell Observatory 31–inch: NASAcam. *Flagstaff, AZ, USA.*
6. 4.1–m Southern Astrophysical Research (SOAR): Goodman High Throughput Spectrograph (GHTS). *Cerro Pachón, Chile.*
7. 4.1–m Southern Astrophysical Research (SOAR): SOAR Optical Imager (SOI). *Cerro Pachón, Chile. multiple sites.*

A.2 Software

1. `astropy` (Astropy Collaboration et al., 2018)
2. `astroquery` (Ginsburg et al., 2019)

3. `calviavat` (Kelley & Lister, 2022)

4. `ccdproc` (Craig et al., 2017)

5. COBS (Zakrajsek & Mikuz, 2018)

6. JPL Horizons*

7. NEOPOP† (Granvik et al., 2018)

8. `PHOTOMETRYPIPELINE` (Mommert, 2017)

9. `photutils` (Bradley et al., 2021)

10. `sbpy` (Mommert et al., 2019)

11. `SciPy` (Gommers et al., 2023)

12. `seaborn` (Waskom, 2021)

*https://ssd.jpl.nasa.gov/horizons/
†https://neo.ssa.esa.int/neo-population-generator

Bibliography

A'Hearn, M. F., Belton, M. J. S., Delamere, W. A., Feaga, L. M., Hampton, D., Kissel, J., Klaasen, K. P., McFadden, L. A., Meech, K. J., Melosh, H. J., Schultz, P. H., Sunshine, J. M., Thomas, P. C., Veverka, J., Wellnitz, D. D., Yeomans, D. K., Besse, S., Bodewits, D., Bowling, T. J., Carcich, B. T., Collins, S. M., Farnham, T. L., Groussin, O., Hermalyn, B., Kelley, M. S., Kelley, M. S., Li, J.-Y., Lindler, D. J., Lisse, C. M., McLaughlin, S. A., Merlin, F., Protopapa, S., Richardson, J. E., Williams, J. L. EPOXI at Comet Hartley 2. Science. 2011. 332 1396–1400.

A'Hearn, M. F., Millis, R. L., Schleicher, D. G., Osip, D. J., Birch, P. V. The Ensemble Properties of Comets: Results from Narrowband Photometry of 85 Comets, 1976-1992. Icarus. 1995. 118 223–270.

A'Hearn, M. F., Schleicher, D. G., Millis, R. L., Feldman, P. D., Thompson, D. T. Comet Bowell 1980b. AJ. 1984. 89 579–591.

Africano, B. M., Caselli, C., Korlevic, K., Buzzi, L., Novichonok, A., Sato, H., Baransky, A., Weryk, R., Laux, U., Stecklum, B., Ludwig, F., Hoegner, C., Bacci, P., Maestripieri, M., Tesi, L., Fagioli, G., Mikuz, H., Gajdos, S., Coffano, A., Marinello, W., Micheli, M., Pizzetti, G., Soffiantini, A., Haver, R., Gorelli, R., Foglia, S., Galli, G., Tichy, M., Ticha, J., Camilleri, P., Oey, J., Groom, R., Stranger, K., Calcagno, M., Fumagalli, A., Sicoli, P., Testa, A., Mastaler, R. A., Ries, J. G., Durig, D. T., Babcock, A. B., Turrentine, A. L., Yates, J. E., Emmerich, M., Melchert, S., Jaeger, M., Prosperi, E., Prosperi, S., Vollmann, W., Lindner, P., Dangl, G., Mantero, A., Ruocco, N., Jahn, J., Zhao, H. B., Li, B., Zhaori, G., Hong, R. Q., Hu, L. F., Lu, H., Bulger, J., Chambers, K., Lowe, T., Magnier, E., Schultz, A., Willman, M., Chastel, S., Huber, M., Ramanjooloo, Y., Wainscoat, R., de Boer, T., Denneau, L., Fairlamb, J., Flewelling, H., Lin, C. C., Lutkenhoner, B., Christensen, E. J., Farneth, G. A., Fuls, D. C., Gibbs, A. R., Grauer, A. D., Groeller, H., Kowalski, R. A., Larson, S. M., Leonard, G. J., Pruyne, T. A., Seaman, R. L., Shelly, F. C., Tilley, S. M., Masek, M., Losse, F., Gonzalez, J., Baj, G., Luna, V., Adamovsky, M., Pascoli Observatory, G., Bacci, R., Grazzini, L., Tombelli, M., Haeusler, B., Vinko, J., Sarneczky, K., Segon, D., Matkovic, F., Kervina, G., Valentine, F., Glavas, E., Hudin, L., Leonelli, L., Leonelli, A., Punzo, P., Alboresi, D., Valvasori, A., Soulier, J. F., Urakawa, S., Nimura, T., Ikemura, T., Tonry, J., Heinze, A., Weiland, H., Stalder, B., Fitzsimmons, A., Young, D., Erasmus, N., Wells,

G., Bamberger, D., Williams, G. V. COMET C/2019 F1 (ATLAS-Africano). Minor Planet Electronic Circulars. 2019. 2019-G124.

Astropy Collaboration, , Price-Whelan, A. M., Sipőcz, B. M., Günther, H. M., Lim, P. L., Crawford, S. M., Conseil, S., Shupe, D. L., Craig, M. W., Dencheva, N., Ginsburg, A., Vand erPlas, J. T., Bradley, L. D., Pérez-Suárez, D., de Val-Borro, M., Aldcroft, T. L., Cruz, K. L., Robitaille, T. P., Tollerud, E. J., Ardelean, C., Babej, T., Bach, Y. P., Bachetti, M., Bakanov, A. V., Bamford, S. P., Barentsen, G., Barmby, P., Baumbach, A., Berry, K. L., Biscani, F., Boquien, M., Bostroem, K. A., Bouma, L. G., Brammer, G. B., Bray, E. M., Breytenbach, H., Buddelmeijer, H., Burke, D. J., Calderone, G., Cano Rodríguez, J. L., Cara, M., Cardoso, J. V. M., Cheedella, S., Copin, Y., Corrales, L., Crichton, D., D'Avella, D., Deil, C., Depagne, É., Dietrich, J. P., Donath, A., Droettboom, M., Earl, N., Erben, T., Fabbro, S., Ferreira, L. A., Finethy, T., Fox, R. T., Garrison, L. H., Gibbons, S. L. J., Goldstein, D. A., Gommers, R., Greco, J. P., Greenfield, P., Groener, A. M., Grollier, F., Hagen, A., Hirst, P., Homeier, D., Horton, A. J., Hosseinzadeh, G., Hu, L., Hunkeler, J. S., Ivezić, Ž., Jain, A., Jenness, T., Kanarek, G., Kendrew, S., Kern, N. S., Kerzendorf, W. E., Khvalko, A., King, J., Kirkby, D., Kulkarni, A. M., Kumar, A., Lee, A., Lenz, D., Littlefair, S. P., Ma, Z., Macleod, D. M., Mastropietro, M., McCully, C., Montagnac, S., Morris, B. M., Mueller, M., Mumford, S. J., Muna, D., Murphy, N. A., Nelson, S., Nguyen, G. H., Ninan, J. P., Nöthe, M., Ogaz, S., Oh, S., Parejko, J. K., Parley, N., Pascual, S., Patil, R., Patil, A. A., Plunkett, A. L., Prochaska, J. X., Rastogi, T., Reddy Janga, V., Sabater, J., Sakurikar, P., Seifert, M., Sherbert, L. E., Sherwood-Taylor, H., Shih, A. Y., Sick, J., Silbiger, M. T., Singanamalla, S., Singer, L. P., Sladen, P. H., Sooley, K. A., Sornarajah, S., Streicher, O., Teuben, P., Thomas, S. W., Tremblay, G. R., Turner, J. E. H., Terrón, V., van Kerkwijk, M. H., de la Vega, A., Watkins, L. L., Weaver, B. A., Whitmore, J. B., Woillez, J., Zabalza, V., Astropy Contributors, . The Astropy Project: Building an Open-science Project and Status of the v2.0 Core Package. AJ. 2018. 156, 3 123.

Bailey, M. E., Chambers, J. E., Hahn, G. Origin of Sungrazers - A Frequent Cometary End-State. A&A. 1992. 257 315–322.

Bertin, E. Automatic Astrometric and Photometric Calibration with SCAMP. Astronomical Data Analysis Software and Systems XV. 351. 2006. 112. (Astronomical Society of the Pacific Conference Series).

Bertin, E., Arnouts, S. SExtractor: Software for source extraction. A&AS. 1996. 117 393–404.

Bessell, M. S. Standard Photometric Systems. ARA&A. 2005. 43, 1 293–336.

Binzel, R. P., DeMeo, F. E., Turtelboom, E. V., Bus, S. J., Tokunaga, A., Burbine, T. H., Lantz, C., Polishook, D., Carry, B., Morbidelli, A., Birlan, M., Vernazza, P., Burt, B. J., Moskovitz, N., Slivan, S. M., Thomas, C. A., Rivkin, A. S., Hicks, M. D., Dunn, T., Reddy, V., Sanchez, J. A., Granvik, M., Kohout, T. Compositional distributions

and evolutionary processes for the near-Earth object population: Results from the MIT-Hawaii Near-Earth Object Spectroscopic Survey (MITHNEOS). Icarus. 2019. 324 41–76.

Binzel, R. P., Morbidelli, A., Merouane, S., DeMeo, F. E., Birlan, M., Vernazza, P., Thomas, C. A., Rivkin, A. S., Bus, S. J., Tokunaga, A. T. Earth encounters as the origin of fresh surfaces on near-Earth asteroids. Nature. 2010. 463 331–334.

Binzel, R. P., Harris, A. W., Bus, S. J., Burbine, T. H. Spectral Properties of Near-Earth Objects: Palomar and IRTF Results for 48 Objects Including Spacecraft Targets (9969) Braille and (10302) 1989 ML. Icarus. 2001. 151, 2 139–149.

Binzel, R. P., Rivkin, A. S., Stuart, J. S., Harris, A. W., Bus, S. J., Burbine, T. H. Observed spectral properties of near-Earth objects: results for population distribution, source regions, and space weathering processes. Icarus. 2004. 170, 2 259–294.

Bockelée-Morvan, D., Biver, N., Moreno, R., Colom, P., Crovisier, J., Gérard, É., Henry, F., Lis, D. C., Matthews, H., Weaver, H. A., Womack, M., Festou, M. C. Outgassing Behavior and Composition of Comet C/1999 S4 (LINEAR) During Its Disruption. Science. 2001. 292 1339–1343.

Bolin, B. T., Lin, Z. Y., Masci, F. J., Sharma, K., Kumar, H., Bhalerao, V. Comet C/2021 e3 (ztf). Minor Planet Electronic Circulars. 2021. J.

Bolin, B. T., Masci, F. J., Ip, W. H., Helou, G., Kramer, E. A., Lin, Z. Y., Prince, T. A., Sato, H., Paul, N., Yoshimoto, K., Urbanik, M., Denneau, L., Siverd, R., Tonry, J., Weiland, H., Erasmus, N., Fitzsimmons, A., Lawrence, A., Robinson, J., Siverd, R., Tonry, J., Birtwhistle, P., Jacques, C., Hug, G., Korlevic, K., Buzzi, L., Bacci, R., van Buitenen, G., Buczynski, D., Hale, A., Masek, M., Guido, E., Rocchetto, M., Bryssinck, E., Milani, G., Savini, G., Valvasori, A., Ligustri, R., Bacci, P., Maestripieri, M., Tesi, L., Fagioli, G., Lutkenhoner, B. Comet C/2022 E3 (ZTF). Minor Planet Electronic Circulars. 2022. 2022-F13.

Bortle, J. E. Post-Perihelion Survival of Comets with Small q. International Comet Quarterly. 1991. 13 89.

Bottke, J. William F., Vokrouhlický, D., Rubincam, D. P., Nesvorný, D. The Yarkovsky and Yorp Effects: Implications for Asteroid Dynamics. Annual Review of Earth and Planetary Sciences. 2006. 34 157–191.

Bottke, W. F., Morbidelli, A., Jedicke, R., Petit, J.-M., Levison, H. F., Michel, P., Metcalfe, T. S. Debiased Orbital and Absolute Magnitude Distribution of the Near-Earth Objects. Icarus. 2002. 156 399–433.

Bowell, E., Hapke, B., Domingue, D., Lumme, K., Peltoniemi, J., Harris, A. W. Application of Photometric Models to Asteroids. Asteroids II. 1989. 524–556.

Boyd, D. Pro-am collaboration in astronomy - past, present and future. Journal of the British Astronomical Association. 2011. 121 73–90.

Bradley, L., Sipőcz, B., Robitaille, T., Tollerud, E., Vinícius, Z., Deil, C., Barbary, K., Wilson, T. J., Busko, I., Donath, A., Günther, H. M., Cara, M., krachyon, , Conseil, S., Bostroem, A., Droettboom, M., Bray, E. M., Lim, P. L., Bratholm, L. A., Barentsen, G., Craig, M., Rathi, S., Pascual, S., Perren, G., Georgiev, I. Y., Val-Borro, M. de, Kerzendorf, W., Bach, Y. P., Quint, B., Souchereau, H. astropy/photutils: 1.2.0. 2021.

Bramich, D. M. A new algorithm for difference image analysis. MNRAS. 2008. 386 L77–L81.

Bramich, D. M., Horne, K., Albrow, M. D., Tsapras, Y., Snodgrass, C., Street, R. A., Hundertmark, M., Kains, N., Arellano Ferro, A., Figuera, J. R., Giridhar, S. Difference image analysis: extension to a spatially varying photometric scale factor and other considerations. MNRAS. 2013. 428, 3 2275–2289.

Brown, T. M., Baliber, N., Bianco, F. B., Bowman, M., Burleson, B., Conway, P., Crellin, M., Depagne, É., De Vera, J., Dilday, B., Dragomir, D., Dubberley, M., Eastman, J. D., Elphick, M., Falarski, M., Foale, S., Ford, M., Fulton, B. J., Garza, J., Gomez, E. L., Graham, M., Greene, R., Haldeman, B., Hawkins, E., Haworth, B., Haynes, R., Hidas, M., Hjelstrom, A. E., Howell, D. A., Hygelund, J., Lister, T. A., Lobdill, R., Martinez, J., Mullins, D. S., Norbury, M., Parrent, J., Paulson, R., Petry, D. L., Pickles, A., Posner, V., Rosing, W. E., Ross, R., Sand, D. J., Saunders, E. S., Shobbrook, J., Shporer, A., Street, R. A., Thomas, D., Tsapras, Y., Tufts, J. R., Valenti, S., Vander Horst, K., Walker, Z., White, G., Willis, M. Las Cumbres Observatory Global Telescope Network. PASP. 2013. 125, 931 1031.

Brunetto, R., Loeffler, M. J., Nesvorný, D., Sasaki, S., Strazzulla, G. Asteroid Surface Alteration by Space Weathering Processes. Asteroids IV, Patrick Michel, Francesca E. DeMeo, and William F. Bottke (eds.), University of Arizona Press, Tucson, 895 pp. ISBN: 978-0-816-53213-1, 2015., p.597-616. 2015. 597–616.

Brunetto, R., Strazzulla, G. Elastic collisions in ion irradiation experiments: A mechanism for space weathering of silicates. Icarus. 2005. 179, 1 265–273.

Brunetto, R., Vernazza, P., Marchi, S., Birlan, M., Fulchignoni, M., Orofino, V., Strazzulla, G. Modeling asteroid surfaces from observations and irradiation experiments: The case of 832 Karin. Icarus. 2006. 184, 2 327–337.

Bulger, J., Chambers, K., Lowe, T., Schultz, A., Smith, I., Chastel, S., Huber, M., Ramanjooloo, Y., Wainscoat, R., Weryk, R., de Boer, T., Fairlamb, J., Gao, H., Huber, M., Lin, C. C., Magnier, E., Armstrong, J. D., Sioulas, N., Sato, H., Hale, A., Bryssinck, E., Rocchetto, M., Guido, E., Fulle, M., Milani, G., Nassef, C., Savini, G., Valvasori, A., Micheli, M., Conversi, L., Petrescu, E., Fohring, D., Schwab, E., Koschny, D. Comet C/2021 s3 (panstarrs). Minor Planet Electronic Circulars. 2021. T.

Campins, H., Kelley, M. S., Fernández, Y., Licandro, J., Hargrove, K. Low Perihelion Near-Earth Asteroids. Earth Moon and Planets. 2009. 105 159–165.

Carbognani, A. Asteroids Lightcurves Analysis at OAVDA: 2016 January - October. Minor Planet Bulletin. 2017. 44, 1 52–57.

Carry, B., Solano, E., Eggl, S., DeMeo, F. E. Spectral properties of near-Earth and Mars-crossing asteroids using Sloan photometry. Icarus. 2016. 268 340–354.

Carusi, A., Kresak, L., Perozzi, E., Valsecchi, G. B. High-Order Librations of Halley-Type Comets. A&A. 1987. 187 899.

Carvano, J. M., Davalos, J. A. G. Shape and solar phase angle effects on the taxonomic classification of asteroids. A&A. 2015. 580 A98.

Chapman, C. R. Space Weathering of Asteroid Surfaces. Annual Review of Earth and Planetary Sciences. 2004. 32 539–567.

Clark, B. E., Hapke, B., Pieters, C., Britt, D. Asteroid Space Weathering and Regolith Evolution. Asteroids III, W. F. Bottke Jr., A. Cellino, P. Paolicchi, and R. P. Binzel (eds), University of Arizona Press, Tucson, p.585-599. 2002. 585–599.

Clark, B. E., Lucey, P., Helfenstein, P., Bell, I. J. F., Peterson, C., Veverka, J., McConnochie, T., Robinson, M. S., Bussey, B., Murchie, S. L., Izenberg, N. I., Chapman, C. R. Space weathering on Eros: Constraints from albedo and spectral measurements of Psyche crater. M&PS. 2001. 36, 12 1617–1637.

Clemens, J. C., Crain, J. A., Anderson, R. The Goodman spectrograph. Ground-based Instrumentation for Astronomy. 5492. 2004. 331–340. (Society of Photo-Optical Instrumentation Engineers (SPIE) Conference Series).

Cochran, A. L., Cochran, W. D. A High Spectral Resolution Atlas of Comet 122P/de Vico. Icarus. 2002. 157, 2 297–308.

Craig, M., Crawford, S., Seifert, M., Robitaille, T., Sipőcz, B., Walawender, J., Vinícius, Z., Ninan, J. P., Droettboom, M., Youn, J., Tollerud, E., Bray, E., Walker, N., Janga, V. R., Stotts, C., Günther, H. M., Rol, E., Bach, Y. P., Bradley, L., Deil, C., Price-Whelan, A., Barbary, K., Horton, A., Schoenell, W., Heidt, N., Gasdia, F., Nelson, S., Streicher, O. astropy/ccdproc: v1.3.0.post1. 2017.

Crovisier, J., Colom, P., Biver, N., Bockelée-Morvan, D., Boissier, J. Comet C/2021 A1 (Leonard). Central Bureau Electronic Telegrams. 2021. 5087.

Dandy, C. L., Fitzsimmons, A., Collander-Brown, S. J. Optical colors of 56 near-Earth objects: trends with size and orbit. Icarus. 2003. 163 363–373.

DeMeo, F. E., Carry, B. The taxonomic distribution of asteroids from multi-filter all-sky photometric surveys. Icarus. 2013. 226, 1 723–741.

DeMeo, F., Binzel, R. P. Comets in the near-Earth object population. Icarus. 2008. 194, 2 436–449.

DeMeo, F. E., Binzel, R. P., Lockhart, M. Mars encounters cause fresh surfaces on some near-Earth asteroids. Icarus. 2014. 227 112–122.

Delbó, M., Gayon-Markt, J., Busso, G., Brown, A., Galluccio, L., Ordenovic, C., Bendjoya, P., Tanga, P. Asteroid spectroscopy with Gaia. Planet. Space Sci. 2012. 73, 1 86–94.

Delbo, M., Libourel, G., Wilkerson, J., Murdoch, N., Michel, P., Ramesh, K. T., Ganino, C., Verati, C., Marchi, S. Thermal fatigue as the origin of regolith on small asteroids. Nature. 2014. 508, 7495 233–236.

Denneau, L., Siverd, R., Tonry, J., Weiland, H., Erasmus, N., Fitzsimmons, A., Lawrence, A., Robinson, J., Paul, N., Sato, H., Guido, E., Valli, E., Ventre, G., Sicoli, P., Drummond, J., Masek, M., Leonard, G. J., Christensen, E. J., Farneth, G. A., Fazekas, J. B., Fuls, D. C., Gibbs, A. R., Grauer, A. D., Groeller, H., Kowalski, R. A., Larson, S. M., Rankin, D., Seaman, R. L., Serrano, A., Shelly, F. C., Wierzchos, K. W., Ikemura, T., Romanov, F. D., Armstrong, J. D., Evans, A. J., Lutkenhoner, B., Maury, A., Attard, G., Fabrega, J., Parrott, D., Rocchetto, M., Bryssinck, E., Milani, G., Savini, G., Valvasori, A., Jacques, C. Comet C/2022 e2 (atlas). Minor Planet Electronic Circulars. 2022. 2022-E227.

Devogèle, M., Moskovitz, N., Thirouin, A., Gustaffson, A., Magnuson, M., Thomas, C., Willman, M., Christensen, E., Person, M., Binzel, R., Polishook, D., DeMeo, F., Hinkle, M., Trilling, D., Mommert, M., Burt, B., Skiff, B. Visible Spectroscopy from the Mission Accessible Near-Earth Object Survey (MANOS): Taxonomic Dependence on Asteroid Size. AJ. 2019. 158, 5 196.

Devyatkin, A. V., Gorshanov, D. L., Petrova, S. N., Martyusheva, A. A., L'vov, V. N., Tsekmeister, S. D. Astrometry and photometry of potentially hazardous asteroid (276033) 2002 AJ129. Planet. Space Sci. 2022. 213 105427.

Dybczyński, P. A. Dynamical history of the observed long-period comets. A&A. 2001. 375 643–650.

Dybczyński, P. A. Simulating observable comets. III. Real stellar perturbers of the Oort cloud and their output. A&A. 2006. 449, 3 1233–1242.

Dybczyński, P. A., Breiter, S. Galactic and stellar perturbations of long-period comet motion. Practical considerations. A&A. 2022. 657 A65.

Dybczyński, P. A., Królikowska, M. Near-parabolic comets observed in 2006-2010 - II. Their past and future motion under the influence of the Galaxy field and known nearby stars. MNRAS. 2015. 448, 1 588–600.

Dybczyński, P. A., Królikowska, M. Towards a better understanding of the apparent source/sources of long period comets. Planet. Space Sci. 2016. 123 77–86.

Dybczyński, P. A., Królikowska, M. The Influence Of Individual Stars On The long-Term Dynamics Of Comets C/2014 UN_{271} And C/2017 K2. A&A. 2022. 660 A100.

Eisner, N., Knight, M. M., Schleicher, D. G. The Rotation and Other Properties of Comet 49P/Arend-Rigaux, 1984-2012. AJ. 2017. 154 196.

Eisner, N. L., Knight, M. M., Snodgrass, C., Kelley, M. S. P., Fitzsimmons, A., Kokotanekova, R. Properties of the Bare Nucleus of Comet 96P/Machholz 1. AJ. 2019. 157, 5 186.

Faggi, S., Lippi, M., Mumma, M. J., Villanueva, G. L. Strongly Depleted Methanol and Hypervolatiles in Comet C/2021 A1 (Leonard): Signatures of Interstellar Chemistry? PSJ. 2023. 4, 1 8.

Farinella, P., Froeschle, C., Gonczi, R., Hahn, G., Morbidelli, A., Valsecchi, G. B. Asteroids Falling Into the Sun. Nature. 1994. 371 314–317.

Farnham, T. L., Schleicher, D. G., A'Hearn, M. F. The HB Narrowband Comet Filters: Standard Stars and Calibrations. Icarus. 2000. 147 180–204.

Farnham, T. L., Schleicher, D. G., Woodney, L. M., Birch, P. V., Eberhardy, C. A., Levy, L. Imaging and Photometry of Comet C/1999 S4 (LINEAR) Before Perihelion and After Breakup. Science. 2001. 292 1348–1354.

Fernández, Y. R., Lowry, S. C., Weissman, P. R., Mueller, B. E. A., Samarasinha, N. H., Belton, M. J. S., Meech, K. J. New Near-Aphelion Light Curves of Comet 2P/Encke. Icarus. 2005. 175 194–214.

Fitzsimmons, A., Denneau, L., Siverd, R., Tonry, J., Weiland, H., Erasmus, N., Lawrence, A., Robinson, J., Camarasa, J., Birtwhistle, P., Sato, H., Valvasori, A., Guido, E., Paul, N., Bryssinck, E., Bacci, P., Maestripieri, M., Grazia, M. D., Tesi, L., Fagioli, G., Gajdos, S., Coffano, A., Marinello, W., Micheli, M., Pizzetti, G., Soffiantini, A., Foglia, S., Galli, G., Buzzi, L., Aletti, A., Pettarin, E., Romanov, F. D., Masek, M., Kugel, F., Duszanowicz, G., Koch, B., Diepvens, A., Lindner, P., Ruocco, N., Zhao, H. B., Li, B., Zhaori, G., Hong, R. Q., Hu, L. F., Lu, H., Xu, Z. J., Ji, Z. W., Urbanik, M., Attard, G., De Pieri, A., Felber, T., Mattiazzo, M., Losse, F., Baj, G., Campestrin, M., Gerhard, C., Tombelli, M., Squilloni, A., Venticinque, E., Mazzanti, A., Brandi, L., Fieramosca, G., Alasia, C., Grazzini, L., Bitossi, T., Interrante, G., Morelli, S., Bernardi, F., Haeusler, B., Sarneczky, K., Korlevic, K., Catapano, A., Flynn, R. L., Maikner, J., Rocchetto, M., Fulle, M., Milani, G., Savini, G., Wells, G., Mickleburgh, A. Comet C/2022 L2 (ATLAS). Minor Planet Electronic Circulars. 2022. 2022-M18.

Fukugita, M., Ichikawa, T., Gunn, J. E., Doi, M., Shimasaku, K., Schneider, D. P. The Sloan Digital Sky Survey Photometric System. AJ. 1996. 111 1748–+.

Gaffey, M. J. Space weathering and the interpretation of asteroid reflectance spectra. Icarus. 2010. 209, 2 564–574.

Gardener, D., Snodgrass, C., Jehin, E. A TRAPPIST Survey of the Activity of 14 Comets. Asteroids, Comets, Meteors 2023. 2023.

Gardener, D., Snodgrass, C., Ligier, N. Searching for outbursts in the ground-based photometry of 67P/Churyumov-Gerasimenko. MNRAS. 2022. 517, 3 4305–4316.

Ginsburg, A., Sipőcz, B. M., Brasseur, C. E., Cowperthwaite, P. S., Craig, M. W., Deil, C., Guillochon, J., Guzman, G., Liedtke, S., Lian Lim, P., Lockhart, K. E., Mommert, M., Morris, B. M., Norman, H., Parikh, M., Persson, M. V., Robitaille, T. P., Segovia, J.-C., Singer, L. P., Tollerud, E. J., de Val-Borro, M., Valtchanov, I., Woillez, J., Astroquery Collaboration, , a subset of astropy Collaboration, . astroquery: An Astronomical Web-querying Package in Python. AJ. 2019. 157, 3 98.

Gladman, B. J., Migliorini, F., Morbidelli, A., Zappala, V., Michel, P., Cellino, A., Froeschle, C., Levison, H. F., Bailey, M., Duncan, M. Dynamical lifetimes of objects injected into asteroid belt resonances. Science. 1997. 277 197–201.

Gomes, R., Levison, H. F., Tsiganis, K., Morbidelli, A. Origin of the cataclysmic Late Heavy Bombardment period of the terrestrial planets. Nature. 2005. 435 466–469.

Gommers, R., Virtanen, P., Burovski, E., Haberland, M., Weckesser, W., Oliphant, T. E., Reddy, T., Cournapeau, D., Alexbrc, , Nelson, A., Peterson, P., Wilson, J., Roy, P., Endolith, , Polat, I., Mayorov, N., Van Der Walt, S., Brett, M., Laxalde, D., Larson, E., Millman, J., Sakai, A., Lars, , Peterbell10, , Van Mulbregt, P., Carey, C., Eric-Jones, , McKibben, N., Kai, , Kern, R. scipy/scipy: SciPy 1.10.1. 2023.

Granvik, M., Morbidelli, A., Jedicke, R., Bolin, B., Bottke, W. F., Beshore, E., Vokrouhlický, D., Delbò, M., Michel, P. Super-catastrophic disruption of asteroids at small perihelion distances. Nature. 2016. 530 303–306.

Granvik, M., Brown, P. Identification of meteorite source regions in the Solar System. Icarus. 2018. 311 271–287.

Granvik, M., Morbidelli, A., Jedicke, R., Bolin, B., Bottke, W. F., Beshore, E., Vokrouhlický, D., Nesvorný, D., Michel, P. Debiased orbit and absolute-magnitude distributions for near-Earth objects. Icarus. 2018. 312 181–207.

Granvik, M., Morbidelli, A., Vokrouhlický, D., Bottke, W. F., Nesvorný, D., Jedicke, R. Escape of asteroids from the main belt. A&A. 2017. 598 A52.

Graves, K. J., Minton, D. A., Hirabayashi, M., DeMeo, F. E., Carry, B. Resurfacing asteroids from YORP spin-up and failure. Icarus. 2018. 304 162–171.

Graves, K. J., Minton, D. A., Molaro, J. L., Hirabayashi, M. Resurfacing asteroids from thermally induced surface degradation. Icarus. 2019. 322 1–12.

Green, D. W. E. The ICQ Guide to Observing Comets. International Comet Quarterly. 1997. 8.

Green, D. W., Rokoske, T. L., Morris, C. S. The ICQ photometric archive for P/Halley and other comets. ESLAB Symposium on the Exploration of Halley's Comet. 250. 1986. 249–251. (ESA Special Publication).

Greenstreet, S., Ngo, H., Gladman, B. The orbital distribution of Near-Earth Objects inside Earth's orbit. Icarus. 2012. 217 355–366.

Gustafsson, A., Trilling, D. E., Mommert, M., McNeill, A., Hora, J. L., Smith, H. A., Hellmich, S., Mottola, S., Harris, A. W. Spitzer Albedos of Near-Earth Objects. AJ. 2019. 158, 2 67.

Hapke, B. Space weathering from Mercury to the asteroid belt. J. Geophys. Res. 2001. 106, E5 10039–10074.

Harrington Pinto, O., Womack, M., Fernandez, Y., Bauer, J. A Survey of CO, CO_2, and H_2O in Comets and Centaurs. PSJ. 2022. 3, 11 247.

Harris, A. W. A Thermal Model for Near-Earth Asteroids. Icarus. 1998. 131 291–301.

Herman, G., Podolak, M. Numerical simulation of comet nuclei I. Water-ice comets. Icarus. 1985. 61, 2 252–266.

Holt, C. E., Knight, M. M., Kelley, M. S. P., Ye, Q., Hsieh, H. H., Snodgrass, C., Fitzsimmons, A., Richardson, D. C., Sunshine, J. M., Eisner, N. L., Gustaffson, A. Surface Properties of Near-Sun Asteroids. PSJ. 2022a. 3, 8 187.

Holt, C. E., Knight, M. M., Lister, T., Kelley, M. S. P., Ye, Q., Snodgrass, C., Opitom, C., Kokotanekova, R., Protopapa, S., Micheli, M., Schwamb, M. Monitoring the activity of distant comets. AAS/Division for Planetary Sciences Meeting Abstracts. 54. 2022b. 101.06. (AAS/Division for Planetary Sciences Meeting Abstracts).

Howell, S. B. Two-Dimensional Aperture Photometry: Signal-to-Noise Ratio of Point-Source Observations and Optimal Data-Extraction Techniques. PASP. 1989. 101 616.

Hsieh, H. H., Fitzsimmons, A., Novaković, B., Denneau, L., Heinze, A. N. The transient Jupiter Trojan-like orbit of P/2019 LD_2 (ATLAS). Icarus. 2021. 354 114019.

Hui, M.-T. Observations of Comet P/2003 T12 = 2012 A3 (SOHO) at large phase angle in STEREO-B. MNRAS. 2013. 436 1564–1575.

Hui, M.-T., Li, J. Resurrection of (3200) Phaethon in 2016. AJ. 2017. 153 23.

Hui, M.-T., Knight, M. M. New Insights into Interstellar Object 1I/2017 U1 ('Oumuamua) from SOHO/STEREO Nondetections. AJ. 2019. 158, 6 256.

Hui, M.-T., Tholen, D. J., Kracht, R., Chang, C.-K., Wiegert, P. A., Ye, Q.-Z., Mutchler, M. The Lingering Death of Periodic Near-Sun Comet 323P/SOHO. AJ. 2022. 164, 1 1.

Ivezic, Z., Juric, M., Lupton, R. H., Tabachnik, S., Quinn, T. Asteroids Observed by The Sloan Digital Sky Survey. Survey and Other Telescope Technologies and Discoveries. 4836. 2002. 98–103. (Society of Photo-Optical Instrumentation Engineers (SPIE) Conference Series).

Ivezić, Ž., Tabachnik, S., Rafikov, R., Lupton, R. H., Quinn, T., Hammergren, M., Eyer, L., Chu, J., Armstrong, J. C., Fan, X., Finlator, K., Geballe, T. R., Gunn, J. E., Hennessy, G. S., Knapp, G. R., Leggett, S. K., Munn, J. A., Pier, J. R., Rockosi, C. M., Schneider, D. P., Strauss, M. A., Yanny, B., Brinkmann, J., Csabai, I., Hindsley, R. B., Kent, S., Lamb, D. Q., Margon, B., McKay, T. A., Smith, J. A., Waddel, P., York, D. G., SDSS Collaboration, . Solar System Objects Observed in the Sloan Digital Sky Survey Commissioning Data. AJ. 2001. 122, 5 2749–2784.

Jenniskens, P., Blake, D. F. Crystallization of Amorphous Water Ice in the Solar System. ApJ. 1996. 473 1104.

Jewitt, D. Properties of Near-Sun Asteroids. AJ. 2013. 145 133.

Jewitt, D. Color Systematics of Comets and Related Bodies. AJ. 2015. 150 201.

Jewitt, D., Li, J. Activity in Geminid Parent (3200) Phaethon. AJ. 2010. 140 1519–1527.

Jewitt, D. The Active Asteroids. AJ. 2012. 143, 3 66.

Jewitt, D., Kim, Y., Mattiazzo, M., Mutchler, M., Li, J., Agarwal, J. Disintegration of Long-period Comet C/2021 A1 (Leonard). AJ. 2023. 165, 3 122.

Jewitt, D., Kim, Y., Mutchler, M., Agarwal, J., Li, J., Weaver, H. Cometary Activity Begins at Kuiper Belt Distances: Evidence from C/2017 K2. AJ. 2021. 161, 4 188.

Jewitt, D., Li, J., Agarwal, J. THE DUST TAIL OF ASTEROID (3200) PHAETHON. The Astrophysical Journal. 2013. 771, 2 L36.

Johnson, R. E., Cooper, J. F., Lanzerotti, L. J., Strazzulla, G. Radiation Formation of a Non-Volatile Comet Crust. A&A. 1987. 187 889.

Jones, G. H., Knight, M. M., Battams, K., Boice, D. C., Brown, J., Giordano, S., Raymond, J., Snodgrass, C., Steckloff, J. K., Weissman, P., al., et. The Science of Sungrazers, Sunskirters, and Other Near-Sun Comets. Space Science Reviews. 2017. 214, 1 20.

Jones, R. L., Jurić, M., Ivezić, Ž. Asteroid Discovery and Characterization with the Large Synoptic Survey Telescope. Asteroids: New Observations, New Models. 318. 2016. 282–292.

Jordi, K., Grebel, E. K., Ammon, K. Empirical color transformations between SDSS photometry and other photometric systems. A&A. 2006. 460 339–347.

Kelley, M. S. P., Woodward, C. E., Bodewits, D., Farnham, T. L., Gudipati, M. S., Harker, D. E., Hines, D. C., Knight, M. M., Kolokolova, L., Li, A., de Pater, I., Protopapa, S., Russell, R. W., Sitko, M. L., Wooden, D. H. Cometary Science with the James Webb Space Telescope. PASP. 2016. 128, 1 018009.

Kelley, M. S. P., Kokotanekova, R., Holt, C. E., Protopapa, S., Bodewits, D., Knight, M. M., Lister, T., Usher, H., Chatelain, J., Gomez, E., Greenstreet, S., Angel, T., Wooding, B. A Look at Outbursts of Comet C/2014 UN_{271} (Bernardinelli-Bernstein) near 20 au. ApJL. 2022. 933, 2 L44.

Kelley, M. S. P., Lister, T. calviacat: Calibrate star photometry by catalog comparison. 2022. ascl:2207.015.

Kidger, M. R. The Breakup of C/1999 S4 (Linear), Days 0-10. Earth Moon and Planets. 2002. 90 157–165.

Knight, M. M., A'Hearn, M. F., Biesecker, D. A., Faury, G., Hamilton, D. P., Lamy, P., Llebaria, A. Photometric Study of the Kreutz Comets Observed by SOHO from 1996 to 2005. AJ. 2010. 139 926–949.

Knight, M. M., Battams, K. Preliminary Analysis of SOHO/STEREO Observations of Sungrazing Comet ISON (C/2012 S1) around Perihelion. ApJL. 2014. 782 L37 (5pp).

Knight, M. M., Farnham, T. L., Schleicher, D. G., Schwieterman, E. W. The Increasing Rotation Period of Comet 10P/Tempel 2. AJ. 2011. 141 2.

Knight, M. M., Fitzsimmons, A., Kelley, M. S. P., Snodgrass, C. Comet 322P/SOHO 1: An Asteroid with the Smallest Perihelion Distance? ApJL. 2016. 823 L6.

Knight, M. M., Holt, C. E., Villa, K. M., Skiff, B. A., Schleicher, D. G. Rotation period of comet C/2022 E3 ZTF from CN morphology. The Astronomer's Telegram. 2023a. 15879 1.

Knight, M. M., Schleicher, D. G., Farnham, T. L., Schwieterman, E. W., Christensen, S. R. A Quarter-century of Observations of Comet 10P/Tempel 2 at Lowell Observatory: Continued Spin-down, Coma Morphology, Production Rates, and Numerical Modeling. AJ. 2012. 144 153.

Knight, M. M., Skiff, B. A., Schleicher, D. G., Holt, C. E., Villa, K. M., Mahoney, M., Spiro, L. G. Coma Morphology of Comet C/2022 E3 (ZTF). Asteroids, Comets, Meteors 2023. 2023b.

Knight, M. M., Kokotanekova, R., Samarasinha, N. H. Physical and Surface Properties of Comet Nuclei from Remote Observations. Comets III. 2023c. in press.

Kokotanekova, R., Lister, T., Bannister, M., Snodgrass, C., Opitom, C., Schwamb, M., Kelley, M. S. P. Newly discovered object 2014 UN271 observed as active at 20.18 au. The Astronomer's Telegram. 2021. 14733 1.

Kolokolova, L., Hanner, M. S., Levasseur-Regourd, A.-C., Gustafson, B. Å. S. Physical Properties of Cometary Dust from Light Scattering and Thermal Emission. Comets II. 2004. 577–604.

Korsun, P. P., Kulyk, I. V., Moiseev, A. V., Afanasiev, V. L. Comet C/2010X1 (Elenin). Unrealized expectations. Astrophysical Bulletin. 2012. 67, 4 414–424.

Kozai, Y. Secular Perturbations of Asteroids with High Inclination and Eccentricity. AJ. 1962. 67 591–598.

Kresák, L. Jacobian integral as a classificational and evolutionary parameter of interplanetary bodies. Bulletin of the Astronomical Institutes of Czechoslovakia. 1972. 23 1.

Królikowska, M. A study of the original orbits of "hyperbolic" comets. A&A. 2001. 376 316–324.

Królikowska, M. Non-gravitational effects change the original 1/a-distribution of near-parabolic comets. A&A. 2020. 633 A80.

Królikowska, M., Dybczyński, P. A. Where do long-period comets come from? 26 comets from the non-gravitational Oort spike. MNRAS. 2010. 404, 4 1886–1902.

Królikowska, M., Dybczyński, P. A. Near-parabolic comets observed in 2006-2010. The individualized approach to 1/a-determination and the new distribution of original and future orbits. MNRAS. 2013. 435, 1 440–459.

Królikowska, M., Dybczyński, P. A. Oort spike comets with large perihelion distances. MNRAS. 2017. 472, 4 4634–4658.

Królikowska, M., Sitarski, G., Pittich, E. M., Szutowicz, S., Ziołkowski, K., Rickman, H., Gabryszewski, R., Rickman, B. New catalogue of one-apparition comets discovered in the years 1901-1950. I. Comets from the Oort spike. A&A. 2014. 571 A63.

Lamy, P., Faury, G., Llebaria, A., Knight, M. M., A'Hearn, M. F., Battams, K. Sunskirting comets discovered with the LASCO coronagraphs over the decade 1996–2008. Icarus. 2013. 226 1350–1398.

Landolt, A. U. UBVRI Photometric Standard Stars in the Magnitude Range 11.5-16.0 Around the Celestial Equator. AJ. 1992. 104 340–371.

Landolt, A. U. UBVRI Photometric Standard Stars Around the Celestial Equator: Updates and Additions. AJ. 2009. 137 4186–4269.

Lantz, C., Brunetto, R., Barucci, M. A., Fornasier, S., Baklouti, D., Bourçois, J., Godard, M. Ion irradiation of carbonaceous chondrites: A new view of space weathering on primitive asteroids. Icarus. 2017. 285 43–57.

Larson, S. M., Edberg, S. J., Levy, D. H. The Modern Role of Visual Observations of Comets. IAU Colloq. 116: Comets in the post-Halley era. Astrophysics and Space Science Library. 1991. 167 209.

Lazzarin, M., Marchi, S., Barucci, M. A., Di Martino, M., Barbieri, C. Visible and near-infrared spectroscopic investigation of near-Earth objects at ESO: first results. Icarus. 2004. 169, 2 373–384.

Lazzarin, M., Marchi, S., Magrin, S., Licandro, J. Spectroscopic investigation of near-Earth objects at Telescopio Nazionale Galileo. MNRAS. 2005. 359, 4 1575–1582.

Leonard, G. J., Aschi, S., Pettarin, E., Groeller, H., Rankin, D., Gray, B., Shelly, F. C., Christensen, E. J., Ries, J. G., Roman, B. P., Bulger, J., Chambers, K., Dukes, T., Lowe, T., Schultz, A., Willman, M., Chastel, S., Huber, M., Ramanjooloo, Y., Wainscoat, R., Weryk, R., Breitenstein, P., Wawerzonnek, M., Fuls, D. C., Farneth, G. A., Gibbs, A. R., Grauer, A. D., Kowalski, R. A., Larson, S. M., Pruyne, T. A., Seaman, R. L., Wierzchos, K. W., Valvasori, A., Guido, E., Romanov, F. D., Buczynski, D., Sarneczky, K., Korlevic, K., Ventre, G., Nohara, H., Denneau, L., Tonry, J., Heinze, A., Weiland, H., Flewelling, H., Fitzsimmons, A., Robinson, J., Erasmus, N. COMET C/2021 A1 (Leonard). Minor Planet Electronic Circulars. 2021. 2021-A99.

Levison, H. F. Comet Taxonomy. Completing the Inventory of the Solar System. 107. 1996. 173–191. (Astronomical Society of the Pacific Conference Series).

Levison, H. F., Morbidelli, A., Dones, L., Jedicke, R., Wiegert, P. A., Bottke, W. F. The Mass Disruption of Oort Cloud Comets. Science. 2002. 296 2212–2215.

Levison, H. F., Morbidelli, A., Tsiganis, K., Nesvorný, D., Gomes, R. Late Orbital Instabilities in the Outer Planets Induced by Interaction with a Self-gravitating Planetesimal Disk. AJ. 2011. 142, 5 152.

Li, J., Jewitt, D. Recurrent Perihelion Activity in (3200) Phaethon. AJ. 2013. 145 9pp.

Li, J., Jewitt, D. Disappearance of Comet C/2010 X1 (Elenin): Gone With a Whimper, Not a Bang. AJ. 2015. 149 133.

Lidov, M. L. The evolution of orbits of artificial satellites of planets under the action of gravitational perturbations of external bodies. Planet. Space Sci. 1962. 9, 10 719–759.

Lin, Z.-Y., Yoshida, F., Lin, Y.-C., Cheng, C.-C., Ip, W.-H., Cheng, Y.-C., Pan, K.-S., Daisuke, K., Chi, H.-C. A study of photometric observations of (3200) phaethon from Lulin Observatory. Planet. Space Sci. 2020. 194 105114.

Lister, T. A., Gomez, E., Chatelain, J., Greenstreet, S., MacFarlane, J., Tedeschi, A., Kosic, I. NEOExchange - an online portal for NEO and Solar System science. Icarus. 2021. 364 114387.

Lister, T., Kelley, M. S. P., Holt, C. E., Hsieh, H. H., Bannister, M. T., Verma, A. A., Dobson, M. M., Knight, M. M., Moulane, Y., Schwamb, M. E., Bodewits, D., Bauer, J., Chatelain, J., Fernández-Valenzuela, E., Gardener, D., Gyuk, G., Hammergren, M., Huynh, K., Jehin, E., Kokotanekova, R., Lilly, E., Hui, M.-T., McKay, A., Opitom, C., Protopapa, S., Ridden-Harper, R., Schambeau, C., Snodgrass, C., Stoddard-Jones, C., Usher, H., Wierzchos, K., Yanamandra-Fisher, P. A., Ye, Q., Gomez, E., Greenstreet, S. The LCO Outbursting Objects Key Project: Overview and Year 1 Status. PSJ. 2022. 3, 7 173.

Loeffler, M. J., Dukes, C. A., Baragiola, R. A. Irradiation of olivine by 4 keV He^+: Simulation of space weathering by the solar wind. Journal of Geophysical Research (Planets). 2009. 114, E3 E03003.

Lunine, J. I., Gautier, D. Coupled physical and chemical evolution of volatiles in the protoplanetary disk: a tale of three elements. Comets II. 2004. 105.

MPEC 2019-Q20. COMET C/2019 L3 (ATLAS). Minor Planet Electronic Circulars.

MPEC 2020-P10. COMET C/2020 O2 (Amaral). Minor Planet Electronic Circulars.

MPEC 2020-S168. COMET C/2020 R7 (ATLAS). Minor Planet Electronic Circulars.

MPEC 2020-U260. COMET C/2020 U4 (PANSTARRS). Minor Planet Electronic Circulars.

MPEC 2021-E64. COMET C/2021 C5 (PANSTARRS). Minor Planet Electronic Circulars.

MPEC 2021-M79. COMET A/2021 G2 (ATLAS). Minor Planet Electronic Circulars.

MPEC 2021-P05. COMET A/2021 O3 (PANSTARRS). Minor Planet Electronic Circulars.

MPEC 2021-U187. COMET C/2021 T4 (Lemmon). Minor Planet Electronic Circulars.

MPEC 2022-A50. COMET C/2021 Y1 (ATLAS). Minor Planet Electronic Circulars.

MPEC 2022-C01. COMET C/2022 A2 (PANSTARRS). Minor Planet Electronic Circulars.

MPEC 2022-E107. COMET C/2022 A3 (ATLAS). Minor Planet Electronic Circulars.

Magnier, E. A., Schlafly, E., Finkbeiner, D., Juric, M., Tonry, J. L., Burgett, W. S., Chambers, K. C., Flewelling, H. A., Kaiser, N., Kudritzki, R. P., Morgan, J. S., Price, P. A., Sweeney, W. E., Stubbs, C. W. The Pan-STARRS 1 Photometric Reference Ladder, Release 12.01. ApJS. 2013. 205, 2 20.

Magnusson, P. Distribution of spin axes and senses of rotation for 20 large asteroids. Icarus. 1986. 68, 1 1–39.

Mainzer, A., Bauer, J., Grav, T., Masiero, J., Cutri, R. M., Dailey, J., Eisenhardt, P., McMillan, R. S., Wright, E., Walker, R., Jedicke, R., Spahr, T., Tholen, D., Alles, R., Beck, R., Brandenburg, H., Conrow, T., Evans, T., Fowler, J., Jarrett, T., Marsh, K., Masci, F., McCallon, H., Wheelock, S., Wittman, M., Wyatt, P., DeBaun, E., Elliott, G., Elsbury, D., Gautier, T. IV, Gomillion, S., Leisawitz, D., Maleszewski, C., Micheli, M., Wilkins, A. Preliminary Results from NEOWISE: An Enhancement to the Wide-field Infrared Survey Explorer for Solar System Science. ApJ. 2011. 731 53.

Mainzer, A., Grav, T., Masiero, J., Bauer, J., McMillan, R. S., Giorgini, J., Spahr, T., Cutri, R. M., Tholen, D. J., Jedicke, R., Walker, R., Wright, E., Nugent, C. R. Characterizing Subpopulations within the near-Earth Objects with NEOWISE: Preliminary Results. ApJ. 2012. 752 110.

Mainzer, A. K., Bauer, J. M., Cutri, R. M., Grav, T., Kramer, E. A., Masiero, J. R., Nugent, C. R., Sonnett, S. M., Stevenson, R. A., Wright, E. L. NEOWISE Diameters and Albedos V1.0. NASA Planetary Data System. 2016. EAR–A–COMPIL–5–NEOWISEDIAM–V1.0.

Marchi, S., Delbo', M., Morbidelli, A., Paolicchi, P., Lazzarin, M. Heating of Near-Earth Objects and Meteoroids Due to Close Approaches to the Sun. MNRAS. 2009. 400 147–153.

Marchi, S., Magrin, S., Nesvorný, D., Paolicchi, P., Lazzarin, M. A spectral slope versus perihelion distance correlation for planet-crossing asteroids. MNRAS. 2006a. 368, 1 L39–L42.

Marchi, S., Paolicchi, P., Lazzarin, M., Magrin, S. A General Spectral Slope-Exposure Relation for S-Type Main Belt and Near-Earth Asteroids. AJ. 2006b. 131, 2 1138–1141.

Marcus, J. N. Forward-Scattering Enhancement of Comet Brightness. I. Background and Model. Int. Comet Quart. 2007a. 39–66.

Marcus, J. N. Forward-Scattering Enhancement of Comet Brightness. II. The Light Curve of C/2006 P1 (McNaught). Int. Comet Quart. 2007b. 119–130.

Marsden, B. G., Sekanina, Z. On the distribution of "original" orbits of comets of large perihelion distance. AJ. 1973. 78 1118.

Marsden, B. G., Sekanina, Z., Everhart, E. New osculating orbits for 110 comets and analysis of original orbits for 200 comets. AJ. 1978. 83 64–71.

Masiero, J. R., Wright, E. L., Mainzer, A. K. Thermophysical Modeling of NEOWISE Observations of DESTINY$^+$ Targets Phaethon and 2005 UD. AJ. 2019. 158, 3 97.

Massey, P., Dunham, E. W., Bida, T. A., Collins, P., Hall, J. C., Hunter, D. A., Lauman, S., Levine, S., Neugent, K., Nye, R., Oliver, R., Schleicher, D., Zoonematkermani, S. As Big and As Good As It Gets: The Large Monolithic Imager for Lowell Observatory's 4.3-m Discovery Channel Telescope. American Astronomical Society Meeting Abstracts. 221. 2013. #345.02. (American Astronomical Society Meeting Abstracts).

McCully, C., Volgenau, N. H., Harbeck, D.-R., Lister, T. A., Saunders, E. S., Turner, M. L., Siiverd, R. J., Bowman, M. Real-time processing of the imaging data from the network of Las Cumbres Observatory Telescopes using BANZAI. Software and Cyberinfrastructure for Astronomy V. 10707. 2018. 107070K. (Society of Photo-Optical Instrumentation Engineers (SPIE) Conference Series).

Meech, K. J., Pittichová, J., Bar-Nun, A., Notesco, G., Laufer, D., Hainaut, O. R., Lowry, S. C., Yeomans, D. K., Pitts, M. Activity of comets at large heliocentric distances pre-perihelion. Icarus. 2009. 201, 2 719–739.

Meech, K. J., Svoren, J. Using cometary activity to trace the physical and chemical evolution of cometary nuclei. Comets II. 2004. 317–335.

Meech, K. J., Kleyna, J. T., Hainaut, O., Micheli, M., Bauer, J., Denneau, L., Keane, J. V., Stephens, H., Jedicke, R., Wainscoat, R., Weryk, R., Flewelling, H., Schunová-Lilly, E., Magnier, E., Chambers, K. C. CO-driven Activity in Comet C/2017 K2 (PANSTARRS). ApJL. 2017a. 849, 1 L8.

Meech, K. J., Schambeau, C. A., Sorli, K., Kleyna, J. T., Micheli, M., Bauer, J., Denneau, L., Keane, J. V., Toller, E., Wainscoat, R., Hainaut, O., Bhatt, B., Sahu, D., Yang, B., Kramer, E., Magnier, G. Beginning of Activity in Long-period Comet C/2015 ER61 (PANSTARRS). AJ. 2017b. 153, 5 206.

Meisel, D. D., Morris, C. S. Comet brightness parameters: definition, determination, and correlations. NASA Special Publication. 393. 1976. 410–444.

Milam, S. N., Roth, N. X., Villanueva, G. L., Wong, I., Kelley, M. S. P., al., et. The Abundance and Distribution of Dust and Volatiles in the Coma of Comet C/2022 E3 (ZTF) from the James Webb Space Telescope. Asteroids, Comets, Meteors 2023. 2023.

Molaro, J. L., Walsh, K. J., Jawin, E. R., Ballouz, R. L., Bennett, C. A., DellaGiustina, D. N., Golish, D. R., Drouet d'Aubigny, C., Rizk, B., Schwartz, S. R., Hanna, R. D., Martel, S. J., Pajola, M., Campins, H., Ryan, A. J., Bottke, W. F., Lauretta, D. S. In situ evidence of thermally induced rock breakdown widespread on Bennu's surface. Nature Communications. 2020. 11 2913.

Mommert, M. PHOTOMETRYPIPELINE: An automated pipeline for calibrated photometry. Astronomy and Computing. 2017. 18 47–53.

Mommert, M., Harris, A. W., Mueller, M., Hora, J. L., Trilling, D. E., Bottke, W. F., Thomas, C. A., Delbo, M., Emery, J. P., Fazio, G., Smith, H. A. ExploreNEOs. VIII. Dormant Short-period Comets in the Near-Earth Asteroid Population. AJ. 2015. 150, 4 106.

Mommert, M., Kelley, M., de Val-Borro, M., Li, J.-Y., Guzman, G., Sipőcz, B., Ďurech, J., Granvik, M., Grundy, W., Moskovitz, N., Penttilä, A., Samarasinha, N. sbpy: A Python module for small-body planetary astronomy. The Journal of Open Source Software. 2019. 4, 38 1426.

Morbidelli, A., Delbo, M., Granvik, M., Bottke, W. F., Jedicke, R., Bolin, B., Michel, P., Vokrouhlicky, D. Debiased albedo distribution for Near Earth Objects. Icarus. 2020. 340 113631.

Mousis, O., Hueso, R., Beaulieu, J. P., Bouley, S., Carry, B., Colas, F., Klotz, A., Pellier, C., Petit, J. M., Rousselot, P., Ali-Dib, M., Beisker, W., Birlan, M., Buil, C., Delsanti, A., Frappa, E., Hammel, H. B., Levasseur-Regourd, A. C., Orton, G. S., Sánchez-Lavega, A., Santerne, A., Tanga, P., Vaubaillon, J., Zanda, B., Baratoux, D., Böhm, T., Boudon, V., Bouquet, A., Buzzi, L., Dauvergne, J. L., Decock, A., Delcroix, M., Drossart, P., Esseiva, N., Fischer, G., Fletcher, L. N., Foglia, S., Gómez-Forrellad, J. M., Guarro-Fló, J., Herald, D., Jehin, E., Kugel, F., Lebreton, J. P., Lecacheux, J., Leroy, A., Maquet, L., Masi, G., Maury, A., Meyer, F., Pérez-Hoyos, S., Rajpurohit,

A. S., Rinner, C., Rogers, J. H., Roques, F., Schmude, R. W., Sicardy, B., Tregon, B., Vanhuysse, M., Wesley, A., Widemann, T. Instrumental methods for professional and amateur collaborations in planetary astronomy. Experimental Astronomy. 2014. 38, 1-2 91–191.

Muinonen, K., Belskaya, I. N., Cellino, A., Delbò, M., Levasseur-Regourd, A.-C., Penttilä, A., Tedesco, E. F. A three-parameter magnitude phase function for asteroids. Icarus. 2010. 209 542–555.

Nesvorný, D., Bottke, W. F., Vokrouhlický, D., Chapman, C. R., Rafkin, S. Do planetary encounters reset surfaces of near Earth asteroids? Icarus. 2010. 209, 2 510–519.

Nesvorný, D., Jedicke, R., Whiteley, R. J., Ivezić, Ž. Evidence for asteroid space weathering from the Sloan Digital Sky Survey. Icarus. 2005. 173, 1 132–152.

Noguchi, T., Nakamura, T., Kimura, M., Zolensky, M. E., Tanaka, M., Hashimoto, T., Konno, M., Nakato, A., Ogami, T., Fujimura, A., Abe, M., Yada, T., Mukai, T., Ueno, M., Okada, T., Shirai, K., Ishibashi, Y., Okazaki, R. Incipient Space Weathering Observed on the Surface of Itokawa Dust Particles. Science. 2011. 333, 6046 1121.

Öberg, K. I., Bergin, E. A. Astrochemistry and compositions of planetary systems. Phys. Rep. 2021. 893 1–48.

Oort, J. H. The Structure of the Cloud of Comets Surrounding the Solar System and a Hypothesis Concerning Its Origin. Bulletin of the Astronomical Institutes of the Netherlands. 1950. 11 91–110.

Oort, J. H., Schmidt, M. Differences Between New and Old Comets. Bulletin of the Astronomical Institutes of the Netherlands. 1951. 11 259–269.

Ozaki, N., Yamamoto, T., Gonzalez-Franquesa, F., Gutierrez-Ramon, R., Pushparaj, N., Chikazawa, T., Dei Tos, D. A., Çelik, O., Marmo, N., Kawakatsu, Y., Arai, T., Nishiyama, K., Takashima, T. Mission Design of DESTINY+: Toward Active Asteroid (3200) Phaethon and Multiple Small Bodies. arXiv e-prints. 2022. arXiv:2201.01933.

Paolicchi, P., Marchi, S., Nesvorný, D., Magrin, S., Lazzarin, M. Towards a general model of space weathering of S-complex asteroids and ordinary chondrites. A&A. 2007. 464, 3 1139–1146.

Penttilä, A., Shevchenko, V. G., Wilkman, O., Muinonen, K. H, G_1, G_2 photometric phase function extended to low-accuracy data. Planet. Space Sci. 2016. 123 117–125.

Perna, D., Barucci, M. A., Fulchignoni, M., Popescu, M., Belskaya, I., Fornasier, S., Doressoundiram, A., Lantz, C., Merlin, F. A spectroscopic survey of the small near-Earth asteroid population: Peculiar taxonomic distribution and phase reddening. Planet. Space Sci. 2018. 157 82–95.

Pieters, C. M., Taylor, L. A., Noble, S. K., Keller, L. P., Hapke, B., Morris, R. V., Allen, C. C., McKay, D. S., Wentworth, S. Space weathering on airless bodies: Resolving a mystery with lunar samples. Meteoritics and Planetary Science. 2000. 35, 5 1101–1107.

Popescu, M., Vaduvescu, O., de León, J., Gherase, R. M., Licandro, J., Boacă, I. L., Şonka, A. B., Ashley, R. P., Močnik, T., Morate, D., Predatu, M., De Prá, M., Fariña, C., Stoev, H., Díaz Alfaro, M., Ordonez-Etxeberria, I., López-Martínez, F., Errmann, R. Near-Earth asteroids spectroscopic survey at Isaac Newton Telescope. A&A. 2019. 627 A124.

Pravec, P., Wolf, M., Sarounova, L. 2018. `http://www.asu.cas.cz/~ppravec/newres.htm`.

Rubincam, D. P. Radiative Spin-up and Spin-down of Small Asteroids. Icarus. 2000. 148, 1 2–11.

Samarasinha, N. H., Larson, S. M. Image enhancement techniques for quantitative investigations of morphological features in cometary comae: A comparative study. Icarus. 2014. 239 168–185.

Samarasinha, N. H., Mueller, B. E. A., Knight, M. M., Farnham, T. L., Briol, J., Brosch, N., Caruso, J., Gao, X., Gomez, E., Lister, T., Hergenrother, C., Hoban, S., Prouty, R., Holloway, M., Howes, N., Guido, E., Hui, M.-T., Jones, J. H., Penland, T. B., Thomas, S. R., Wyrosdick, J., Kiselev, N., Ivanova, A. V., Kaye, T. G., Eluo, J.-B. K., Lau, B. P. S., Lin, Z.-Y., Martin, J. L., Moskvitin, A. S., Nicolini, M., Ottum, B. D., Pruzenski, C., Vogel, D. C., Kellett, L., Rapson, V., Schmid, J., Doyle, B., Dimino, F., Carlino, S., Safonova, M., Murthy, J., Sutaria, F., Schleicher, D. G., Snodgrass, C., Tezcan, C. T., Yorukoglu, O., Trowbridge, D., Whitmer, D., Ye, Q.-Z. Results from the worldwide coma morphology campaign for comet ISON (C/2012 S1). Planet. Space Sci. 2015. 118 127–137.

Sanchez, J. A., Reddy, V., Nathues, A., Cloutis, E. A., Mann, P., Hiesinger, H. Phase reddening on near-Earth asteroids: Implications for mineralogical analysis, space weathering and taxonomic classification. Icarus. 2012. 220, 1 36–50.

Sárneczky, K., Szabó, G. M., Csák, B., Kelemen, J., Marschalkó, G., Pál, A., Szakáts, R., Szalai, T., Szegedi-Elek, E., Székely, P., Vida, K., Vinkó, J., Kiss, L. L. Activity of 50 Long-period Comets Beyond 5.2 au. AJ. 2016. 152, 6 220.

Sasaki, S., Nakamura, K., Hamabe, Y., Kurahashi, E., Hiroi, T. Production of iron nanoparticles by laser irradiation in a simulation of lunar-like space weathering. Nature. 2001. 410, 6828 555–557.

Schleicher, D. G., Bair, A. N. The Composition of the Interior of Comet 73P/Schwassmann-Wachmann 3: Results from Narrowband Photometry of Multiple Components. AJ. 2011. 141 177.

Schleicher, D. G., Farnham, T. L. Photometry and Imaging of the Coma with Narrowband Filters. Comets II. 2004. 449–469.

Schleicher, D. G., Millis, R. L., Birch, P. V. Narrowband Photometry of Comet P/Halley: Variation with Heliocentric Distance, Season, and Solar Phase Angle. Icarus. 1998. 132 397–417.

Schwamb, M. E., Jones, R. L., Chesley, S. R., Fitzsimmons, A., Fraser, W. C., Holman, M. J., Hsieh, H., Ragozzine, D., Thomas, C. A., Trilling, D. E., Brown, M. E., Bannister, M. T., Bodewits, D., de Val-Borro, M., Gerdes, D., Granvik, M., Kelley, M. S. P., Knight, M. M., Seaman, R. L., Ye, Q.-Z., Young, L. A. Large Synoptic Survey Telescope Solar System Science Roadmap. ArXiv e-prints. 2018. arXiv:1802.01783.

Scott, D. W. Multivariate density estimation : theory, practice, and visualization / David W. Scott. New York, 1992. (Wiley series in probability and mathematical statistics).

Seaman, R., Abell, P., Christensen, E., Kelley, M. S. P., Schwamb, M. E., Malhotra, R., Juric, M., Ye, Q., Mommert, M., Knight, M. M., Snodgrass, C., Rivkin, A. S. A near-Sun Solar System Twilight Survey with LSST. 2018.

Sekanina, Z. 1I/'Oumuamua and the Problem of Survival of Oort Cloud Comets Near the Sun. arXiv e-prints. 2019. arXiv:1903.06300.

Sekanina, Z., Kracht, R. Disintegration of Comet C/2012 S1 (ISON) Shortly Before Perihelion: Evidence from Independent Data Sets. arXiv e-prints. 2014. arXiv:1404.5968.

Sekanina, Z., Kracht, R. Preperihelion Outbursts and Disintegration of Comet C/2017 S3 (Pan-STARRS). arXiv e-prints. 2018. arXiv:1812.07054.

Shanklin, J. D. The BAA Observers' Workshops: Visual observation of comets. Journal of the British Astronomical Association. 2004. 114 158–160.

Smoluchowski, R. Amorphous ice and the behavior of cometary nuclei. ApJL. 1981. 244 L31–L34.

Snodgrass, C., A'Hearn, M. F., Aceituno, F., Afanasiev, V., Bagnulo, S., Bauer, J., Bergond, G., Besse, S., Biver, N., Bodewits, D., Boehnhardt, H., Bonev, B. P., Borisov, G., Carry, B., Casanova, V., Cochran, A., Conn, B. C., Davidsson, B., Davies, J. K., de León, J., de Mooij, E., de Val-Borro, M., Delacruz, M., DiSanti, M. A., Drew, J. E., Duffard, R., Edberg, N. J. T., Faggi, S., Feaga, L., Fitzsimmons, A., Fujiwara, H., Gibb, E. L., Gillon, M., Green, S. F., Guijarro, A., Guilbert-Lepoutre, A., Gutiérrez, P. J., Hadamcik, E., Hainaut, O., Haque, S., Hedrosa, R., Hines, D., Hopp, U., Hoyo, F., Hutsemékers, D., Hyland, M., Ivanova, O., Jehin, E., Jones, G. H., Keane, J. V., Kelley, M. S. P., Kiselev, N., Kleyna, J., Kluge, M., Knight, M. M., Kokotanekova, R., Koschny, D., Kramer, E. A., López-Moreno, J. J., Lacerda, P., Lara, L. M., Lasue, J., Lehto, H. J., Levasseur-Regourd, A. C., Licandro, J., Lin, Z. Y., Lister, T., Lowry, S. C., Mainzer, A., Manfroid, J., Marchant, J., McKay, A. J., McNeill, A., Meech, K. J., Micheli, M., Mohammed, I., Monguió, M., Moreno, F., Muñoz, O., Mumma,

M. J., Nikolov, P., Opitom, C., Ortiz, J. L., Paganini, L., Pajuelo, M., Pozuelos, F. J., Protopapa, S., Pursimo, T., Rajkumar, B., Ramanjooloo, Y., Ramos, E., Ries, C., Riffeser, A., Rosenbush, V., Rousselot, P., Ryan, E. L., Santos-Sanz, P., Schleicher, D. G., Schmidt, M., Schulz, R., Sen, A. K., Somero, A., Sota, A., Stinson, A., Sunshine, J. M., Thompson, A., Tozzi, G. P., Tubiana, C., Villanueva, G. L., Wang, X., Wooden, D. H., Yagi, M., Yang, B., Zaprudin, B., Zegmott, T. J. The 67P/Churyumov-Gerasimenko observation campaign in support of the Rosetta mission. Philosophical Transactions of the Royal Society of London Series A. 2017. 375 20160249.

Snodgrass, C., Jones, G. H. The European Space Agency's Comet Interceptor lies in wait. Nature Communications. 2019. 10 5418.

Solontoi, M. Comets in Large Sky Surveys: From SDSS to LSST. Doctoral Dissertation, University of Washington. 2010.

Sonnett, S., Mainzer, A., Grav, T., Spahr, T., Masiero, J., Lilly, E. NEOCam/NEO Surveyor Survey Cadence: Discovery, Self-Follow-Up, and Orbital Quality. Lunar and Planetary Science Conference. 2020. 2992. (Lunar and Planetary Science Conference).

Statler, T. S., Cotto-Figueroa, D., Riethmiller, D. A., Sweeney, K. M. Size matters: The rotation rates of small near-Earth asteroids. Icarus. 2013. 225, 1 141–155.

Strazzulla, G., Dotto, E., Binzel, R., Brunetto, R., Barucci, M. A., Blanco, A., Orofino, V. Spectral alteration of the Meteorite Epinal (H5) induced by heavy ion irradiation: a simulation of space weathering effects on near-Earth asteroids. Icarus. 2005. 174, 1 31–35.

Taylor, L. A., Pieters, C. M., Keller, L. P., Morris, R. V., McKay, D. S. Lunar mare soils: Space weathering and the major effects of surface-correlated nanophase Fe. J. Geophys. Res. 2001. 106, E11 27985–28000.

Thomas, C. A., Emery, J. P., Trilling, D. E., Delbó, M., Hora, J. L., Mueller, M. Physical characterization of Warm Spitzer-observed near-Earth objects. Icarus. 2014. 228 217–246.

Thomas, C. A., Trilling, D. E., Rivkin, A. S. Space weathering of small Koronis family asteroids in the SDSS Moving Object Catalog. Icarus. 2012. 219, 1 505–507.

Thomas, C. A., Trilling, D. E., Rivkin, A. S., Linder, T. Space Weathering within C-complex Main Belt Asteroid Families. AJ. 2021. 161, 3 99.

Thomas, P. C., A'Hearn, M. F., Veverka, J., Belton, M. J. S., Kissel, J., Klaasen, K. P., McFadden, L. A., Melosh, H. J., Schultz, P. H., Besse, S., Carcich, B. T., Farnham, T. L., Groussin, O., Hermalyn, B., Li, J.-Y., Lindler, D. J., Lisse, C. M., Meech, K., Richardson, J. E. Shape, density, and geology of the nucleus of Comet 103P/Hartley 2. Icarus. 2013. 222 550–558.

Tisserand, F. Traité de mécanique céleste, Vol 4. Paris Gauthier-Villars. 1896.

Toliou, A., Granvik, M., Tsirvoulis, G. Minimum perihelion distances and associated dwell times for near-Earth asteroids. MNRAS. 2021. 506, 3 3301–3312.

Tonry, J. L., Denneau, L., Flewelling, H., Heinze, A. N., Onken, C. A., Smartt, S. J., Stalder, B., Weiland, H. J., Wolf, C. The ATLAS All-Sky Stellar Reference Catalog. ApJ. 2018. 867, 2 105.

Tonry, J. L., Stubbs, C. W., Lykke, K. R., Doherty, P., Shivvers, I. S., Burgett, W. S., Chambers, K. C., Hodapp, K. W., Kaiser, N., Kudritzki, R.-P., Magnier, E. A., Morgan, J. S., Price, P. A., Wainscoat, R. J. The Pan-STARRS1 Photometric System. ApJ. 2012. 750 99.

Trilling, D. E., Mueller, M., Hora, J. L., Harris, A. W., Bhattacharya, B., Bottke, W. F., Chesley, S., Delbo, M., Emery, J. P., Fazio, G., Mainzer, A., Penprase, B., Smith, H. A., Spahr, T. B., Stansberry, J. A., Thomas, C. A. ExploreNEOs. I. Description and First Results from the Warm Spitzer Near-Earth Object Survey. AJ. 2010. 140 770–784.

Trilling, D., Mommert, M., Hora, J., Chesley, S., Emery, J., Fazio, G., Harris, A., Mueller, M., Smith, H. NEOLegacy: The ultimate Spitzer survey of Near Earth Objects. 2016a. 13006.

Trilling, D. E., Mommert, M., Hora, J., Chesley, S., Emery, J., Fazio, G., Harris, A., Mueller, M., Smith, H. NEOSurvey 1: Initial Results from the Warm Spitzer Exploration Science Survey of Near-Earth Object Properties. AJ. 2016b. 152, 6 172.

Tsiganis, K., Gomes, R., Morbidelli, A., Levison, H. F. Origin of the orbital architecture of the giant planets of the Solar System. Nature. 2005. 435, 7041 459–461.

Urakawa, S., Ohtsuka, K., Abe, S., Ito, T., Nakamura, T. Fast Rotation of a Subkilometer-sized Near-Earth Object 2011 XA_3. AJ. 2014. 147, 5 121.

Usher, H., Snodgrass, C., Biver, N., Kargl, G., Tautvaišienė, G., James, N., Walter, F., Černý, J. Strengthening Pro-Am Comet Community Cooperation: Report on Europlanet Pro-Am Workshop (10-12 June 2022). European Planetary Science Congress. 2022. EPSC2022–1135.

Usui, F., Kasuga, T., Hasegawa, S., Ishiguro, M., Kuroda, D., Müller, T. G., Ootsubo, T., Matsuhara, H. Albedo Properties of Main Belt Asteroids Based on the All-Sky Survey of the Infrared Astronomical Satellite AKARI. ApJ. 2013. 762, 1 56.

Vereš, P., Jedicke, R., Fitzsimmons, A., Denneau, L., Granvik, M., Bolin, B., Chastel, S., Wainscoat, R. J., Burgett, W. S., Chambers, K. C., Flewelling, H., Kaiser, N., Magnier, E. A., Morgan, J. S., Price, P. A., Tonry, J. L., Waters, C. Absolute magnitudes and slope parameters for 250,000 asteroids observed by Pan-STARRS PS1 - Preliminary results. Icarus. 2015. 261 34–47.

Vernazza, P., Binzel, R. P., Rossi, A., Fulchignoni, M., Birlan, M. Solar wind as the origin of rapid reddening of asteroid surfaces. Nature. 2009. 458, 7241 993–995.

Vincent, J.-B., Oklay, N., Pajola, M., Höfner, S., Sierks, H., Hu, X., Barbieri, C., Lamy, P. L., Rodrigo, R., Koschny, D., Rickman, H., Keller, H. U., A'Hearn, M. F., Barucci, M. A., Bertaux, J.-L., Bertini, I., Besse, S., Bodewits, D., Cremonese, G., Da Deppo, V., Davidsson, B., Debei, S., De Cecco, M., El-Maarry, M. R., Fornasier, S., Fulle, M., Groussin, O., Gutiérrez, P. J., Gutiérrez-Marquez, P., Güttler, C., Hofmann, M., Hviid, S. F., Ip, W.-H., Jorda, L., Knollenberg, J., Kovacs, G., Kramm, J.-R., Kührt, E., Küppers, M., Lara, L. M., Lazzarin, M., Lin, Z.-Y., Lopez Moreno, J. J., Lowry, S., Marzari, F., Massironi, M., Moreno, F., Mottola, S., Naletto, G., Preusker, F., Scholten, F., Shi, X., Thomas, N., Toth, I., Tubiana, C. Are fractured cliffs the source of cometary dust jets? Insights from OSIRIS/Rosetta at 67P/Churyumov-Gerasimenko. A&A. 2016. 587 A14.

Vokrouhlický, D., Bottke, W. F., Chesley, S. R., Scheeres, D. J., Statler, T. S. The Yarkovsky and YORP Effects. Asteroids IV. 2015. 509–531.

Vokrouhlický, D., Nesvorný, D. Sun-grazing Orbit of the Unusual Near-Earth Object 2004 LG. A&A. 2012. 541 A109.

Walsh, K. J., Morbidelli, A., Raymond, S. N., O'Brien, D. P., Mandell, A. M. A low mass for Mars from Jupiter's early gas-driven migration. Nature. 2011. 475, 7355 206–209.

Warner, B. D. Near-Earth Asteroid Lightcurve Analysis at CS3-Palmer Divide Station: 2014 January-March. Minor Planet Bulletin. 2014. 41, 3 157–168.

Warner, B. D. Near-Earth Asteroid Lightcurve Analysis at CS3-Palmer Divide Station: 2014 October-December. Minor Planet Bulletin. 2015a. 42, 2 115–127.

Warner, B. D. Near-Earth Asteroid Lightcurve Analysis at CS3-Palmer Divide Station: 2015 January - March. Minor Planet Bulletin. 2015b. 42, 3 172–183.

Warner, B. D. Near-Earth Asteroid Lightcurve Analysis at CS3-Palmer Divide Station: 2016 December thru 2017 April. Minor Planet Bulletin. 2017. 44, 3 223–237.

Waskom, M. L. seaborn: statistical data visualization. Journal of Open Source Software. 2021. 6, 60 3021.

Whipple, F. L. Cometary Brightness Variation and Nucleus Structure. Moon and Planets. 1978. 18 343–359.

Whipple, F. L. 1983 TB and the Geminid Meteors. IAU Circ. 1983. 3881 1.

Wiegert, P., Brown, P., Pokorný, P., Ye, Q., Gregg, C., Lenartowicz, K., Krzeminski, Z., Clark, D. Supercatastrophic Disruption of Asteroids in the Context of SOHO Comet, Fireball, and Meteor Observations. AJ. 2020. 159, 4 143.

Wiegert, P., Tremaine, S. The Evolution of Long-Period Comets. Icarus. 1999. 137, 1 84–121.

Womack, M., Curtis, O., Rabson, D. A., Harrington Pinto, O., Wierzchos, K., Cruz Gonzalez, S., Sarid, G., Mentzer, C., Lastra, N., Pichette, N., Ruffini, N., Cox, T., Rivera, I., Micciche, A., Jackson, C., Homich, A., Tollison, A., Reed, S., Zilka, J., Henning, B., Spinar, M., Escoto, S. R., Erdahl, T., Goldschen-Ohm, M. P., Uhl, W. T. The Visual Lightcurve of Comet C/1995 O1 (Hale-Bopp) from 1995 to 1999. PSJ. 2021. 2, 1 17.

Ye, Q., Granvik, M. Debris of Asteroid Disruptions Close to the Sun. ApJ. 2019. 873, 2 104.

Zakrajsek, J., Mikuz, H. Introducing the Comet Observation database (COBS). Journal of the British Astronomical Association. 2018. 128 279–283.

Zhang, Q., Ye, Q., Farnham, T. L., Holt, C. E. Disintegration of Near-Sun Comet C/2021 O3 (PANSTARRS). The Astronomer's Telegram. 2022. 15358 1.

de Almeida, A. A., Boczko, R., Sanzovo, G. C., Trevisan Sanzovo, D. Analysis of total visual and CCD V-broadband observations of Comet C/1995 O1 (Hale-Bopp): 1995-2001. Advances in Space Research. 2009. 44, 3 335–339.